A DISSERTATION FOR THE DEGREE OF DOCTOR OF PHILOSOPHY

A synthesis of nanoparticle from technical lignin for drug delivery system

산업공정 리그닌을 이용한 약물 방출 조절형 나노입자 합성

Advisor Professor: In-Gyu Choi

By Jae Hoon Lee

PROGRAM IN ENVIRONMENTAL MATERIALS SCIENCE
DEPARTMENT OF FOREST SCIENCES
GRADUATE SCHOOL
SEOUL NATIONAL UNIVERSITY

FEBRUARY, 2021

A synthesis of nanoparticle from technical lignin for drug delivery system

산업공정 리그닌을 이용한 약물 방출 조절형 나노입자 합성

지도교수 최 인 규

이 논문을 농학박사 학위논문으로 제출함
2020년 11 월

서울대학교 대학원
산림과학부 환경재료과학전공
이 재 훈

이재훈의 농학박사 학위논문을 인준함
2021년 1 월

위 원 장	최 준 원	(인)
부위원장	최 인 규	(인)
위 원	김 태 민	(인)
위 원	곽 효 원	(인)
위 원	구 본 욱	(인)

Abstract

A synthesis of nanoparticle from technical lignin for drug delivery system

Jae Hoon Lee

Program in Environmental Materials Science

Department of Forest Sciences

The Graduate School

Seoul National University

There has been growing interest in lignin as a promising source for drug delivery system preparation in recent years. The lignin-based nanoparticle has the potential to be preferably used because of its controllable intracellular uptake and stimuli-controlled drug-releasing ability. However, few research investigated the effect of structural characteristics of lignin on the synthesis of nanoparticles and its essential features such as size, colloidal stability, and biocompatibility. This research focuses on how the molecular structures of technical lignin (kraft and alkaline/soda lignin) affect the lignin nanoparticle properties. Based on these results, drug-encapsulated lignin nanoparticles were synthesized, and those drug-releasing efficiencies were investigated through evaluation of *in vitro* and *in vivo* biocompatibility.

First, lignin fractions with different molecular weights (M_w 1,460 ~ 12,900), phenolic hydroxyl group (total 3.7 ~ 6.2 mmol g^{-1}), and main internal linkages (β-O-4, β-β, and β-5) were obtained by performing a sequential solvent extraction of kraft lignin (KL). Subsequently, spherical lignin nanoparticles (KLNPs, i.d. 193 ~

1,039 nm) were synthesized by the nanoprecipitation process. The low-molecular-weight KL fractions generated KLNPs with a relatively enlarged diameter but less size-distributed. Further analysis showed that molecular weight, total, and phenolic hydroxyl group content in the lignin highly correlated with nanoparticle size. Every KLNPs exhibited comparable and good colloidal stability (-44.5 ~ -29.1 mV). Cell viability and hemotoxicity assessments revealed higher and sustained biocompatibility of KLNPs even at a high concentration, at least for three days.

Second, KL was utilized as a polymer for the drug-encapsulated nanoparticle (ELNP) synthesis. Successful drug encapsulation of ELNPs by nanoprecipitation was determined (max. 59% for coumarin 6 and max. 73% for doxorubicin (DOX)). Compared to KLNP, the size (i.d. 176 ~ 469 nm) and surface charge (-40.5 ~ -32.7 mV) of ELNP showed no remarkable change regardless of introducing the drug in the particle. The drug release profile of ELNPs was faster in the relatively acidic condition (over 70% within 0 ~ 4 h) than the neutral (less than 50% within 0 ~ 4 h). *In vitro* cytotoxicity assay revealed the drug release effect of ELNPs, delaying but not decreasing the anticancer activity. In addition, the hemocompatibility test, *in vivo* allergic reaction test, and tumor inhibition assays using mice tumors showed high ELNP biocompatibility and side effect reduction during the chemotherapy.

Lastly, alkaline/soda lignin (AL) was sequentially solvent-extracted, or its phenolic hydroxyl groups were chemoselectively methylated. These lignins with the modified structure were handled to form nanoparticles (ALNP) to clarify the effect of the lignin structure on the physical properties of nanoparticles. Pure ALNPs were obtained from neat lignin, solvent-extracted fractions (ALNP-Fs, i.d. 414 ~ 1,214 nm), and methylated lignins (ALNP-Ms, i.d. 516 ~ 721 nm). Specifically, the size properties of ALNP-Ms showed a very high negative correlation ($R^2 = 0.95$) with the phenolic hydroxyl group amount. It indicates that the phenolic hydroxyl groups in lignin are the main structures that affect the nucleation and/or condensation during the nanoprecipitation process. ALNPs

exhibited high colloidal stability (-42.3 ~ -32.7 mV), and most of them also showed good *in vitro* biocompatibility.

Keywords: Technical lignin, drug-encapsulated nanoparticle,
              nanoprecipitation, lignin functionalization, drug delivery system,
              biocompatibility

Student number: 2016-30382

Contents

Chapter 2

Synthesis of pure nanoparticles with solvent-fractionated kraft lignin and evaluation of their biocompatibility ························· 51

Chapter 3

In vivo and *in vitro* evaluation of drug-encapsulated lignin

Chapter 4

Effect of chemoselective methylation of the phenolic hydroxyl group on lignin nanoparticle synthesis

List of Tables

vii

List of Figures

Chapter 1

Introduction

1. Background

1.1. The concept of lignocellulosic biorefinery

Lignocellulose is derived from inedible plants, including woody, agricultural, and herbaceous biomass, primarily cellulose, hemicellulose, and lignin (Wertz & Bédué, 2013). Cellulose generally accounts for ca. 40~60%, hemicellulose ca. 20~40%, and lignin ca. 10~25%. It also contains other minor components (e.g., extractives and inorganics). Lignocellulosic biomass is likely to use for an alternative carbon-based resource that can be converted to food, feed, chemicals, materials, and energy by biorefining. In particular, lignocellulosic biomass energy includes cellulosic ethanol, biomass-to-liquid (BtL) diesel, and other BtL fuels (Anwar et al., 2014). There has been growing interest in lignocellulosic biomass energy due to the concerns over the depletion of fossil fuel and increases in energy demand (Demirbas, 2007). Also, lignocellulosic biomass contains little amount of nitrogen and sulfur, which results in the lower emission of pollution sources such as NO_x and SO_x.

The two most common conversion processes of lignocellulosic biomass are biochemical and thermochemical conversion. Among them, biochemical conversion involves breaking down holocellulose to produce sugars that can be converted to bioethanol and other chemicals with enzymes, microbes, and catalysts. In this process, lignin is the principal impediment in the production of bioethanol. Due to the high amount of lignin, substantial amounts of lignin is generated as a byproduct of the biochemical process.

1.2. Lignin production from pulping and sugar-based biorefinery

As shown in Table 1-1 and Figure 1-1, most lignins are produced as waste by the pulp industry (70 million tons per year) but are also expected to be a byproduct from sugar-based biofuels and bioproducts (less than 10 million tons per year) (Fang & Smith Jr, 2016; Ragauskas et al., 2014). Lignin produced as a byproduct in the sugar-based biorefinery process has been used as a heat source for plant work (Ragauskas et al., 2006). However, to make bioethanol or monomeric sugars from lignocellulosic biomass economically viable, a much higher value must be added to the lignin byproduct. In sugar-based biorefinery, a pretreatment process is required to effectively remove lignin from the biomass because lignin polymers exist in the plant cell wall. Organosolv pretreatment, typically using solvents such as methanol, ethanol, acetone, and ethylene glycol, is an efficient pretreatment method because organic solvents are easily recovered and recycled (Johansson et al., 1987). Ionic liquid pretreatment is another promising method due to its eco-friendly characteristics and recyclable capacities, enhancing the accessibility of cellulolytic enzymes to the biomass by reducing both the crystallinity and lignin content (Zhu et al., 2006).

Table 1-1. Global lignin production status and the potential use of them

	Amount (1,000 tons annual^{-1})	Purity	Potential use
Kraft lignin	70,000	Low	Fuel
Lignosulfonate	1,000	Medium	Admixture
Commercial kraft lignin	100		Phenolic resin,
Organosolv lignin	1	High	carbon material,
High-quality lignin	-		and chemical
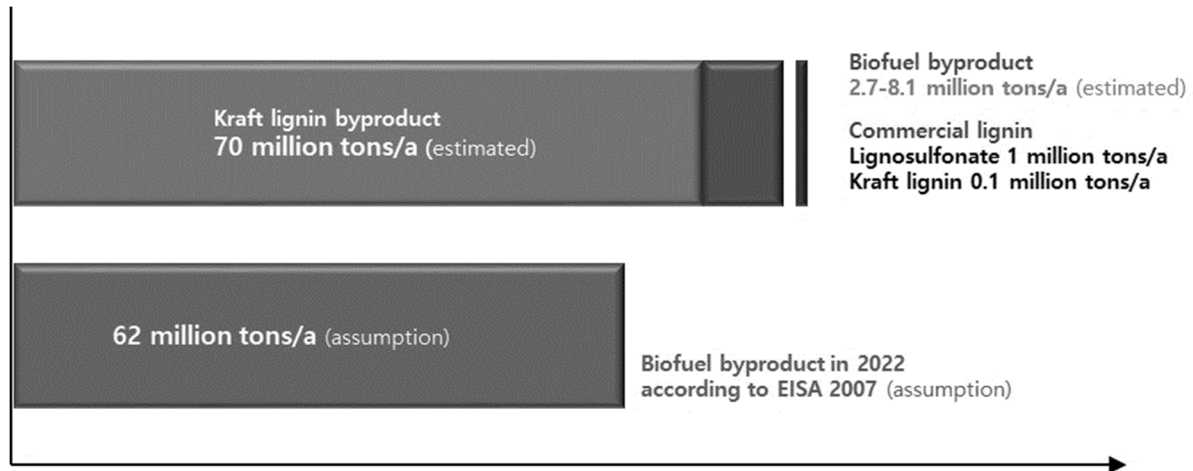
Figure 1-1. The estimated amount of lignin production (Fang & Smith Jr, 2016; Ragauskas et al., 2014)

1.3. Understanding the lignin structure for further application

Lignin is the second most abundant natural polymer, and it accounts for 10~30 wt% of lignocellulosic biomass. Lignin is a natural polymer composed of three different C6C3 types of monolignols (p-coumaryl, coniferyl, and sinapyl alcohol, Figure 1-2) with various interunit linkages β-O-4, β-5, and biphenyl (Gillet et al., 2017). Native lignin has complex and three-dimensional amorphous structures with a high degree of condensation, which allows the lignin to resist physical, chemical, and/or biological forces. Because of this resistance, the utilization of lignin in high value-added products is difficult. For this reason, only 2% of the lignin byproduct produced from the pulp industry is used for the value-added product (Fang & Smith Jr, 2016). A few value-added lignins have traditionally been utilized as a stabilizer for plastics and rubber, phenolic resins, dispersants, automotive brakes, and wood panel products. Production research on aromatic chemicals, carbon fibers, and thermoplastic or fusible materials from various lignins has also been carried out (Kadla et al., 2002; Saito et al., 2013; Zakzeski et al., 2012).

All the lignin uses mentioned so far require proper conversion process conditions, but it is also important to select suitable raw lignin materials because their structural features significantly influence the target products' yield and characteristics. An in-depth study of the structural elements of lignin must be conducted before its widespread utilization.
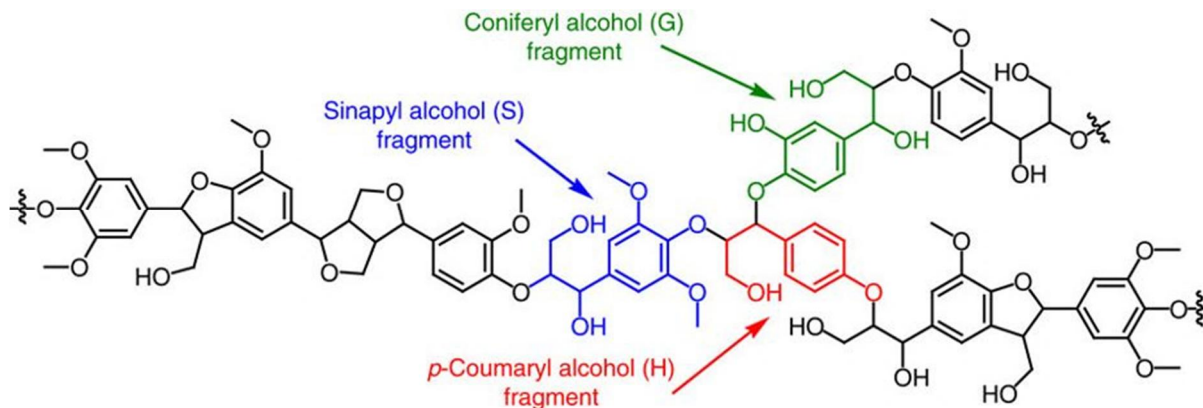
Figure 1-2. Schematic representation of a typical lignin structure (Shao et al., 2017)

1.4. Polymeric nanoparticle for biomedical use

Drug delivery system is generally designed to improve the pharmacological and therapeutic value of a drug molecule in humans or animals (Bianco et al., 2005; Tiwari et al., 2012). Conventional drug delivery systems (tablets, capsules, solutions, etc.) are the most used techniques for medicine administrations (Martinez Rivas et al., 2017). These systems present several advantages to drugs such as full control of preparation processes, common availability of manufacturing facilities, and efficacy. However, they have many problems that may be potentially overcome by methods that can enhance solubility and sustained release of drugs. The global drug delivery systems market was valued at 510 billion US$ in 2016. The global drug delivery systems market is anticipated to expand at a compound annual growth rate (CAGR) of 7% from 2017 to 2025 to reach approximately 900 billion US$.

Nanoparticle-based drug delivery systems show promise as active vectors due to their drug-release ability (Mora-Huertas et al., 2010). Their subcellular size allows higher intracellular uptake than other particulate systems, and they can improve the stability of active drugs or other substances. An encapsulated nanoparticle, so-called nanocapsule, is a vesicular system in which a drug is confined in a space consisting of an inner liquid core encapsulated by a polymeric membrane (Fessi et al., 1989). The global encapsulated nanoparticle market size was valued at 1.9 billion US$ in 2015, relatively very small compared to the whole drug delivery system market, but is expected to witness a CAGR of 8% over the forecast period.

Polymers used for drug encapsulation are preferably produced from both synthetic and natural compounds. Recently, biopolymers, such as polysaccharides, lipids, and proteins, have been studied in detail regarding the ability to be appropriate for release substances. But studies of lignin for biomedical applications, especially for drug release, are rare (Table 1-2). As mentioned earlier, lignin is the
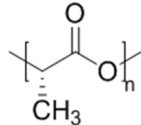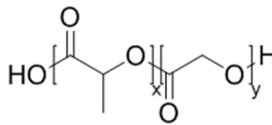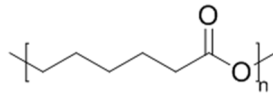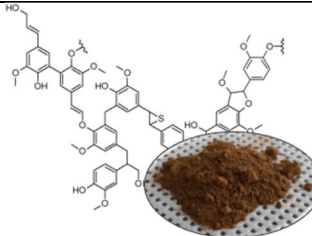
most abundant phenolic biopolymer in nature. It also presents biocompatibility and particularly good stability. All the facts show that lignin is an ideal precursor for developing cheap, environmentally friendly nanomaterials, compared to other nanoparticles (Table 1-3).

Table 1-2. Several scientific publications on the keywords on lignin refined by drug release according to Web of Science

Year	Keywords	
	"Lignin"	"Lignin" and "Drug release"
2016	3,714	11
2017	3,952	11
2018	4,398	19
2019	5,116	30
2020	4,602	22

Table 1-3. Prices and potential market sizes of biocompatible polymers for nanoparticle use

	Polylactic acid	Polylactide-co-glycolic acid	Polycaprolactone	Lignin (kraft)
Price per kg	2.8~3 US$	30 US$	6.8~7 US$	0.2~0.3 US$
Global market size as bioresorbable materials (2019 forecast)[*]	72 million US$	52 million US$	32 million US$	No data

[*] Grand View Research (2016)

1 1

2. Objectives

Over the past few years, there has been growing interest in lignin as a promising source for drug delivery system preparation. Especially, lignin is appropriate for the synthesis of nanoparticle, encapsulation structure of drug delivery. Still, studies of lignin for the application of the nanoparticle are relatively rare. Although some research revealed the controllable intracellular uptake and controlled the drug-release ability of the lignin-based nanoparticle, few research investigated the effect of lignin's molecular structural characteristics on the nanoparticle synthesis. Therefore, there is no reference to manage the nanoparticle formation by controlling lignin molecular structural features (types of lignin isolation, molecular weight, functional group, or internal linkages).

In this study, an in-depth analysis of LignoBoost kraft and alkaline/soda lignin characteristics (molecular weights, functional groups, and internal linkages) and the effect of the features on the pure nanoparticle synthesis was firstly carried out using gel permeation chromatography, gas chromatography, ^{31}P, and 2D-^{1}H-^{13}C HSQC nuclear magnetic resonance. Several fractions with different molecular weights and structures were obtained by sequential solvent extraction. In addition, the lignin phenolic hydroxyl group was chemoselectively blocked to determine the effect of lignin characteristics on the nanoparticle properties. In order to determine these effects, the nanoparticle was synthesized from the modified lignin or fractions by nanoprecipitation and analyzed their essential features by dynamic light scattering and transmission electron microscopy. Spherical lignin nanoparticles with varied particle sizes, size distributions, and relatively stable zeta potential values were obtained from the results. In addition, it was found that the correlations between nanoparticle size and hydroxyl groups of the lignin are presented as high.

Finally, an antitumor-encapsulated lignin nanoparticle with drug encapsulation efficiency and a rapid drug release profile was produced. *In vitro*

cytotoxicity and hemotoxicity tests supported nanoparticles' ability to reduce the antitumor's adverse effects and red blood cell degradation without hypersensitive responses. The antitumor-encapsulated nanoparticle exhibited comparable *in vivo* chemotherapeutic efficacy to the same amount of free drug. However, the side effect was significantly reduced, showing advantages for biomedical applications.

Therefore, this study aims:

(1) To successfully synthesize the lignin-based nanoparticle from technical lignin by nanoprecipitation

(2) To investigate the effect of various technical lignin characteristics on the synthesis of nanoparticle during the nanoprecipitation process

(3) To introduce the potential of drug-encapsulated lignin nanoparticle as a future chemotherapeutic medicine by *in vitro* and *in vivo* assays

(4) To further determine the effect of lignin phenolic hydroxyl group on the drug encapsulation efficiency of lignin nanoparticle
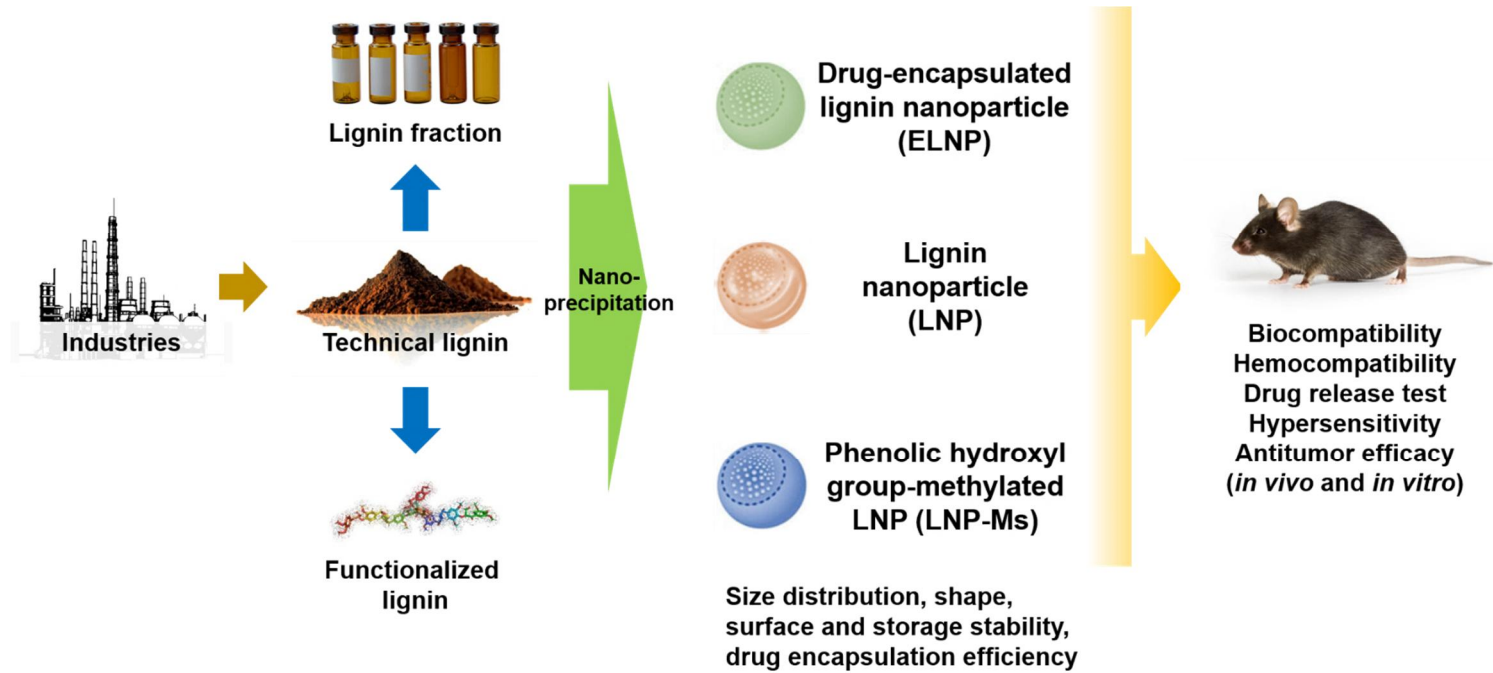
Figure 1-3. The objective of this study

3. Literature review

3.1. Valorization of lignin macromolecules

3.1.1. Isolation of lignin from biomass

Isolation of lignin can be categorized into two groups: lignin for analysis and technical lignin. Firstly, various lignin isolation processes have been developed to understand the structure of native lignin, such as klason and milled wood lignin methods. Klason or 72% H_2SO_4 method is the most widely used method for lignin determination in wood chemistry. Dried raw biomass is digested with 72% H_2SO_4, then hydrolyzed with diluted (4%) H_2SO_4 to solubilize carbohydrates (Sluiter et al., 2008). Partially solubilized lignin fractions can be detected from the UV absorbance of the hydrolysate.

Milled wood lignin (MWL) is a low-yielded fraction from lignocellulosic biomass, extracted by extensive milling followed by solvent extraction (Björkman, 1954). It has high carbohydrate content and is the closest to in vivo native lignin. Therefore, MWL is widely used to understand the structure of native lignin and the lignin-carbohydrate complex (LCC). In the former study, 5.5% of MWL was recovered from poplar wood (*Populus alba × Prosopis glandulosa*) according to the Bjorkman method, and its physicochemical features were identified using gel permeation chromatography, pyrolysis-gas chromatography (GC), and thermogravimetric analyzer (Kim et al., 2015; Kim et al., 2013).

On the other hand, the most famous lignin isolation methods have been developed to remove the lignin during cellulose production and subsequent pulp bleaching. Biorefineries also produce lignin byproducts during the pretreatment of biomass or fractionation steps. Among these byproducts, kraft lignin is the most abundant product since more than 85% of the paper pulp produced worldwide is

generated by kraft pulping. Wood for pulp is treated with a mixture of aqueous NaOH and Na$_2$S at around 180 °C of temperature, and most of the lignin is dissolved in the resulting mixture, so-called black liquor. Precipitation of lignin from black liquor employing acidification in a single stage of dewatering/washing has been the most common process, while a two-stage washing/dewatering process denoted "LignoBoost" was developed recently (Figure 1-4).

The sulfite pulping industry is much smaller than the kraft pulping. Wood is reacted with CaSO$_3$ or MgSO$_3$ at around 150 °C for 7 h. And sulfite ions from the chemicals are introduced into hydrolyzed lignin. Under acidic sulfite pulping conditions, the α-ether linkage in lignin is cleaved, and the hydroxyl groups are substituted with benzyl sulfonic acid (Aro & Fatehi, 2017). These sulfonated lignins (lignosulfonates) are easily isolated from the brown liquor by adding lime suspension or ultrafiltration. Lignosulfonates have a sulfonic acid group that is water-soluble, making it dissolve in water at a wide range of pH values. High water solubility makes lignosulfonates have a wide variety of applications.

The alkaline/soda pulping uses NaOH as a pulping chemical, so there is no sulfur content in soda lignin. Since the soda pulping has been used for not woody products but easy mill, most of the soda lignin derived from *Poaceae* plants, mainly rice and wheat straws or sarkanda grass.

Organosolv is one of the promising biomass fractionation techniques in integrated biorefinery rather than paper pulp production. Because the production pulp is good for enzymatic digestion to convert cellulose into glucose, and major biomass components include lignin can be cleanly separated. Hydrophobic organosolv lignin contains little ash relative to other types of technical lignin. In a previous experiment about a fractionation of empty fruit bunch (EFB) (Lee et al., 2020), organosolv lignin was precipitated from the steam-exploded EFB fraction by acidification with a 2 M of hydrochloric acid, maintaining pH about 2.0. Obtained lignin fractions showed the presence of 14 major peaks via their pyrolysis-GC analysis. Phenolic compounds, including toluene, phenol, guaiacol,

syringol, and isoeugenol, were the major identified compounds.

There is a tremendous amount of technical lignin from pulping (kraft, sulfite, etc.) and biorefinery industries. Worldwide annual production of kraft lignin is estimated to be around 70 million tons (Beckham et al., 2018), whereas 2.7~8.1 million metric tons of lignin from biorefinery is expected to be produced (Fang & Smith Jr, 2016). However, most of the kraft lignin is fed in a boiler to generate the pulp industry's energy, and only less than 2% of lignin is used for the value-added product.
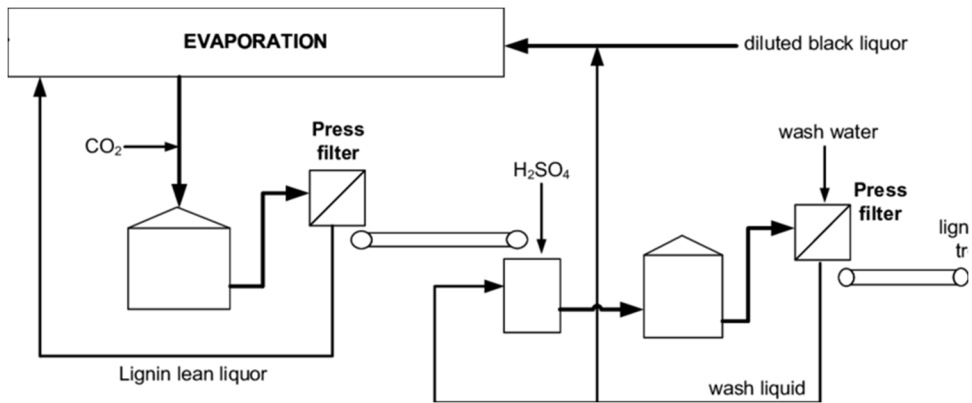
Figure 1-4. Schematic diagram of the LignoBoost process (Hamaguchi et al., 2012)

3.1.2. Determination of lignin structure

The structure of lignin is composed of three primary aromatic alcohols linked by several kinds of inter-unit linkage such as β-aryl ether (45~60%), phenylcoumaran (3~12%), resinol (2~12%), dibenzodioxocin (1~7%), diaryl ether (2%), and spirodienone (1~9%) (Rinaldi et al., 2016). Early studies depolymerized lignin to get structural information by chemical degradation reactions. In a nitrobenzene oxidation (NBO) process, lignin is oxidized by nitrobenzene in an alkaline medium at 180 °C. By cleavage of benzylic and ether bonds in lignin, benzaldehydes (vanillin, syringaldehyde, and *p*-hydroxybenzaldehyde), and benzoic acids (vanillic acid, syringic acid, and *p*-hydroxybenzoic acid) are mainly produced. The yield of these compounds indicates the amount of non-condensed lignin units and their ratio. Nitrobenzene acts as both one-electron-transfer oxidant at the level of the benzylic alcohol group and two-electron-transfer oxidant to produce quinone methides from free phenolic units (Schultz & Templeton, 1986).

Derivatization followed by reductive cleavage (DFRC) is another chemical degradation to obtain degradation monomers from lignin. This method selectively cleaves β-aryl ether and produces acetylated monolignols (coniferyl and sinapyl alcohol) (Lu & Ralph, 1997). It consists of three different stages of reaction: (1) the benzylic bond of lignin is brominated, and free hydroxyl groups are acetylated by acetyl bromide treatment, (2) reductive cleavage of β-aryl ether bonds with Zn, (3) acetylation of free phenolic functional groups for GC analysis.

Nuclear magnetic resonance (NMR) spectrometry also contributed to the determination of complex macromolecular structures of lignin. Proton NMR can be used for quantification of carboxylic acids, formyl, aromatic hydrogens, and methoxyl groups in lignin (Li & Lundquist, 1994). ^{13}C NMR has been widely employed to figure out the carbon skeleton of lignin both qualitatively and quantitatively. Different hydroxyl groups in lignin such as aliphatic, carboxylic, guaiacyl, *p*-hydroxyphenyl, and C5-substituted can be quantified with ^{31}P NMR
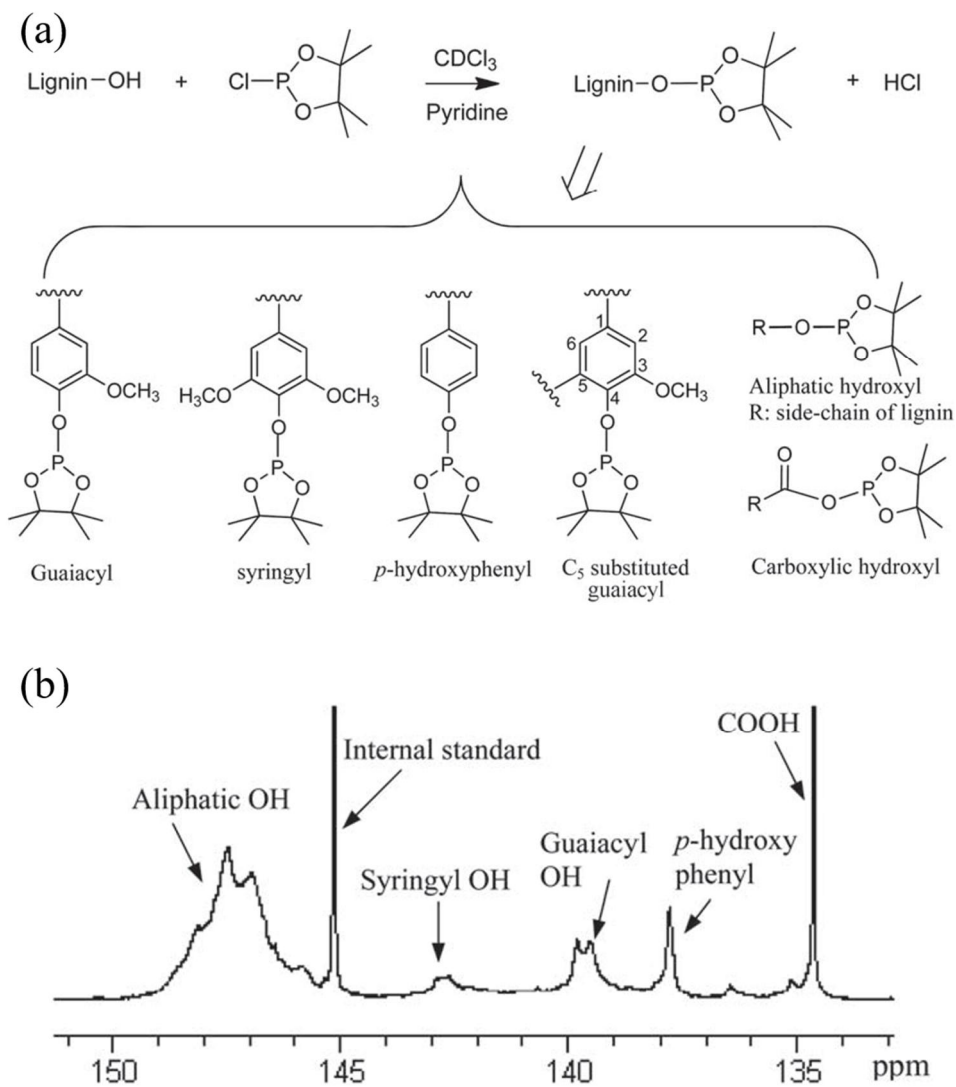
Figure 1-5. (a) Phosphitylation of hydroxyl groups in lignin with 2-chloro-4,4,5,5–tetramethyl-1,3,2-dioxaphospholane and (b) ^{31}P NMR spectrum of a switchgrass ball-milled lignin (Pu et al., 2011)

(Pu et al., 2011). Phosphitylation of hydroxyl groups with proper reagent is needed to operate the NMR analysis, and 2-chloro-4,4,5,5–tetramethyl-1,3,2-dioxaphospholane (TMDP) is the most common reagent for a lignin-derived compound. TMDP reacts with hydroxyl groups in the presence of an organic base (pyridine), and the resulted product can be analyzed by an NMR instrument (Figure 1-5). A previous study determined the aliphatic hydroxyl, phenolic hydroxyl, and carboxyl content of soda lignin and its ethanolyzed products by ^{31}P NMR (Kim et al., 2019).

Recent advances in 2D NMR of lignin contributed to revealing much about different typical interunit bonding units than any other technique. There are various methods of 2D NMR, such as heteronuclear multiple quantum coherence (HMQC), heteronuclear correlation (HETCOR), homonuclear Hartmann-Hahn (HOHAHA), total correlation spectroscopy (TOCSY), rotating frame Overhauser experiment (ROESY), heteronuclear single quantum coherence (HSQC), and heteronuclear multiple bond coherence (HMBC) spectroscopy. Especially, 2D-^{1}H-^{13}C correlative qualitative and quantitative HSQC NMR has proven to be powerful for revealing different types of ether linkages and phenylpropane units in the lignin structure due to its adaptability and structural transformations. Figures 1-6 and 7 show typical 2D HSQC NMR spectra of soda lignin (Kim et al., 2017). The study revealed that the soda lignin contains 6.0% of β-aryl ether, 1.4% of β-β linkage, and 0.5% of β-5 linkage.
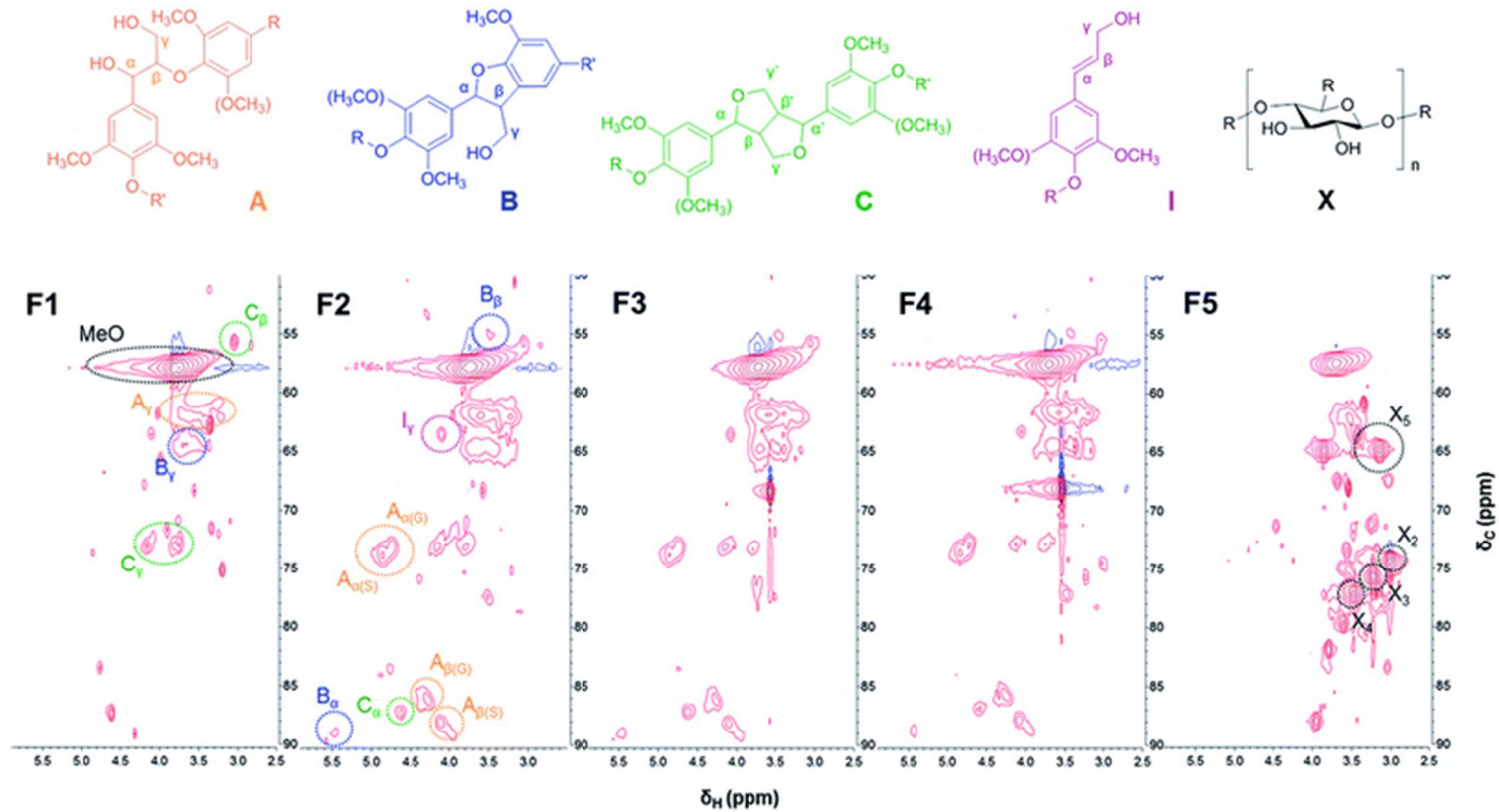
Figure 1-6. Sidechain regions in the 2D-HSQC NMR spectra of lignin fractions (Kim et al., 2017)
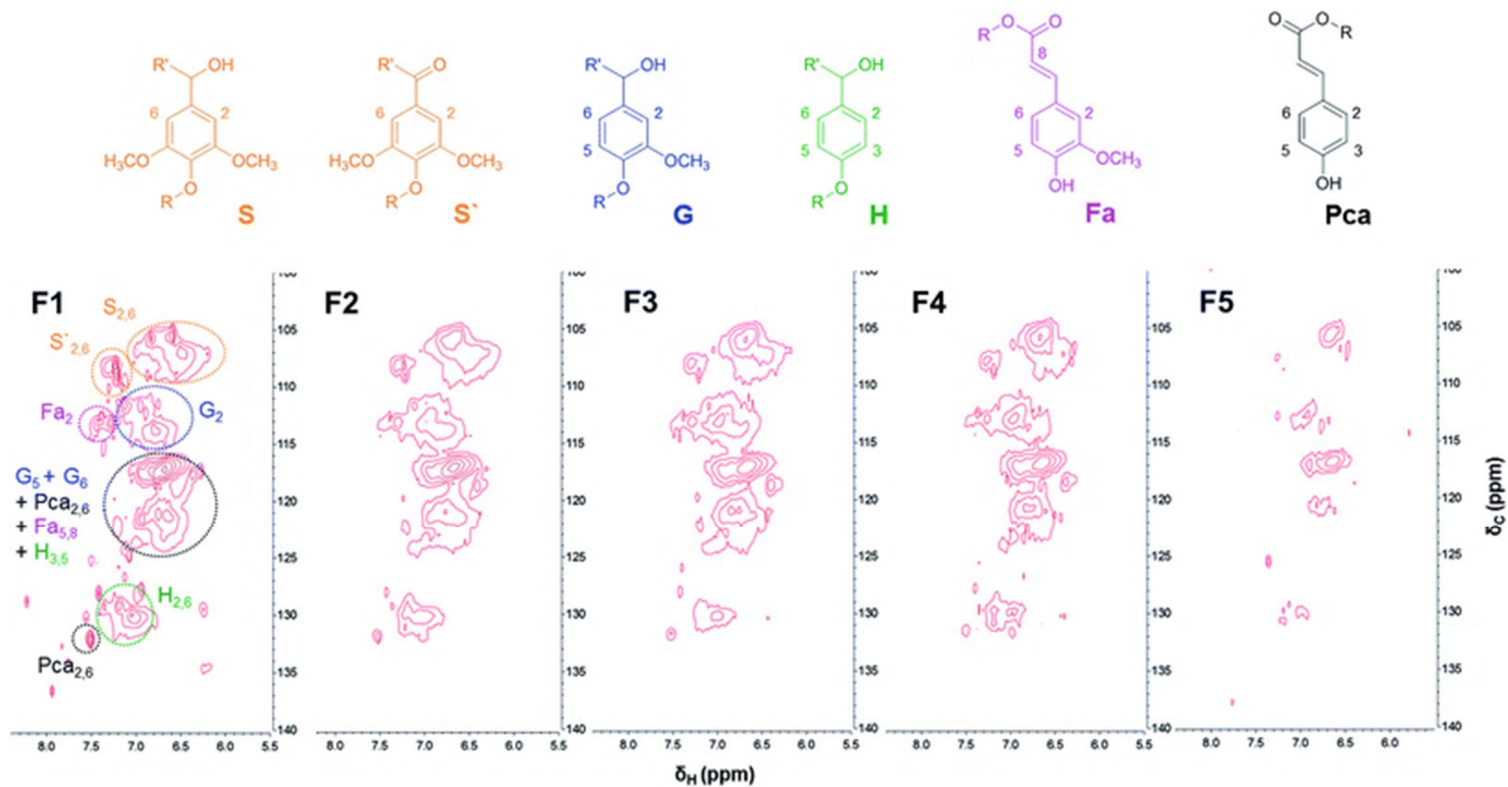
Figure 1-7. Aromatic/unsaturated regions in the 2D-HSQC NMR spectra of lignin fractions (Kim et al., 2017)

3.1.3. Lignin fractionation

3.1.3.1. Solvent extraction

Previous studies revealed that lignin with broad molecular weight distribution could be successfully fractionated into sub-lignin fractions with a narrower distribution. Thus, fractionation aims to obtain specific-molecular-weight lignin fractions with well-defined properties.

Lignin was fractionated by selective extraction at ambient temperature using various concentrations of acetone/water solution (10, 30, 50, 70, and 90%) and ethyl acetate, and the characteristics of each fraction (solubility, molecular weight distribution, and functional groups) were compared (Boeriu et al., 2014). The authors described that the low-molecular-weight lignin fractions are less condensed and have lower aliphatic hydroxyl content than parent lignins, while the high-molecular-weight ones have a higher content of condensed hydroxyl groups.

On the other hand, two-step lignin fractionation using different acetone concentrations (40 and 60%) in water was performed by different research groups (Domínguez-Robles et al., 2018). In this aqueous acetone fractionation, the lower-molecular-weight fractions contained more phenolic hydroxyl groups and carboxylic acid moieties than higher-molecular-weight fractions. In contrast, the higher-molecular-weight fractions possessed much higher amounts of carbohydrates.

The fractionation effect of a different solvent (methanol) on the molecular weight distribution, glass-transition temperature, thermal decomposition, and lignin chemical structure was investigated (Saito et al., 2014). The high-molecular-weight lignin fraction showed a glass-transition temperature of 211 °C and a char yield of 47 %, much higher than those of raw kraft lignin (153 °C and 41 %, respectively). The methanol-soluble fraction of lignin showed an increased low-molecular-weight fraction and a lower glass-transition temperature (117 °C) and

char yield (32 %). The authors revealed that the low-molecular-weight fraction showed a correlation with both inverse proportions of glass-transition temperature and char yield in linear regression.

The impact of sequential solvent fractionation (ethyl acetate, ethanol, methanol, and acetone) of kraft lignin on the chemical structure, antioxidant activity, heating values, and thermal and adsorption properties was investigated (Tagami et al., 2019). The authors reported that the higher-molecular-weight lignin fractions demonstrated better thermal stability and excellent sorption properties toward methylene blue dye. They also found that the ethyl acetate-extracted fraction showed higher antioxidant activity than the natural antioxidants (rutin and quercetin).

Another study also presented sequential solvent extraction of softwood kraft lignin into four different fractions by dissolving it in a methanol–acetone mixture followed by sequential precipitation with various organic solvents (ethyl acetate, ethyl acetate/petroleum ether, petroleum ether) of decreasing solubility parameters (Jiang et al., 2017). The result indicated that the contents of each fraction's internal linkages and thermal properties varied by its molecular weight, and residual polysaccharides only existed in the highest-molecular-weight fraction.

3.1.3.2. Ultrafiltration

Improved membrane technologies allow the separation of lignin by ultrafiltration, membrane filtration in which hydrostatic pressure forces a liquid against a semi-permeable membrane. Lignin fractions with a specific and monodisperse molecular weight distribution can be used in the conversion of value-added products.

A study from Toledano et al. used a black liquor resulting from the alkaline pulping of the *Miscanthus sinensis* to introduce ultrafiltration and obtained several lignin fractions with specific molecular weight distribution (Toledano et al., 2010).

Fractions with different molecular weights and improved polydispersity were obtained by ultrafiltration. However, no significant differences in the composition of the fractions (β-O-4, β-5, guaiacyl, syringyl, ferulates, *p*-coumaric acid, and thermal behavior) were found.

Another study fractionated lignin with narrow molecular weight distributions by ultrafiltration of industrial softwood weak black liquor (Sevastyanova et al., 2014). Membranes with molecular weight cut-offs of 1, 5, and 10 kDa. were used in this process (Figure 1-8). The authors described that the obtained lignin samples had a varying amount of functional groups—the number of functional groups was reversely correlated with their fractions' molecular weight.
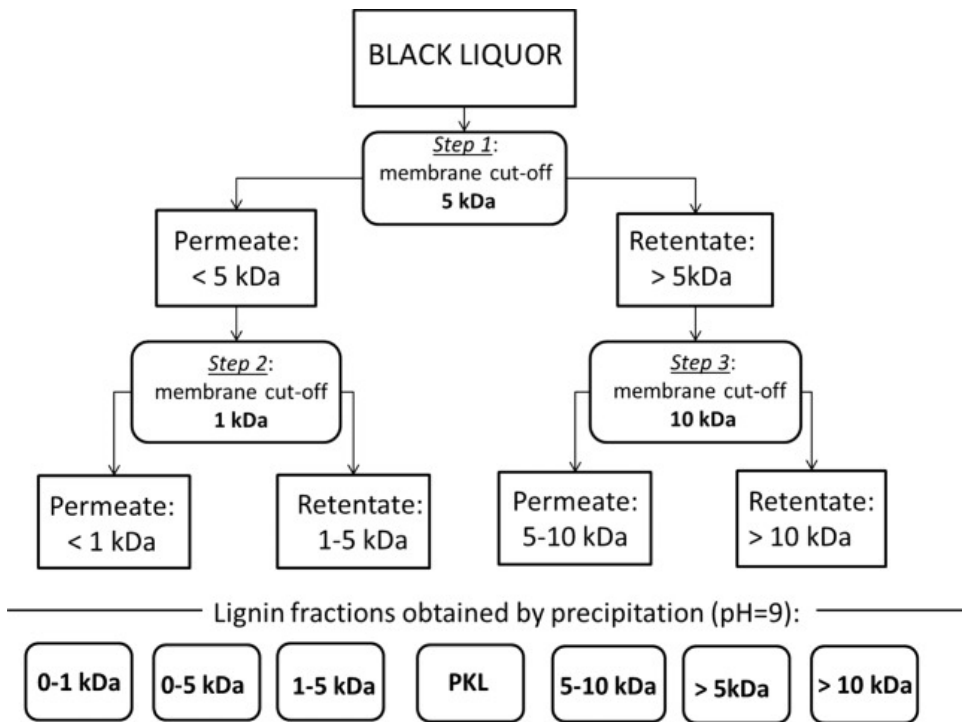
Figure 1-8. Scheme for the fractionation from industrial black liquor by ultrafiltration (Sevastyanova et al., 2014)

3.1.4. Structural functionalization of lignin

Chemical modification of lignin to develop new materials is another promising way of lignin value-addition. Lignin has plenty of reactive functional groups, such as hydroxyl, carbonyl, benzyl alcohol, and carboxyl groups. However, lignin's structural complexity and heterogeneity, attributed to the various functional groups, decrease its processability toward making lignin-derived materials. Therefore, proper structural transformation to introduce new functionalities on lignin has been performed. One way is the incorporation of functional groups that have not existed in raw lignin material. Another is to modify the hydroxyl group, the most frequent and reactive functional group in lignin polymer, for further development.

Lignin functionalization has been performed to increase the chemical reactivity and processability of lignin. Among the modification strategies, the hydroxyl group's alteration is considered the simplest to increase the potential of lignin applications in the polymer industry, including allylation, esterification, etherification, and silylation. Table 1-4 presents several examples of structural modification of lignin.

In the allylation, the hydroxyl groups of lignin are converted into allyl ether groups, which can be further functionalized or directly applied to various chemical reactions, including epoxidation, thiol-end click chemistry, and bromination. Llevot et al. reported an allylation of bio-based phenols (guaiacol, eugenol, vanillyl alcohol, and syringol) and organosolv lignin in the Tsuji–Trost reaction with a Pd nanoparticle catalyst (Llevot et al., 2017). The study revealed that the phenolic hydroxyl groups' selective allylation was employed by 1 mol% of Pd catalyst in an H_2O/dimethylacetamide solvent mixture (44% allylated) and an H_2O/ethyl acetate solvent mixture (83% allylated). Dumont et al. also described the Pd-catalyzed selective allylation of kraft lignin to produce malleable materials (Dumont et al., 2018). Dumont et al. described that the telomerized lignin showed a decreased

Table 1-4. Structural modifications of lignin functional groups

Position	Functionalization	Lignin	References
Hydroxyl group	Allylation	Kraft lignin	Dumont et al. (2018)
			Zhang and Ogale (2014)
			Duval et al. (2015b)
	Esterification	Softwood kraft lignin	Koivu et al. (2016)
			Li et al. (2017)
			Krall et al. (2018)
			Scarica et al. (2018)
		Grass organosolv lignin	Ding et al. (2016)
		Lignin	Larrañeta et al. (2018)
			Duval et al. (2015a)
	Etherification	Softwood lignin	Duval et al. (2015b)
			Gómez-Fernández et al. (2017)
			Zhang et al. (2018)
	Silylation	Kraft lignin	Li et al. (2018)
			de Haro et al. (2019)
	Tosylation	Lignosulfonate	Mahata et al. (2017)

Table 1-4. (continued)

Position	Functionalization	Lignin	References
Hydroxyl group			
Phenolic-specific	Allylation	Bio-based phenols and organosolv lignin	Llevot et al. (2017)
Aliphatic-specific	Esterification	Softwood kraft lignin, organosolv hardwood lignin, and hydroxyethyl lignin	Liu et al. (2019)
	Phenolation	Softwood kraft lignin	Du et al. (2014)
Methoxyl group	Demethylation	Synthetic lignin	Sawamura et al. (2017)
C5 position	Hydroxyalkylation	Corncob lignin, poplar wood lignin, and wheat straw lignin	Yang et al. (2015)
		Corncob lignin	Jiao et al. (2018)
			Du et al. (2014)
	Mannich reaction	Softwood kraft lignin	Mendis et al. (2015)
			Li et al. (2017)
	Nitration	Alkali lignin	Graglia et al. (2016)

glass-transition temperature of 50 °C and can be easily shaped. Furthermore, ^{1}H NMR analysis determined the presence of unsaturated sidechains in the telomerized lignin, which could be further functionalized to synthesize fillers, macromonomers, and compatibilizing agents.

Traditionally, lignin esterification with acid derivatives has been widely used for structural analysis of lignin since it functionalizes the lignin hydroxyl group, decreases intermolecular hydrogen bonding, and increases lignin solubility in nonpolar solvents. Also, lignin esters with larger-chain derivatives showed increased thermal mobility compared to unmodified lignin, which has lead to research for several applications in carbon fibers, thermoset plastics, and coating polymers. Koivu et al. carried out a detailed study of lignin esterification with different acids (C2~C16) to determine the effect of chain length and substitution degree on the lignin's thermal properties ester (Koivu et al., 2016). In this study, softwood kraft lignin was dissolved with a mixture of tetrahydrofuran (THF), dimethylformamide (DMF), and pyridine. Acyl chlorides with four different fatty acid chains (C2, C8, C12, and C16) were introduced in the lignin solution and further reacted. All the synthesized esters showed a decrease in the glass-transition temperature (ΔTg max. -100 °C) and melting temperature with a high loading of fatty acids, suggesting the lignin's potential ester as additives for polymer blends by melt extrusion.

Lignin has been viewed as a promising feedstock of renewable carbon fiber. However, there have been critical issues of decreasing tensile properties (instability or surface defects) for lignin-based carbon fibers. Zhang & Ogale, to overcome the problem, synthesized partially acetylated lignin and used it to prepare dry-spinning carbon fiber (Zhang & Ogale, 2014). The acetylated lignin with low acetic anhydride concentration (0.66 mL g^{-1} lignin) was dissolved in acetone and successfully dry-spun into lignin as-spun fibers (i.d. 30 μm). Final carbonized fibers obtained in this study (i.d. 6~8 μm) displayed higher tensile modulus (52 ± 2 GPa), larger surface area, and higher reactivity due to its less

graphitic surfaces. In the study by García-Mateos et al., carbonyl and hydroxyl groups of Alcell lignin were esterified with phosphoric acid to generate phosphate and/or polyphosphate esters during electrospinning lignin fiber preparation in ethanol (García-Mateos et al., 2018). Product fibers containing phosphorus-functionalities have shown an increased glass-transition temperature and a much shorter stabilization time (105 min) than the pure lignin fibers (more than 90 h) without fiber fusion issues. The fiber also has submicron size (i.d. ≤ 1 µm), higher surface area, and uniformly distributed O and P surface functionalities that can be used as a heterogeneous catalyst, adsorbent, and electrode.

Functionalization with an alkylene oxide applied to lignin is the most well-known etherification process, giving lignin higher solubility in organic solvents and additional active sites. Duval et al. applied epoxide ring-opening etherification with the lignin hydroxyl group to provide the benzene ring site to lignin for further modifications (Duval et al., 2015a). Phenolic hydroxyl groups of kraft lignin were selectively reacted with ring-opened styrene oxide in an alkaline solution (NaOH) at 50 °C. The new benzene rings in this benzylated lignin were further reacted with diazotized *N,N*-dimethyl-*p*-phenylenediamine to contain diazobenzene groups, granting pH- and light-responsive properties to it.

Silylation is also one of the candidate modifications to improve the mechanical properties of lignin as polymer alternatives. Li et al. performed an experiment of lignin modification with 1,1,3,3-tetramethyl-1,3-divinyldisilazane, which increases film flexibility and can partially replace polyacrylonitrile (PAN) in applications. Given its properties as lightweight and stiffness, PAN is the most used precursor for producing the carbon film. Pine kraft lignin was mixed with 1,1,3,3-tetramethyl-1,3-divinyldisilazane using a twin-screw extruder at 120 °C for 15 min (31 % sylilated). This vinyl silylated lignin was then copolymerized with acrylonitrile to form the PAN-grafted vinyl silylated lignin with improved thermal stability.

Moreover, the films based on lignin-*graft* (g)-PAN showed much higher

tensile strength (18 MPa) and strain (55% by a dynamic mechanical analyzer) than that of an unmodified lignin-based copolymer (10 MPa and 10%, respectively) (Figure 1-9). Buono et al. produced silylated lignin, and its thermal, physicochemical, and blending properties were compared to acetylated lignin. Soda lignin (Protobind 1000™) was silylated with *t*-butyldimethylsilylchloride using imidazole as a catalyst and base at room temperature. The authors noted that the whole lignin phenolic hydroxyl group was functionalized quickly; however, around 15% of the aliphatic hydroxyl group could not be reacted, possibly due to the steric hindrance. The silylated lignin was well melt-blended with low-density polyethylene (LDPE) at 10% loading and showed better thermal stability and compatibility with the LDPE matrix than the neat or acetylated lignins.

So far, approaches to modify the hydroxyl group in the lignin has been increasingly studied. Sawamura et al. investigated the effect of the lignin methoxyl group's demethylation to convert it to a hydroxyl group with three different chemicals (1-dodecanethiol, hydroiodic acid, and iodocyclohexane) (Sawamura et al., 2017). Synthetic lignin, guaiacyl-type dehydrogenation polymer (GDHP), was used in this study. Among the chemicals used, iodocyclohexane found to be the most effective for increasing the number of phenolic hydroxyl groups.

Several types of chemical reactions have been used to synthesize new functional groups onto lignin; hydroxyalkylation, nitration, amination, etc. (Table 1-4). Each modification method can contribute to the change of physicochemical properties of lignin.

Hydroxyalkylation is a reaction that can replace the carboxyl group and hydroxyl group of lignin using formaldehyde and strong bases, such as NaOH or Na_2CO_3. This reaction includes the condensation of an aldehyde with activated lignin aromatic regions for further functionalization or improving solubility and mechanical properties of the lignin-derived resin. Several studies were conducted to use hydroxyalkylated lignin-derived resin as a binder replacement in particleboard or plywood. Yang et al. synthesized hydroxymethyl lignin from four
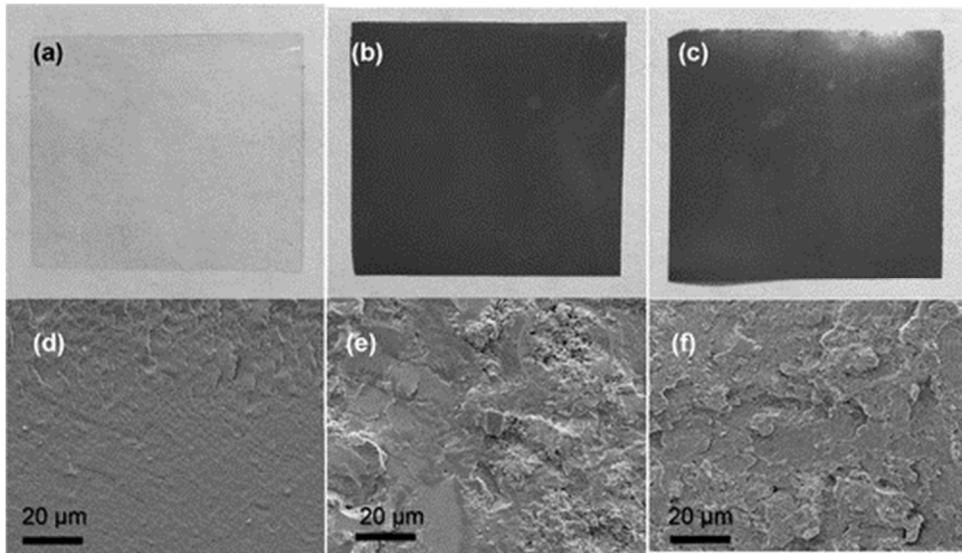
Figure 1-9. Optical images of (a) PAN, (b) lignin-g-PAN, and (c) vinyl silylated lignin-g-PAN films. Cross-section SEM images (1000×) of (d) PAN, (e) lignin-g-PAN, and (f) vinyl silylated lignin-g-PAN films.

kinds of technical lignin (corncob lignin, two different poplar wood lignins, and wheat straw lignin) obtained from black liquor or biorefinery mills (Yang et al., 2015). In this study, an aromatic region of lignin and formaldehyde were reacted in the presence of NaOH (pH 9~10) at 80 °C to form a methylol group on the *para* or *ortho* positions of a phenolic hydroxyl group. These functionalized lignins were then copolymerized with phenol to produce lignin-phenol-formaldehyde resin adhesive in the preparation of plywood. A similar experiment of lignin modification was described (Wang & Chen, 2014). Alkaline lignin solution extracted from corn stalk (pH 10.5~12.0) was methylolated at 60~80 °C. The authors noticed that high temperatures at over 90 °C could accelerate the self-condensation process of methylolated lignin. The methylol groups in the aromatic C_5 position of lignin were subsequently condensed with phenolic resin as plywood adhesives under hot pressing conditions (0.8 MPa at 160 °C). Another study of lignin hydroxyalkylation was conducted (Jiao et al., 2018). In their research, corncob lignin was methylolated at 80 °C and pH 11.5 to enhance lignin's reactivity toward making a hydroxymethylurea polymer. This three-dimensional lignin polymer network captures hydroxymethylurea and slowly releases nitrogenous compounds (NH_4^+ and NO_3^-). As a result, the authors suggested that the hydroxymethylated lignin could be a diffusional barrier of controlled-release nitrogen fertilizer.

Nitration and Mannich reaction are used to add nitrogen-containing functional groups in an aromatic region of lignin structure. Lignin nitration is used not only for further substitution reactions or adding a directing group that enables the incoming electrophile to react at specific positions on the aromatic ring but also to produce nitrated aromatics, which is an important intermediate in chemical industries. Graglia et al. reported nitrogen-doped carbon preparation using functionalized lignin via aromatic nitration followed by carbonization in molten eutectic $KCl/ZnCl_2$. It was reported that nitrogen doping enhances the electroactivity of carbon. Residual lignin obtained from lactic acid production was

reacted with inorganic acid catalysts in acetic anhydride at 0 °C. The obtained acetylated nitrogen-functionalized lignin (NL) with 6.7% nitrogen content was employed to synthesize nitrogen-doped carbon via carbonization in molten eutectic $KCl/ZnCl_2$. Compared to further deacetylated NL and aminated lignin, NL was reported to show slightly better electrocatalytic activity for the oxygen reduction reaction when carbonized (Graglia et al., 2016).

The Mannich reaction is a condensation reaction of ammonia, primary or secondary amine, in the presence of formaldehyde. This reaction introduces amine groups to the unsubstituted *ortho* position in the lignin and is used to synthesize building blocks to prepare nitrogen-containing compounds or nitrogen-doped materials. Du et al. performed the amination of the lignin model compound (apocynin) and LignoBoost softwood kraft lignin by the Mannich reaction (Axegård & STFI-Packforsk, 2007; Du et al., 2014). In this research, the lignin was dissolved in 1,4-dioxane, then 10 equivalents of dimethylamine and formaldehyde were subsequently introduced in the solution. The Mannich reaction between lignin, amine, and formaldehyde was carried out under sealing conditions at 60 °C for 4 h. Du et al. identified a new $ArCH_2N$ signal in ^{13}C NMR and 2D-HSQC NMR from the resulting aminated lignin and determined that 28 amine groups were successfully introduced per 100 aromatic rings. Furthermore, 42 amine groups were introduced per 100 aromatic rings by the Mannich reaction after phenolation. The aminated lignin products were hydrophilic and showed higher zeta potential (max. 31.6 mV) and charge density (max. 1.6×10^{-7} Equiv. mL^{-1}) that could form surfactant chemicals or polycationic materials.

Li et al. applied the Mannich reaction to synthesize the aminated lignin-polylactic acid (PLA) blend (Li et al., 2017). Softwood kraft lignin was reacted with diethylamine and formaldehyde at 60 °C for 4 h under sealing and stirring. ^{31}P NMR spectra showed the complete disappearance of the guaiacyl hydroxyl group peak, and the rise of C_5 substituted (dialkylaminomethyl) guaiacyl hydroxyl group peak indicates the full introduction of dialkylaminomethyl group at the C_5

position of the lignin aromatic ring. They reported that the blend coating of PLA-aminated lignin on the urea pellet fertilizer for food production provides additional bound nitrogen (high molecular amine groups) to the fertilizer to supply a slow-release effect.

3.2. Nano-sized carriers for drug delivery

3.2.1. Strategies for drug delivery

Drug delivery system (DDS) is the process of transporting pharmaceutical compounds in the body to safely achieve a therapeutic effect in humans or animals (Tiwari et al., 2012). It includes conventional drug administration types such as traditional solid tablets, capsules, nasal spray, and injection. Also, there has been increased interest in the use of nanoparticles as a promising drug carrier in recent decades. There are several representatives of the nanoparticle drug delivery system: liposomes, nanospheres, silica or carbon nanostructures, and encapsulated nanoparticles (Figure 1-10).

3.2.1.1. Liposome

A liposome is a bilayer, spherical, and colloidal vesicle composed of phospholipids and steroids in aqueous media (Zylberberg & Matosevic, 2016). Drug-contained liposome was the first nanomedicine in FDA clinical trials since it has been the first to be investigated as a nano-sized drug carrier (Bobo et al., 2016; Zylberberg & Matosevic, 2016). The phospholipid bilayer structure of liposome is similar to the cell membrane, so it can mimic the living cell's biophysical properties and perform some cellular functions such as moving or shape-changing (Hua & Wu, 2013).

Recent studies focused on modifying phospholipid bilayer with appropriate compounds (amphiphiles) to improve the duration and elasticity or developing brand new lipid-drug complexes for enhanced drug delivery. One example is the liposome with a synthetic polymer called hydrazine-functionalized poly(ethylene glycol)-phosphatidylethanolamine-based amphiphilic polymer to conjugate ligands via a reversible, pH-cleavable bond (Biswas et al., 2011). This polymer
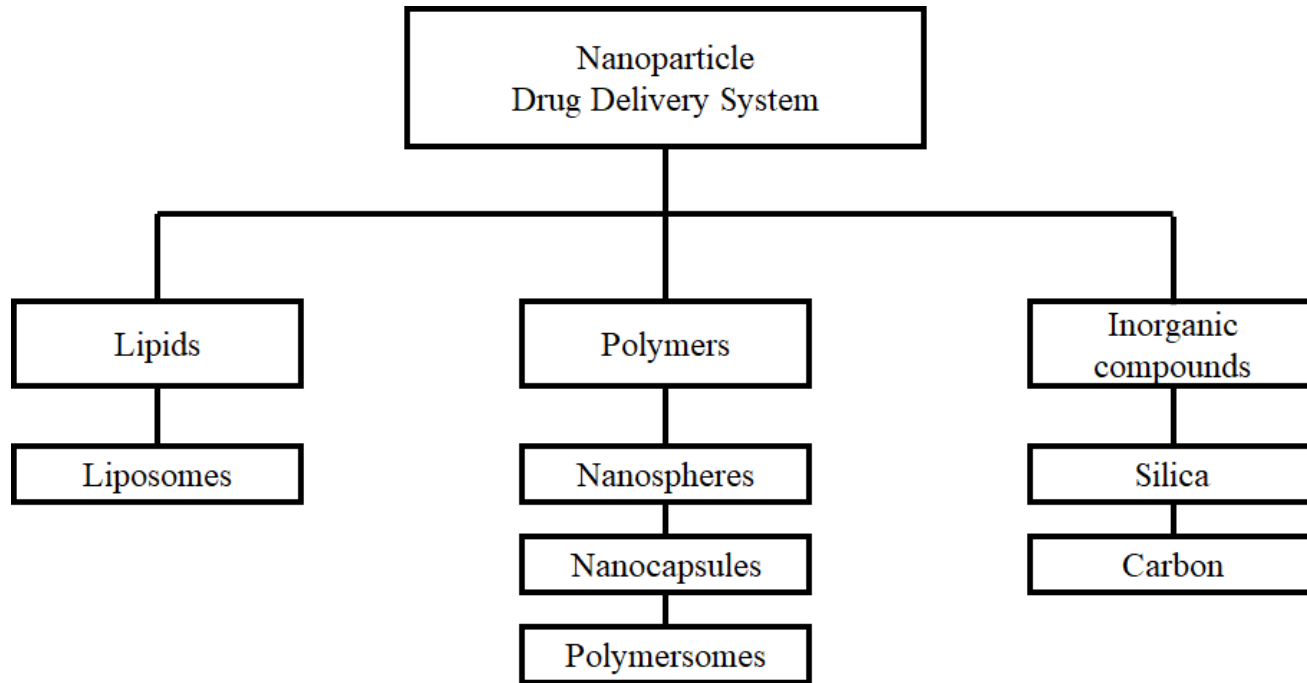
Figure 1-10. Nanoparticle drug delivery system (modified from Letchford and Burt (2007))

successfully conjugated various targeting ligands to liposomes via a pH-responsive reversible hydrazone bond.

3.2.1.2. Silica nanostructure

Mesoporous silica nanoparticles, such as MCM-41 and SBA-15, are used in controlled drug delivery systems (Slowing et al., 2006; Yang et al., 2005). Silica nanoparticle's large surface area and pore volume provide not only encapsulation property but also the possibility of capping/releasing the drug.

3.2.1.3. Carbon nanotube

A carbon nanotube is one of the promising materials used in various biomedical applications, including nanosensor, nanorobot, nanoprobe, and drug nanocarrier (Beg et al., 2011). Carbon nanotubes can be classified into many different structures, depending on their shapes (nanohorn, nanobud, and nanotorus). The larger inner volume and immobilization of their outer surface and biocompatibility make the carbon nanotube a good material for the drug delivery system.

3.2.1.4. Polymeric nanoparticle

Polymeric nanoparticles have advantages as biomaterials since they have favorable characteristics of simple elaboration and design, biocompatibility, and a variety of structures (El-Say & El-Sawy, 2017). As a drug delivery system, the polymeric nanoparticle has controlled release characteristics, a combination of therapy and theranostic, drug molecule protection, and targeting ability (Crucho & Barros, 2017).

Nanosphere is the simplest type of nanoparticle, a polymer matrix structure in

which drugs are entrapped to the matrix (Figure 1-11). The size of the particle is between 100 and 200 nm. Thanks to the small size, nanosphere drug carriers can be introduced by oral, local, and systemic injection (Brittain, 2013).

Encapsulated nanoparticles (Figure 1-11 and Table 1-5) and polymersome are more complicated forms of nanoparticles, consist of a polymer shell and space inside in which drugs may be placed (Fessi et al., 1989). There are two kinds of capsule-type nanoparticles, depending on the core and polymer surrounded. A single layer of polymer surrounding an oily core is referred to as an encapsulated nanoparticle or nanocapsule. For example, hydrophobic drugs like Ru 58668 (antiestrogen for breast cancer), methotrexate diethyl ester (immune system suppressant), and xanthone derivatives are incorporated into encapsulated nanoparticles (Ameller et al., 2003; Teixeira et al., 2005; Yurgel et al., 2014). Various polymer types are used for the encapsulated nanoparticle formation; PLA, polylactic-co-glycolic acid (PLGA), and polycaprolactone (Letchford & Burt, 2007). On the other hand, a polymeric bilayer surrounding an aqueous core is referred to as a polymersome. Its structure is similar to that of the liposome. Water-soluble drugs are incorporated into the bilayer of diblock copolymers like polyethylene glycol (PEG)-b-polybutadiene, and PEG-poly (ethyl ethylene) or PEGylated polyesters (Zhang & Zhang, 2017).
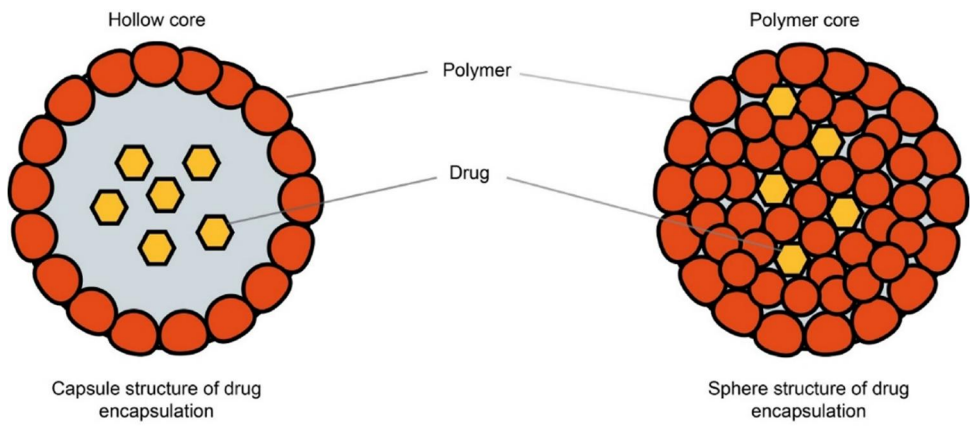
Figure 1-11. Schematics of encapsulation forms of polymeric nanoparticles (Martinez Rivas et al., 2017)

Table 1-5. Types of natural polymer-based nanoparticle for commercial drug delivery

Polymer	Drug	Therapeutic activity	References
Cellulose	Methylene blue (drug model compound)		Butun et al. (2011)
Carboxymethylcellulose	Aciclovir	Herpes simplex virus	Chin et al. (2018)
Ethylcellulose	Retinyl acetate	Photoaging, severe acne, and skin inflammation	Arayachukeat et al. (2011)
Cellulose-g-poly(Methylmethacrylate)	Betulinic acid	Topoisomerase activity	Dai and Si (2017)
Chitosan (CS)	Rifampicin	Tuberculosis	Rawal et al. (2017)
CS-octenylsuccinic anhydride	Curcumin and quercetin	Inflammation	Yu et al. (2020)
RGD-CS-PLGA	Paclitaxel	Lung cancer	Babu et al. (2017)
CS-tripolyphosphate	Aciclovir	Herpes simplex virus	Calderón et al. (2013)
Gelatin			
Amphiphilic gelatin	Camptothecin and doxorubicin	Tumor	Li et al. (2015)

3.2.2. Nanoparticle synthesis

3.2.2.1. Nanoprecipitation

The nanoprecipitation (a.k.a. solvent displacement) is the low energy input process for preparing polymeric nanoparticles (Fessi et al., 1989; Schubert et al., 2011). In general, the interfacial deposition of the polymer is performed after a displacement of the organic phase (solvent phase) from the aqueous phase (non-solvent phase). The organic phase consists of water-miscible solvent, polymer source for nanoparticle formation, drug, and oil. Quick diffusion of the organic phase and dissolved polymer into the aqueous phase encourages the nanoparticle formation to avoid the water molecules. In comparison, dialysis is slightly different from the nanoprecipitation process but has the same solvent displacement mechanism. As an organic phase solvent, acetone is the most used. Acetone-ethanol blend and THF are also commonly selected solvents.

Based on the theory of polymer precipitation, the particle formation in the nanoprecipitation contains three steps: nucleation, growth, and aggregation (Figure 1-12). In fact, prior to nucleation, the addition of an aqueous phase decreases the dissolving potency organic phase to force to undergo a supersaturation step (Martinez Rivas et al., 2017). Then, nucleation is induced by an excess of the energy barrier (ΔG), the boundaries of a critical level that is solvent/non-solvent specific. Therefore, the nucleation rate is higher when the ΔG has low interfacial tension levels at the solid-liquid interface and the molar volume of solute, and higher temperature. Nuclei are grown by adding single molecules to the adjacent particle surface until the non-adsorbed solvent reaches equilibrium saturation.

Biodegradable polyesters, especially polycaprolactone, PLA, and PLGA, are used as sources of gene or drug delivery systems (Boehm et al., 2000; Lassalle & Ferreira, 2007; Panyam & Labhasetwar, 2003), and polysaccharides or lignin are the natural polymer candidates.
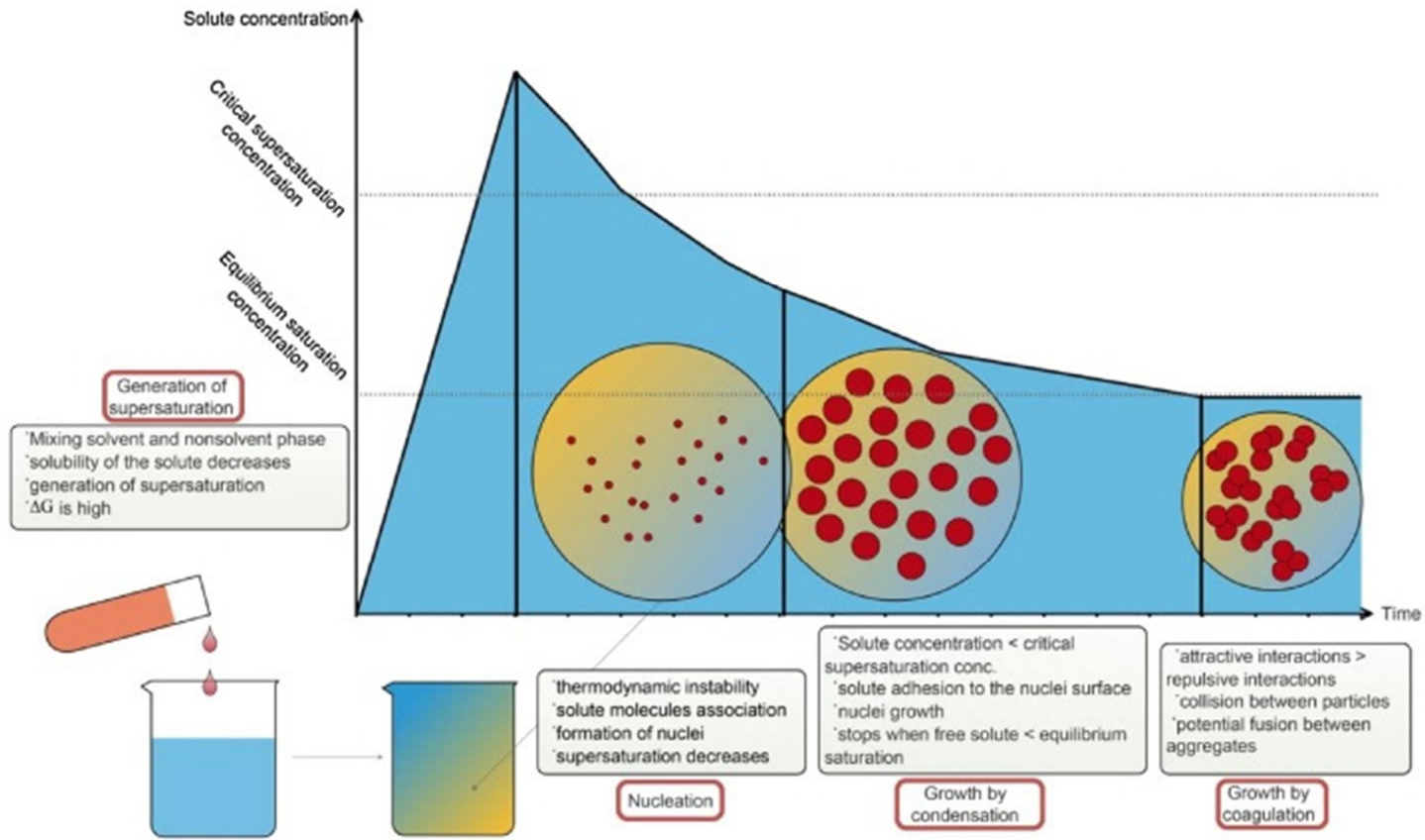
Figure 1-12. Schematic illustration of nanoprecipitation (Martinez Rivas et al., 2017)

3.2.2.2. Emulsion-diffusion

Emulsion-diffusion consists of forming a conventional oil-water (o/w) emulsion between a partially water-miscible organic solvent containing the dissolved polymer and drug and an aqueous solution having a surfactant (Quintanar-Guerrero et al., 1998). This method is the most widely used for the production of polymer nanoparticles from monomers. The general concept is categorized as non-surfactant and surfactant emulsion polymerization based on the surfactant used. The more complicated heterodisperse method, water-oil-water emulsions of emulsions (w/o/w), is so-called double emulsification, which uses two surfactants (Garti, 1997).

3.2.2.3. Polymer coating

The polymer coating process contains modified conventional methods, a thin layer-formed polymer can be deposited on the nanoparticle surface during the final stage of nanoprecipitation and double emulsification. In contrast, a polymer-coating process could be the first step to prepare the nanoemulsion template to coat it with another polymer on the w/o emulsion surface (Prego et al., 2005).

3.2.2.4. Layer-by-layer

The layer-by-layer assembly process for colloidal particle preparation can produce fine vesicular particles, called polyelectrolyte capsules, with well-defined chemical and structural properties (Figure 1-13). The nanocapsule formation mechanism is based on an irreversible electrostatic attraction. This reaction leads to polyelectrolyte adsorption at supersaturating bulk polyelectrolyte concentrations.
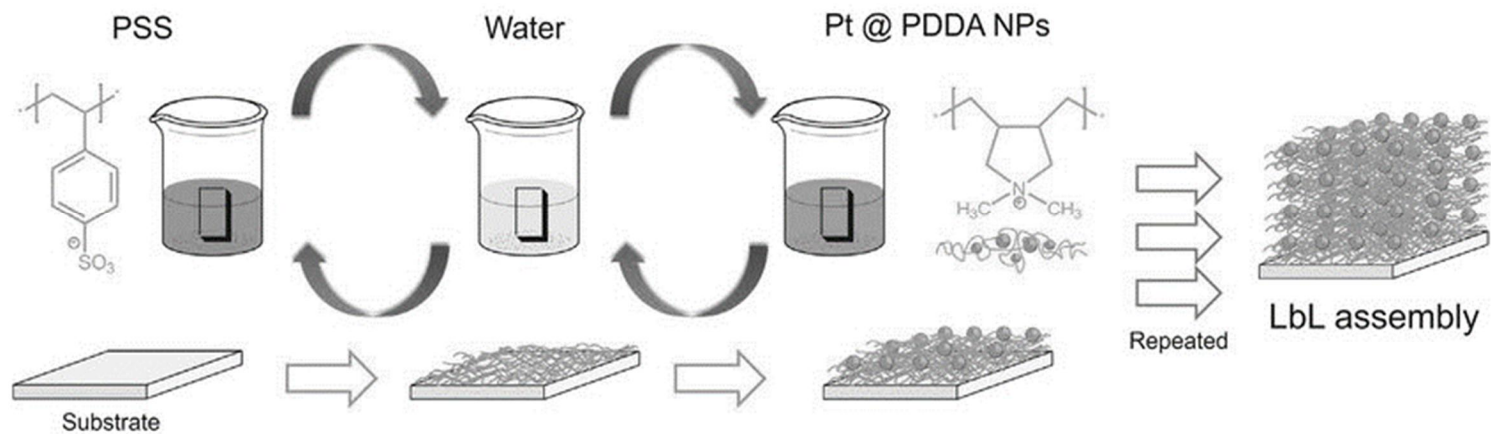
Figure 1-13. Schematic illustration of the layer-by-layer assembly of polyelectrolyte capped-platinum nanoparticles (Fenoy et al., 2017)

3.2.3. Strategies for controlled drug release

Recent progress of polymeric nanoparticle systems for drug delivery has been focused on achieving a delivery profile that yields a high level of the drug in the body over a long period, reduced side effects, and increased bioavailability in the organism (Siepmann et al., 2012). Each drug delivery system has its chemical, physical, and morphological characteristics and may affect different drug polarities through covalent bonds, hydrogen bonds, or other electrostatic interactions.

Several studies regarding drug-release mechanisms in the drug delivery system have been carried out. Diffusion, solvent, chemical reaction by the change of pH, hydrolysis, or enzyme reaction, and stimuli-controlled release are just a few that can represent the mechanisms (Figure 1-14).

Diffusion is a very important component of many controlled drug releases. Not only drugs but also all molecules randomly collide with other molecules and execute thermal or Brownian motion. Many mathematical models have been used to explain several drug delivery systems and predict the overall behavior to provide a particular drug release profile and predict resulting kinetics (Bruschi, 2015; Korsmeyer & Peppas, 1983).

Recently, drug delivery strategies are being formulated to improve the organism's nanostructure target-specificity (Singh & Amiji, 2018). Reduction of the immunogenicity through modifying polymer coat or functionalization is provided by several substances, such as synthetic polymers, natural polysaccharides, bilipid membranes, and tunable surfactants, etc. The specific chemistry of various affected areas helps to engineer stimuli-responsive properties responding to the conditions, allowing for precise drug delivery, improving its effectiveness, and minimizing off-target effects.
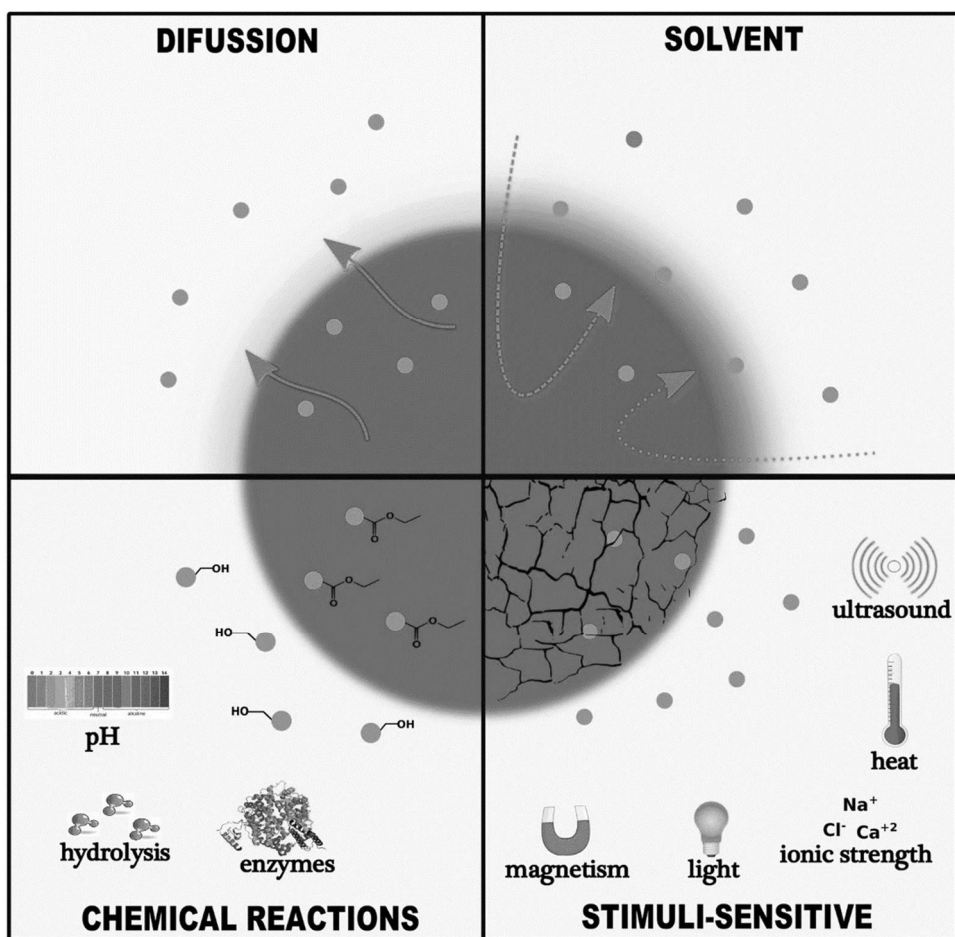
Figure 1-14. Mechanisms for the controlled release of drugs using nanoparticles (Patra et al., 2018)

Chapter 2

A synthesis of pure nanoparticles with solvent-fractionated kraft lignin and evaluation of their biocompatibility

1. Introduction

Lignin is the second most abundant natural polymer, composed of three different C6C3 types of monolignols (p-coumaryl, coniferyl, and sinapyl alcohol) with various interunit linkages such as β-O-4, β-5, and biphenyl (Glasser, 2019). Native lignin has complex and three-dimensional amorphous structures with a high degree of condensation, which allows the lignin to resist physical, chemical, and/or biological forces. Because of this resistance, the utilization of lignin in high value-added products is very difficult (Himmel et al., 2007). There is a tremendous amount of technical lignin produced from the pulping (kraft, sulfite, etc.) and biorefinery (bioethanol) industries (Lora, 2008; Sannigrahi et al., 2010). The worldwide annual production of lignin is estimated to be around 70 million tons but is also expected to be produced as a byproduct of biorefining (less than 10 million tons per year) (Fang & Smith Jr, 2016; Ragauskas et al., 2014). However, only less than 2% of the lignin byproduct is used for high-value products. Therefore, the value-addition of lignin, as a stabilizer for plastics and rubber (Gregorová et al., 2006; Jiang et al., 2013), phenolic resin (Cavdar et al., 2008; Ibrahim et al., 2011; Sarkar & Adhikari, 2000), and automotive brake pads, has been investigated to date (Park et al., 2018a). Yet, all these lignin uses mentioned require proper conversion. It is also important to choose lignin feedstock with suitable structural features that can influence the characteristics of the products. For these reasons, fundamental studies on the conversion and structural features of lignin must be conducted.

One of the promising ways is to provide high-value to lignin as a material for drug delivery. A drug delivery system (DDS) is a process to improve the pharmacological and therapeutic effect of a drug molecule inside the human body through oral, pulmonary, transdermal, and injection systems (Tiwari et al., 2012). In recent decades, polymeric nano-sized DDSs are preferably utilized because of their higher intracellular uptake and exquisite drug-release capability (Couvreur,

2013; Li et al., 2019). In addition, natural polymers such as polysaccharides (Liu et al., 2012; Ye et al., 2005), lipids (Heurtault et al., 2003), or lignin have the great potential to be appropriate as releasing substances by demonstrating lower toxicity and side effects. Lignin is biocompatible (Chen et al., 2018; Figueiredo et al., 2017; Kai et al., 2018) and the second most abundant biopolymer, thus it is a promising material for the preparation of pharmaceutical nanoparticles. Much nanoparticle production for hydrophobic drug delivery has been based on the simple and reproducible interfacial deposition technique called nanoprecipitation (Martinez Rivas et al., 2017). In this method, polymer materials' characteristics are crucial parameters since they affect the size or drug loading capacity of the nanoparticle. However, few reported investigations of the effect of structural characteristics of lignin (e.g., molecular weight, functional groups, and molecular structure) could affect properties of lignin nanoparticles. Recent works fractionated lignin with two different concentrations of ethanol solution to obtain different lignin fractions with different molecular weights and hydrophilic group content values (Ma et al., 2020; Pang et al., 2020). The authors investigated the effects of lignin characteristics on the nanosizing behaviors during nanoprecipitation but the structural differences between each lignin fraction are not significant.

This study was initiated to determine the effect of lignin characteristics, mainly molecular weights, functional groups, and internal linkages, on the synthesis of nanoparticles and their properties (particle size, surface charge, stability, and cytotoxicity). First, kraft lignin as representative technical lignin was fractionated by sequential solvent extraction to obtain five different fractions with significant molecular and structural differences. Then, lignin-based nanoparticles were synthesized by the nanoprecipitation method, and their physicochemical properties were comprehensively analyzed by dynamic light scattering (DLS) and transmission electron microscopy (TEM). The comparative biocompatibility of the lignin nanoparticles was also assessed by cell viability and hemolysis testing.

2. Materials and methods

2.1. Materials

A commercial pine kraft lignin (BioChoice® Lignin, KL) extracted by the LignoBoost process was provided by Domtar Inc., Plymouth, NC, USA. Elemental analysis (CHNSO) of KL was conducted using an elemental analyzer (628 Series, Sulfur add-on module, LECO Co., St. Joseph, MI, USA). The oxygen content was calculated by difference. Proximate analysis was performed according to the National Renewable Energy Laboratory (NREL) standard procedures (Sluiter et al., 2005a; Sluiter et al., 2005b). The total carbohydrate content was determined by difference. All results with the corresponding values are listed in Table 2-1.

Organic solvents for sequential solvent extraction of lignin (ethyl acetate, 2-butanone, methanol, acetone, and dioxane), tetrahydrofuran (THF), and the dialysis tubing (molecular weight cut-off 14,000 Da) were purchased from Sigma-Aldrich Korea (Yongin, Republic of Korea).

Table 2-1. Elemental and chemical composition of pine kraft lignin

Properties	Value
Elemental analysis (wt%)	
Carbon	61.7 ± 0.5
Hydrogen	5.0 ± 0.2
Nitrogen	0.0 ± 0.0
Oxygen[*]	31.5 ± 0.3
Sulfur	1.8 ± 0.2
Proximate analysis (wt%, dry basis)	
Carbohydrates[*]	10.8 ± 1.8
Acid-insoluble lignin	86.1 ± 2.0
Acid-soluble lignin	2.6 ± 0.3
Ash	1.8 ± 0.1

[*] calculated by difference

2.2. Lignin fractionation

Sequential organic solvent fractionation of KL was performed using Park's method (Park et al., 2018b). In detail, 10 g of lignin was dissolved in 200 mL of ethyl acetate and was stirred at room temperature for 2 h. This mixture was filtered using a 2G4 funnel glass filter under a vacuum to separate an undissolved fraction. The dissolved fraction was evaporated to remove most of the solvent, followed by precipitation with DI water, and then finally freeze-dried to recover the lignin fraction denoted KL-F1. This process was sequentially repeated with the undissolved fractions using 2-butanone, methanol, acetone, and a dioxane-water mixture (95:5 v/v) as the solvent. The recovered fractions were denoted KL-F2, KL-F3, KL-F4, and KL-F5, respectively (Figure 2-1). The yield of each kraft lignin fraction (KLF) was determined gravimetrically.
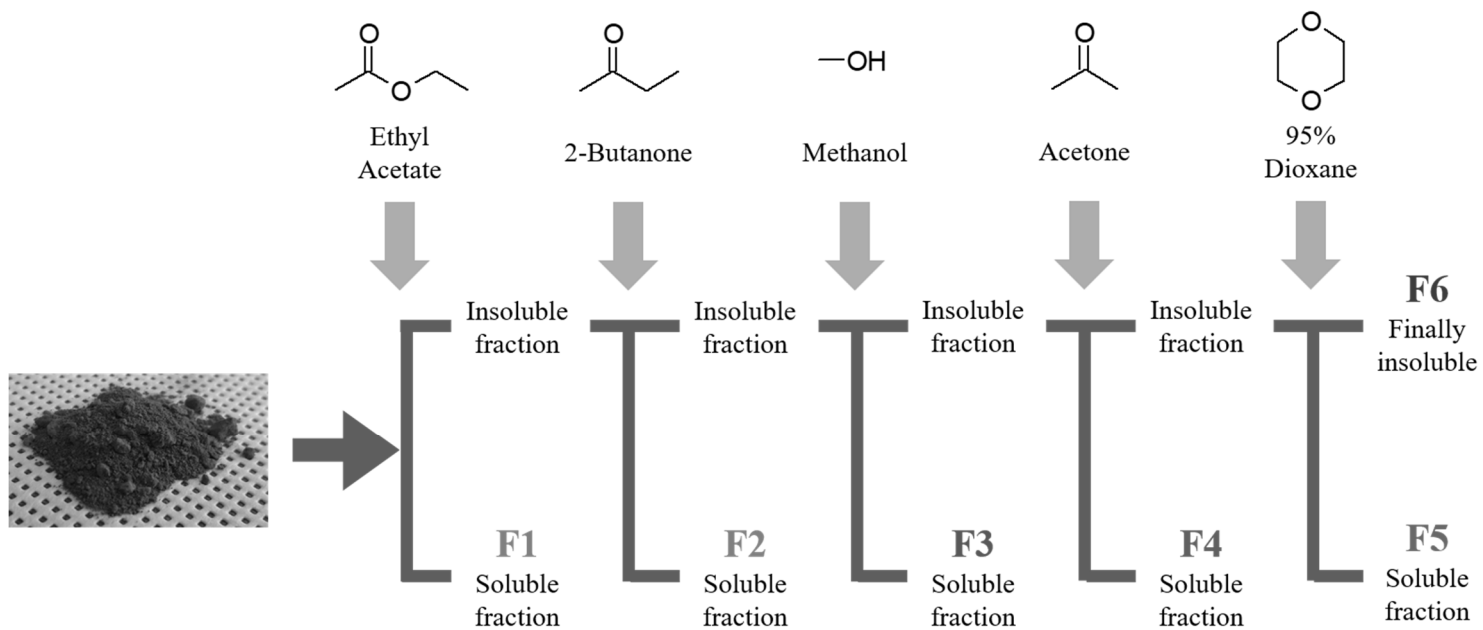
Figure 2-1. Schematic diagram of sequential solvent extraction process of kraft lignin with six different solvents

2.3. Characterization of fractionated lignin

The number and weight average molecular weights of KLFs were determined by gel permeation chromatography (GPC). A 10 mg sample dissolved in 1 mL of THF was introduced into a GPC instrument (1260 Infinity II LC Systems, Agilent Technologies Inc., Santa Clara, CA, USA) equipped with a PLgel 5 μm MIXED-C column (300 × 7.5 mm, Agilent Technologies Inc.) and a refractive index detector (Table 2-2). A polystyrene standard (low molecular, Sigma-Aldrich Korea, Yongin, Republic of Korea) was used to calibrate the molecular weights of the analyte in the effluent (1.0 mL min^{-1}).

Methoxyl group content of lignin was determined by the reaction of KLFs with hydroiodic acid for 30 min at 130 °C to release methyl iodide from the methoxyl groups (Baker, 1996). After cooling the sample, ethyl iodide as an internal standard and pentane were added. The mixture was shaken vigorously, and 1 mL of pentane phase was analyzed using a gas chromatography-mass spectrometry system (5975C Series GC/MSD System, Agilent Technologies Inc.) (Table 2-3). The amount of methyl iodide from KLF was quantified.

Table 2-2. Gel permeation chromatography conditions used in this study

THF-GPC (1260 Infinity II LC Systems)	
Column	PLgel 5 μm MIXED-C (300 × 7.5 mm)
Flow rate	1.0 mL min^{-1}
Oven temperature	40 °C
Detector	RI
Sample injection	20 μL

Table 2-3. Gas chromatography-mass spectrometry system conditions used in this study

GC/MSD (5975C Series GC/MSD System)	
Column	DB-5 (30 m × 250 μm × 0.25 μm)
Split ratio	5:1
Oven program	40 C° for 2 min then 10 C° min^{-1} to 80 C° for 1 min
Carrier gas	He

^{31}P nuclear magnetic resonance (NMR) spectra were obtained to quantify the free hydroxyl group content in KLFs (Pu et al., 2011). Each 20 mg lignin fraction dissolved in 0.55 mL pyridine/CDCl$_3$ mixture (1.6:1, v/v) was phosphorylated with 70 μL of 2-chloro-4,4,5,5-tetramethyl-1,3,2-dioxaphospholane (TMDP). Cyclohexanol was used as an internal standard. The solution was analyzed by a Bruker AVANCE 600 MHz instrument (Bruker, Billerica, MA, USA).

2D-^{1}H-^{13}C heteronuclear single quantum coherence (HSQC) NMR spectrometry was conducted to identify structural differences between lignin fractions (Sette et al., 2013). Each 60 mg lignin fraction dissolved in 1 mL of dimethylsulfoxide-d_6 (DMSO-d_6) was analyzed with the Bruker AVANCE™ 600 MHz applying a pulse sequence "hsqcedetgpsp.3" with a 90° pulse, 0.16 s acquisition time, 1.5 s relaxation delay, 32 scans, and acquisition of 1024 data points (for ^{1}H) over 512 increments (for ^{13}C). The central DMSO solvent peak was used as a reference (δ_C = 40.1; δ_H = 2.5). Relative quantitative analysis based on the 2D-HSQC spectra was carried out using MestReNova® v12.0 software (Mestrelab Research, Santiago de Compostela, Spain) (Wen et al., 2013).

2.4. Synthesis of lignin nanoparticle

2.4.1. Pre-dialysis concentration

Synthesis of KL nanoparticles (KLNP) was conducted by modification from the method of Lievonen (Lievonen et al., 2016). KL was dissolved in THF at four different concentrations (1, 2, 4, and 6 mg mL^{-1}), and the solutions were then filtered with a 0.50 μm syringe filter. Note that the negligible mass of KL was undissolved in THF and filtered. The solution was poured into a pre-soaked dialysis tube. The tube was immersed in excess deionized water (replaced at intervals of 3 h) for over 12 h while stirring at 300 rpm (Figure 2-2). Products were labeled as KLNP-C1, KLNP-C2, KLNP-C4, and KLNP-C6, respectively. Each experimental variable was run in triplicate.

The recovery of the synthesized particles was calculated using Eq. (1):

$$Recovery \ of \ KLNPs \ (\%) = W_{KLNP}/W_t \times 100 \qquad (1)$$

where W_t is the weight of total lignin and W_{KLNP} is the weight of KLNPs obtained by lyophilization (over 48 h) of a whole lignin suspension.
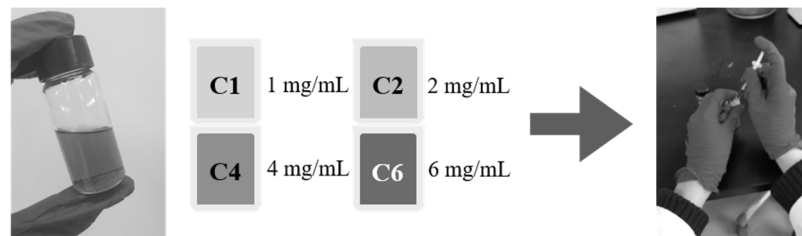
Filtration
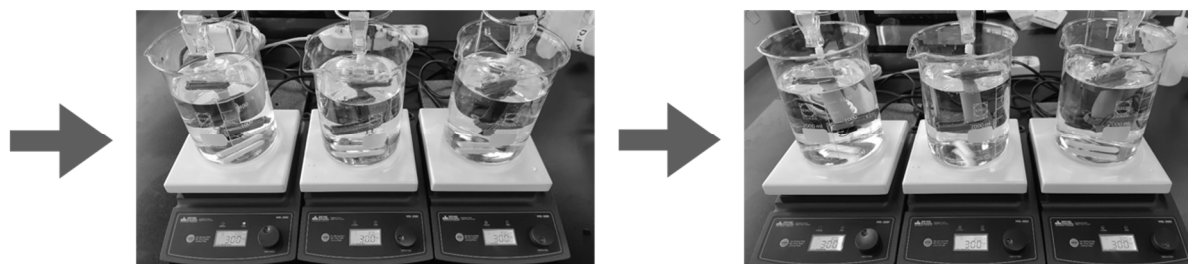
Dialysis

300 rpm, 12 h,
2 L x 4 of D.I. water to exchange

Figure 2-2. Schematic diagram of kraft lignin-based nanoparticle synthesis at four different pre-dialysis concentrations

2.4.2. Lignin fractions

Based on the pre-dialysis lignin concentration results in Section 3.2, KLFs were dissolved in THF at a fixed concentration of 2 mg mL^{-1}. Filtration with a 0.50 μm syringe filter was followed by a nanoprecipitation process with the THF solution's immersion in a dialysis tube in deionized water for 12 h with stirring at 300 rpm. Products were labeled as KLNP-F1, KLNP-F2, KLNP-F3, KLNP-F4, and KLNP-F5. Each variable was also run in triplicate. The yield of the particle was also calculated using Eq. (1).

2.5. Characterization of lignin nanoparticle

TEM imaging was performed with the use of an energy-filtering transmission electron microscope (LIBRA$^{®}$ 120, Carl Zeiss, Oberkochen, Germany). Nanoparticle samples were deposited on a thin carbon-coated copper 400 mesh TEM grid, followed by solvent evaporation.

Particle size, polydispersity (PDI), and electrokinetic potential in colloidal dispersion by DLS were calculated using a Zetasizer Nano ZS instrument (Malvern Panalytical Ltd., Worcestershire, UK). The samples were diluted in deionized water (approximately 0.2 mg mL^{-1}) and were measured at a constant temperature of 25 °C. For size calculation, both peak size and Z-average size (harmonic intensity averaged size) were presented. The measured electrokinetic potential values were converted into zeta potential using Smoluchowski's formula (Hunter, 2013). Averaging measurements of three samples obtained each value.

The stability of colloidal KLNPs by pre-dialysis concentration in pure water was analyzed by measuring the particle peak size (peak with the highest intensity) and zeta potential at different times (up to 28 days) using the Zetasizer Nano ZS.

2.6. Biocompatibility tests

2.6.1. CCK-8 assay

The biocompatibility of KLNPs (C2, F1, F2, and F3) on A549 cells (ATCC®, CCL-185™, Manassas, VA, USA) and Lewis Lung Carcinoma cells (LLC, ATCC®, CRL-1642™) was ascertained by Cell Counting Kit-8 (CCK-8) assays (Figure 2-3). The cells were first grown in Dulbecco's Modified Eagle Medium (DMEM, Thermo Fisher Scientific, Waltham, MA, USA) containing 10% fetal bovine serum (FBS, Atlas Biologicals, Fort Collins, CO, USA) and 1% Antibiotic-Antimycotic solution (GeneDireX, Las Vegas City, NV, USA). The cells were seeded onto 96-well plates (3×10^3 cells per well) and attached overnight. The medium was removed, and a series of serum-free DMEM containing 1% Antibiotic-Antimycotic and KLNPs with various concentrations (25, 50, 100, and 250 μg mL^{-1}) were added and further cultured for 24, 48, or 72 h. To examine cell viability, 10 μL of CCK-8 (Dojindo Molecular Technologies Inc., Kumamoto, Japan) was then added into each well and incubated for 3 h at 37 °C. Subsequently, the absorbance at 450 nm was measured using a microplate reader (Sunrise™, TECAN Group Ltd., Männedorf, Switzerland). Cells incubated with DMEM supplemented with 10% FBS and 10% Triton X-100 (TX, LPS solution, Daejeon, Republic of Korea) were used as positive and negative controls, respectively. Three replicates were used for each assay. All results were reported as the mean ± standard deviation.
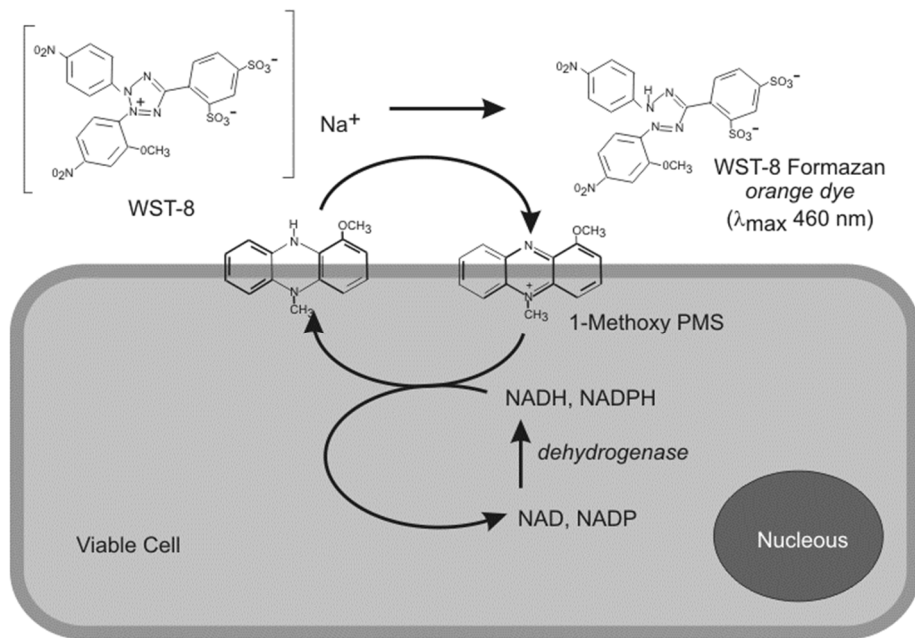
Figure 2-3. Cell viability detection mechanism with CCK-8 (Held, 2009)

2.6.2. Hemolysis assay

The fresh whole blood samples (0.6 mL) were collected from rats by tail-vein or retro-orbital blood collection. An anticoagulant (BD Vacutainer® K$_2$EDTA 5.4 mg, BD Life Sciences, Franklin Lakes, NJ, USA) was added immediately and used within 0.5 h. After centrifuging (2,140 rpm, 2 min at room temperature), the red blood cells (RBCs) were washed until the supernatant was clear and diluted by phosphate-buffered saline (PBS) to obtain a 5×10^8 cell mL^{-1} suspension. Different concentrations (200, 400, and 800 µg mL^{-1}) of the samples (KLNP, KLNP-F1, KLNP-F2, and KLNP-F3) were mixed with 1 mL of RBC suspension and incubated for 1 h at 37 °C. The negative and positive controls were pure PBS and 1% TX in PBS, respectively. After centrifuging (3,090 rpm, 2 min at room temperature), the hemoglobin releases were detected at 540 nm using a SpectraMax® iD3 multi-mode microplate readers (Molecular Devices, San Jose, CA, USA). The hemolytic degree was expressed by the hemoglobin release as the following Eq. (2):

$$Hemoglobin\ release\ (\%) = (OD_{sample} - OD_{negative})/(OD_{positive} - OD_{negative}) \times 100 \quad (2)$$

where OD is a calculated optical density value.

2.7. Statistical analysis

Statistical differences among groups were analyzed by analysis of variance (ANOVA), and multiple t-tests were performed to compare differences between the two groups. A p-value of <0.05 was considered significant.

3. Results and discussion

3.1. Characteristics of lignin fractions

KL was sequentially fractionated with five kinds of organic solvent with different solubilities. KL completely dissolved in the dioxane-water mixture. The yields of the five fractions were 33.1, 26.3, 7.4, 9.0, and 24.3 wt%, respectively (Table 2-4). The number average molecular weights (M_n) and weight average molecular weights (M_w) of KL and its fractions were determined by GPC (Table 2-4 and Figure 2-4). KL had varied sizes of molecules with M_w of 4,580 Da and dispersity (M_w/M_n) of 3.1. After fractionation, each KLF had a decreased M_w/M_n compared to KL. The M_w values of KLF increased from 1,460 Da for KL-F1 to 12,900 Da for KL-F5 as the sequential extraction progressed. These results agree with previous studies of successive lignin solvent extractions (An et al., 2017; Kim et al., 2017; Park et al., 2018b). It is assumed that the low-molecular-weight lignin compounds dissolve better than the high ones in the organic solvent. On the other hand, KL-F1 to F4 had relatively low M_w/M_n values of 1.7~1.8, and F5 had a lower but similar M_w/M_n of 2.8 compared to KL.

Table 2-4. The fractions yield of kraft lignin (KL) and their GPC information

	Yield (%)	M_w	M_n	M_w/M_n
KL		4,580	1,490	3.1
KL-F1	33.1	1,460	830	1.8
KL-F2	26.3	3,340	2,000	1.7
KL-F3	7.4	3,460	2,080	1.7
KL-F4	9.0	6,760	3,650	1.9
KL-F5	24.3	12,900	4,620	2.8
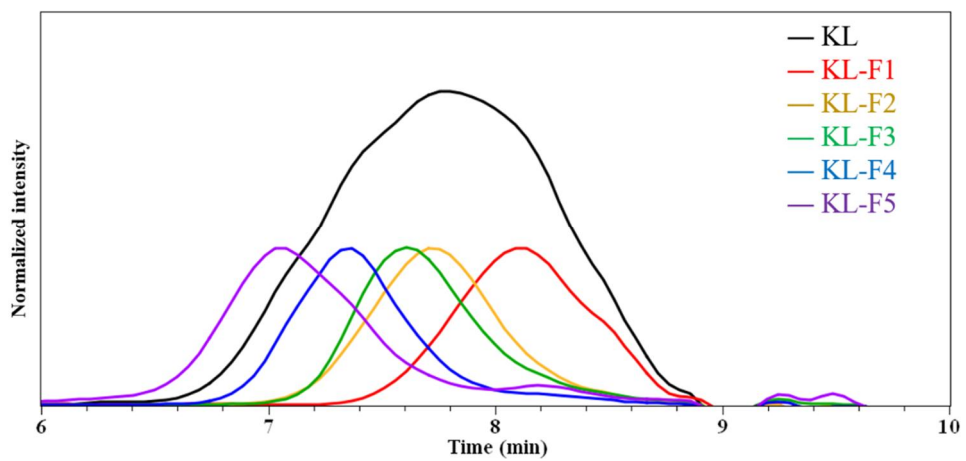
Figure 2-4. GPC curves of KL and its fractions by solvent extraction

Functional group content (methoxyl and hydroxyl) of KLFs was quantitatively determined, and the results are shown in Table 2-5; hydroxyl group (132~150 ppm) regions of ^{31}P NMR spectra are shown in Figure 2-5. The results indicate that the content of total hydroxyl groups decreased as the fractionation progressed. Phenolic hydroxyl groups significantly decreased from 4.39 mmol g^{-1} for KL-F1 to 1.00 mmol g^{-1} for KL-F5. Carboxylic group content also decreased from 0.83 mmol g^{-1} for KL-F1 to 0.25 mmol g^{-1} for KL-F5, whereas aliphatic hydroxyl groups increased from 1.02 mmol g^{-1} for KL-F1 to 2.52 mmol g^{-1} for KL-F5 throughout the process. The highest content of aliphatic hydroxyl groups was, however, obtained in KL-F3, followed by F5, F4, F2, and F1. A rationale for this tendency is not clear, but it might be related to the solvents' relative solvency behavior in this study. Hansen solubility parameters of the solvents are as follows: ethyl acetate (18.1), 2-butanone (19.1), methanol (29.6), acetone (20.0), and dioxane (20.5) (Barton, 2017).

Table 2-5. Content in hydroxyl groups of KL fractions quantified by ^{31}P NMR and methoxy group

	Hydroxyl (mmol g^{-1})						Methoxy
	Phenolic				Carboxylic acids	Aliphatic	(mmol g^{-1})
	H	G	Condensed				
			5-5	DPM*			
KL	0.09	1.86	0.32	0.39	0.48	2.03	4.92
KL-F1	0.16	3.26	0.28	0.69	0.83	1.02	5.12
KL-F2	0.08	1.68	0.36	0.47	0.47	1.65	4.99
KL-F3	0.07	1.44	0.22	0.20	0.47	2.86	4.79
KL-F4	0.04	1.17	0.26	0.22	0.34	2.28	4.73
KL-F5	0.02	0.79	0.12	0.07	0.25	2.52	4.04

* diphenylmethane
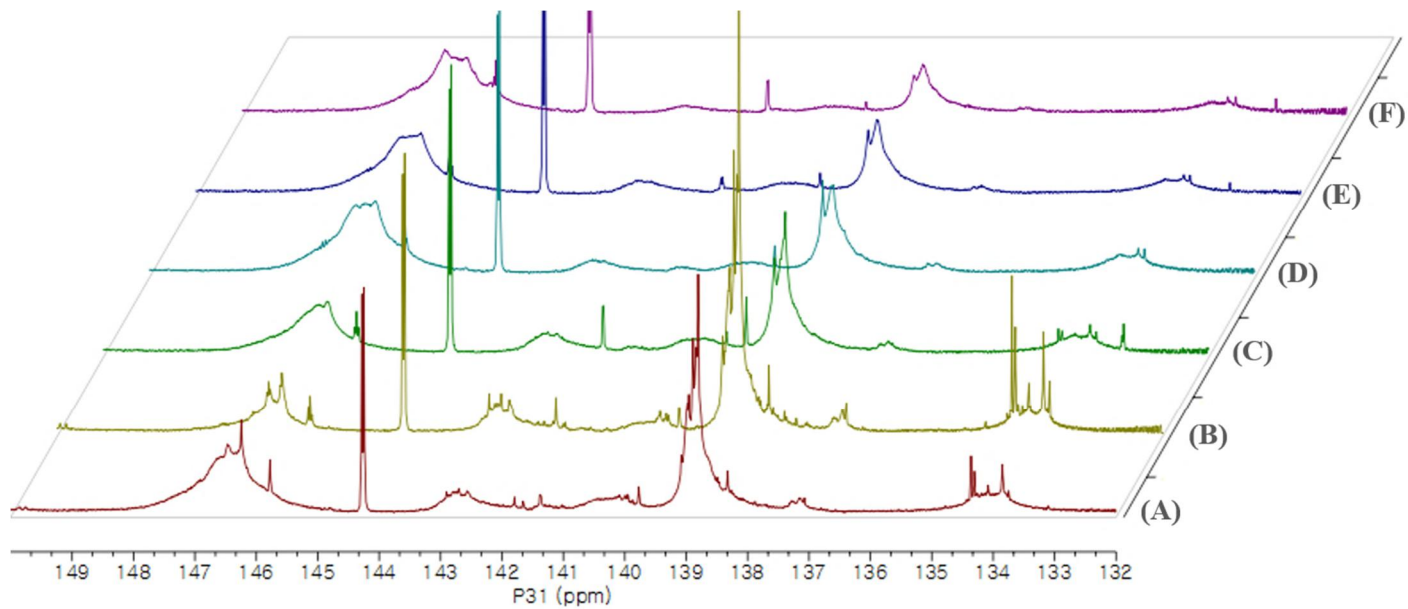
Figure 2-5. ^{31}P NMR spectra of (A) KL, (B) KL-F1, (C) KL-F2, (D) KL-F3, (E) KL-F4, and (F) KL-F5

Structures of KLFs, including the presence of aryl ethers as well as aromatic and aliphatic carbons, were elucidated by HSQC spectra consisting of cross-peaks of protons and carbons. The sidechain (δ_C/δ_H 50~90/2.5~6.0) and aromatic (δ_C/δ_H 100~135/5.5~8.0) regions of HSQC spectra are shown in Figures 2-6 and 7. Quantitative measurement of interunit linkages was carried out based on HSQC spectra with all of the aromatic units as an internal standard (Wen et al., 2013). The relative amount of β-aryl ether (β-O-4), resinol (β-β), and phenylcoumaran (β-5) of KL per 100 aromatic units were 6.4, 3.3, and 1.6, respectively (Table 2-6). In addition, the presence of lignin-carbohydrate linkages, β-D-xylopyranoside, was detected at δ_C/δ_H 72.5/3.05, 73.6/3.25, 75.3/3.56, and 63.2/3.24 (Wen et al., 2012). The relative amount of β-O-4, β-β, and β-5 in KL per 100 aromatic units were 6.4, 3.3, and 1.6, respectively. In the KL-F1 and F2 spectra, very weak cross signals of C_α–H_α were observed, which precluded the number of major linkages. This observation correlated with higher phenolic hydroxyl group content and indicates that KL-F1 and F2 are highly condensed phenolic oligomers. Interestingly, the M_w value and M_w/M_n of KL-F3 were similar to that of F2, but the interunit structure was significantly different. KL-F5 had the highest amount of β-O-4 linkage and the only β-D-xylopyranoside linkages among the lignin fractions. These results also might reflect the difference of solvation power between 2-butanone and methanol, as discussed above.
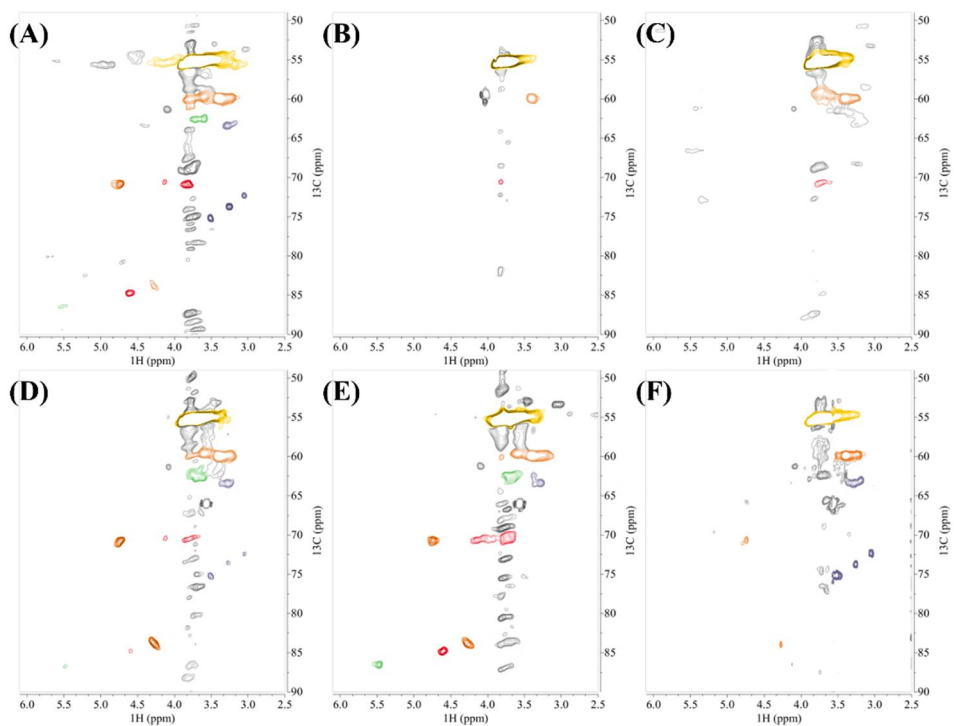
Figure 2-6. Sidechain regions in the 2D-HSQC NMR spectra of (A) KL, (B) KL-F1, (C) KL-F2, (D) KL-F3, (E) KL-F4, and (F) KL-F5; A_χ, C_χ-H_χ in β-O-4; B_χ, C_χ-H_χ in β-β; C_χ, C_χ-H_χ in phenylcoumaran; OMe, C-H in methoxyls; X_χ, C_χ-H_χ in phenyl glycoside linkages.
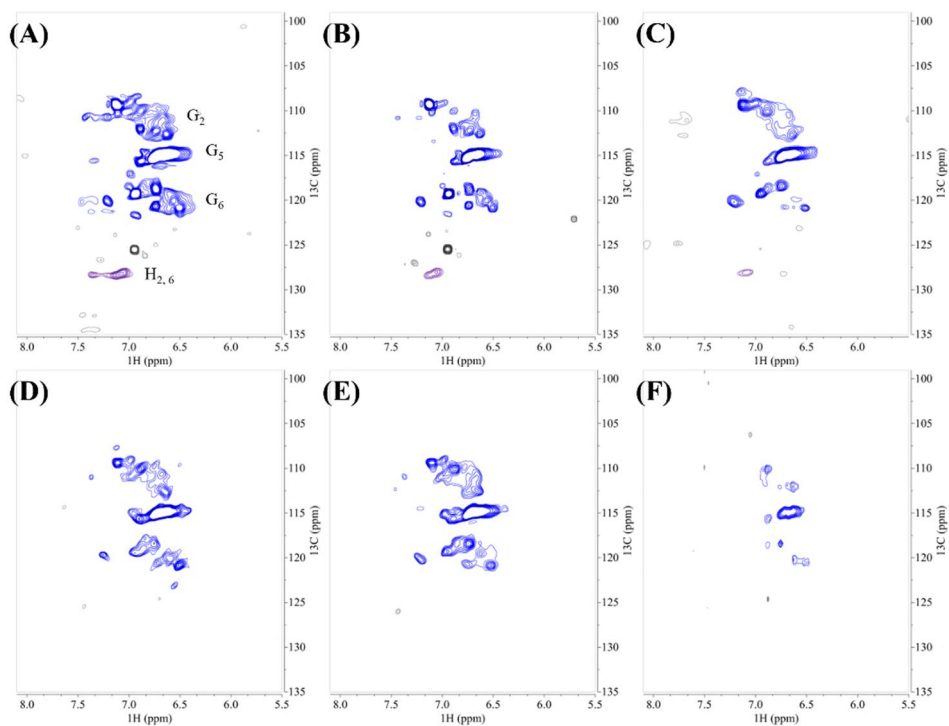
Figure 2-7. Aromatic/unsaturated regions in the 2D-HSQC NMR spectra of (A) KL, (B) KL-F1, (C) KL-F2, (D) KL-F3, (E) KL-F4, and (F) KL-F5; G_n, C_n–H_n in guaiacyl units; H_n, C_n–H_n in hydroxyphenyl units.

Table 2-6. Relative amounts of main interunit linkages in KL and its fractions

Samples	Linkage amount (per 100 aromatic units)			
	β-O-4	β-β	β-5	G:H
KL	6.4	3.3	1.6	95:5
KL-F1	ND[*]	ND	ND	94:6
KL-F2	ND	ND	ND	97:3
KL-F3	12.3	1.8	1.3	100:0
KL-F4	10.3	7.7	5.8	100:0
KL-F5	20.8	ND	ND	100:0

[*] not detected

3.2. Particle size and morphology

Figure 2-8 represents the recovery of resultant KLNPs, which were sedimentated and freeze-dried. All the samples had a high nanoparticle yield, from 89.7% for KLNP-F4 to 96.0% for KLNP-F1, a total average yield of 94.0%. There was no unique relationship between the yield of KLNP and pre-dialysis initial concentrations or fractions of KL. Compared to lower nanoparticle yields (43.8~64.9 %) from the similar nanoprecipitation process using lignin (Pang et al., 2020), the different recovery methods could induce the high particle yield (Bilati et al., 2005).

The pre-dialysis concentration of KL influenced the average particle size and distribution of nanoparticles. The smallest Z-average size of 272 nm was obtained at 2 mg mL^{-1} concentration (Table 2-7 and Figure 2-9). Moreover, KLNP-C2 showed the smallest gap between the peak and Z-average size among all nanoparticles. This finding indicates that KLNP-C2 is the least polydisperse state among the samples since the Z-average size is very sensitive and could be comparable with the peak size if the particle is monomodal, spherical in shape, and monodisperse in a suitable dispersant. On the other hand, the peak size, a mean size for each separate size peak of the distribution, and its width were enlarged as the lignin concentration increased. This result is in agreement with previous work on the nanoprecipitation of several synthetic polymers (Badri et al., 2017; Dong & Feng, 2004; Lince et al., 2008) and lignin (Lievonen et al., 2016). It is well known that a higher polymer concentration leads to the higher viscosity of the solution, which involves longer mixing time to form larger nanoparticles (Chorny et al., 2002; Limayem Blouza et al., 2006). Polymer concentration also contributes to particle growth with respect to particle nucleation (Martinez Rivas et al., 2017). Peak sizes and pre-dialysis concentrations were very highly correlated ($R^2 = 0.94$).
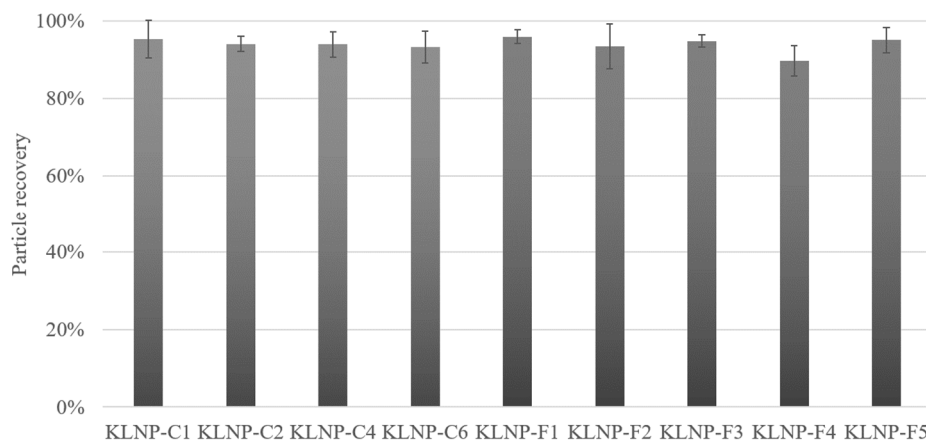
Figure 2-8. Recovery of nanoparticles as functions of initial KL concentration and fractionation

Table 2-7. Main properties of lignin fraction-derived nanoparticles

	Peak size (nm)				Z-average size	PDI	Zeta potential
	Peak 1	Intensity (%)	Peak 2	Intensity (%)	(nm)		(mV)
KLNP-C1	193	100	-	-	380.5	0.395	-42.6 ± 1.4
KLNP-C2	274	100	-	-	272.0	0.284	-38.6 ± 0.2
KLNP-C4	389	100	-	-	473.0	0.313	-36.7 ± 0.2
KLNP-C6	712	100	-	-	461.0	0.275	-29.1 ± 0.4
KLNP-F1	1,039	100	-	-	1,039	0.042	-44.5 ± 2.3
KLNP-F2	848	100	-	-	1,121	0.330	-40.7 ± 0.3
KLNP-F3	732	96.4	5,484	3.6	1,311	0.353	-42.9 ± 0.6
KLNP-F4	530	78.3	3,339	21.7	533.0	0.376	-39.0 ± 0.4
KLNP-F5	767	90.8	145	7.8	632.9	0.381	-36.3 ± 0.4
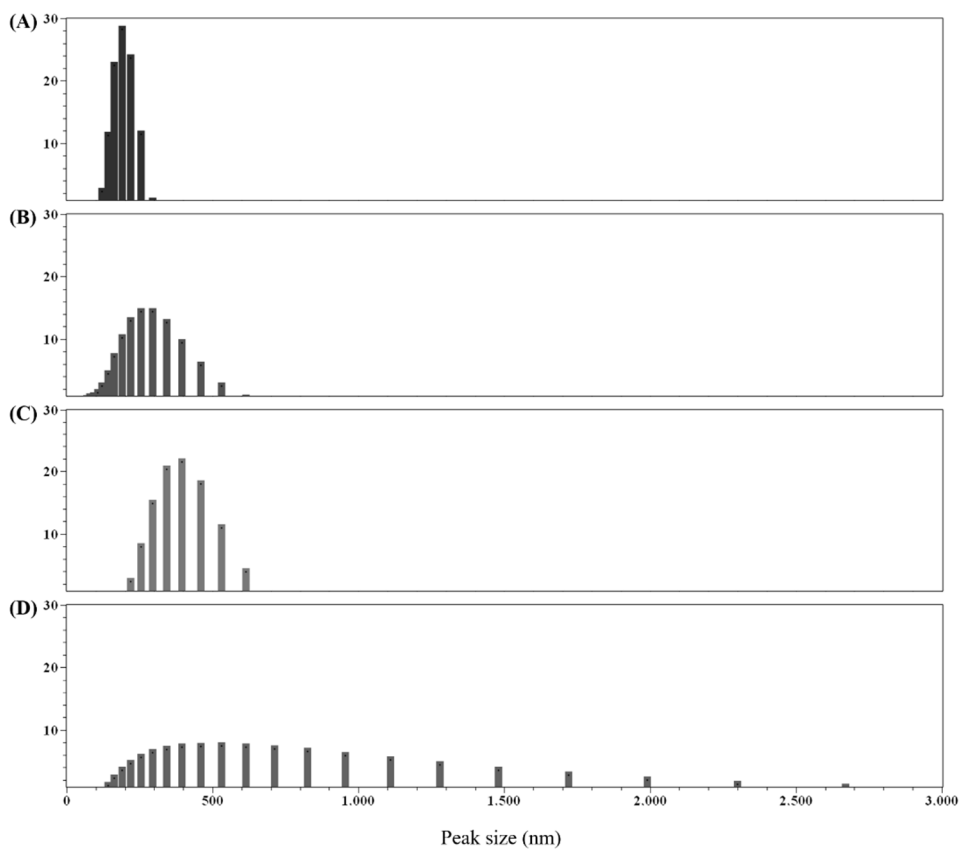
Figure 2-9. Peak size graph of KLNPs with different pre-dialysis concentrations. (A) KLNP-C1, (B) KLNP-C2, (C) KLNP-C4, and (D) KLNP-C6.

The average particle size, shape, and distribution of lignin nanoparticles were affected by the fractionation step. As shown in Table 2-7, all of the particles of each KLF had a significantly bigger size compared with the control group (KLNP-C2). In detail, larger nanoparticles consisted of fractions of lower M_w and higher hydrophilic functional group content, while smaller particles with multi-peak size distribution were obtained from fractions of higher M_w and higher hydrophobic group content (Figure 2-10). Upon replacing THF with water, the lignin fraction's higher hydrophilic character increases its interaction with water molecules, resulting in the need for a large amount of lignin to form nanoparticles. Additionally, it is assumed that hydrogen bonding with phenolic hydroxyl and carboxyl groups can boost layer-by-layer self-assembly, a possible formation mechanism for lignin nanoprecipitation (Salentinig & Schubert, 2017; Xiong et al., 2017). While KL and KL-F1 displayed similar hydrophilic group content, the size of the resulting particles, KLNP-C2 and KLNP-F1, were different (272 and 1,039 nm, respectively). The relatively short and uniform structures of KLFs demand a larger polymer amount to self-assemble than the raw lignin.

The correlations between particle sizes and several features of the lignin are presented in Figure 2-11. There were no high correlations between particle size and structural characteristics of KLFs since KLNP-F4 and F5 are highly polydispersed and/or not formed regularly. Instead, less polydisperse groups (KLNP-F1, F2, and F3) highly correlate with the particle size. M_w ($R^2 = 0.89$) and total hydroxyl group content in the lignin ($R^2 = 0.99$) are highly correlated with the average peak size of KLNP-Fs. Therefore, it could be assumed that the hydrogen bond formation between hydroxyl groups encourages nucleation or condensation during the nanoprecipitation process. However, the aliphatic hydroxyl group and β-O-4 linkages did not correlate with the particle size ($R^2 = 0.30$ and 0.05, respectively).

TEM images determined the morphology of KLNPs in water. Figure 2-12 shows representative TEM images of nanoparticles synthesized from each

fractionated lignin. Nearly spherical shaped particles were obtained, while KLNP-F5 had some irregular and cracked sphere morphological structures, which merits further discussion.
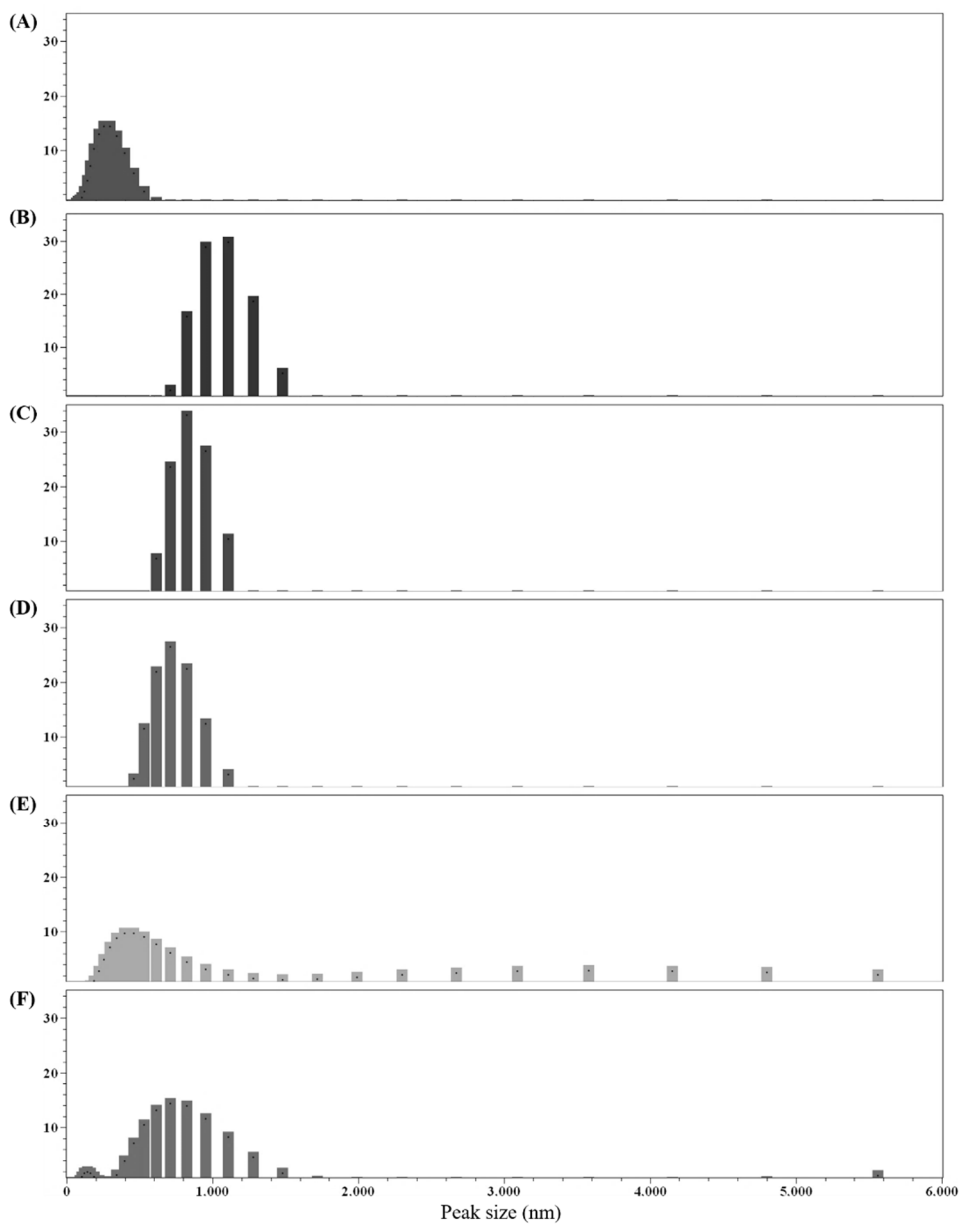
Figure 2-10. The peak size distribution of KLNPs with lignin fractions. (A) KLNP-C2, (B) KLNP-F1, (C) KLNP-F2, (D) KLNP-F3, (E) KLNP-F4, and (F) KLNP-F5.
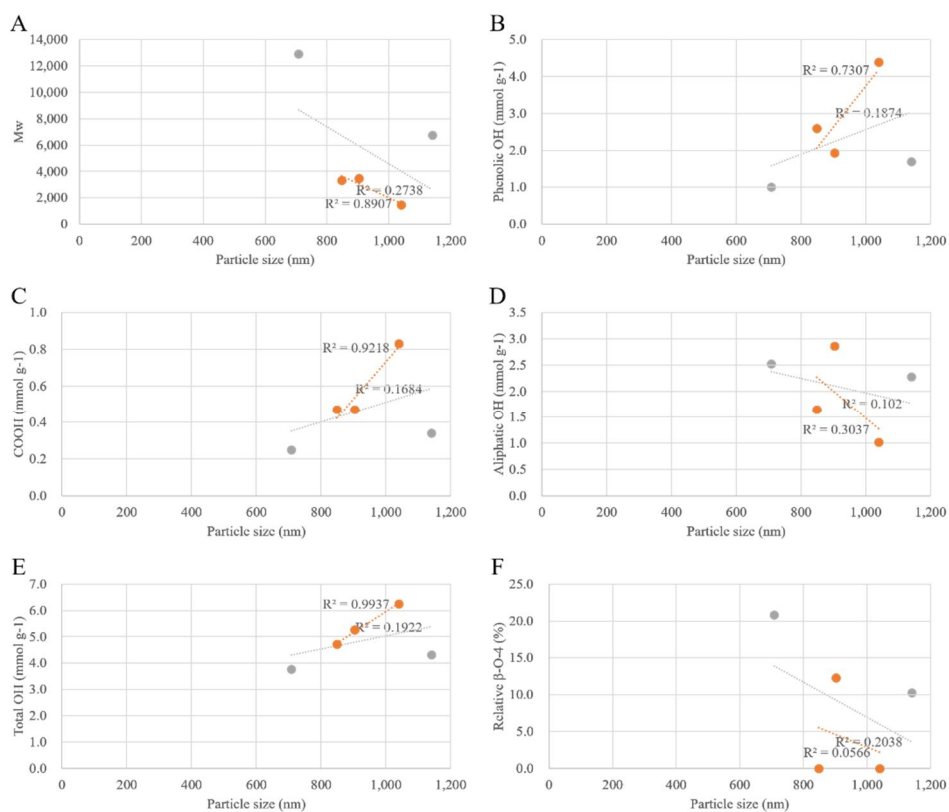
Figure 2-11. Peak average size distribution of KLNPs as functions of structural characteristics. (A) M_w, (B) phenolic hydroxyl, (C) carboxylic acid, (D) aliphatic hydroxyl, (E) total hydroxyl content, and (F) relative β-O-4. Orange dots represent the properties of KLNPs with monomodal size distribution (KLNP-F1, F2, and F3). Achromatic dots represent the properties of KLNPs with multimodal size distribution (KLNP-F4 and F5)
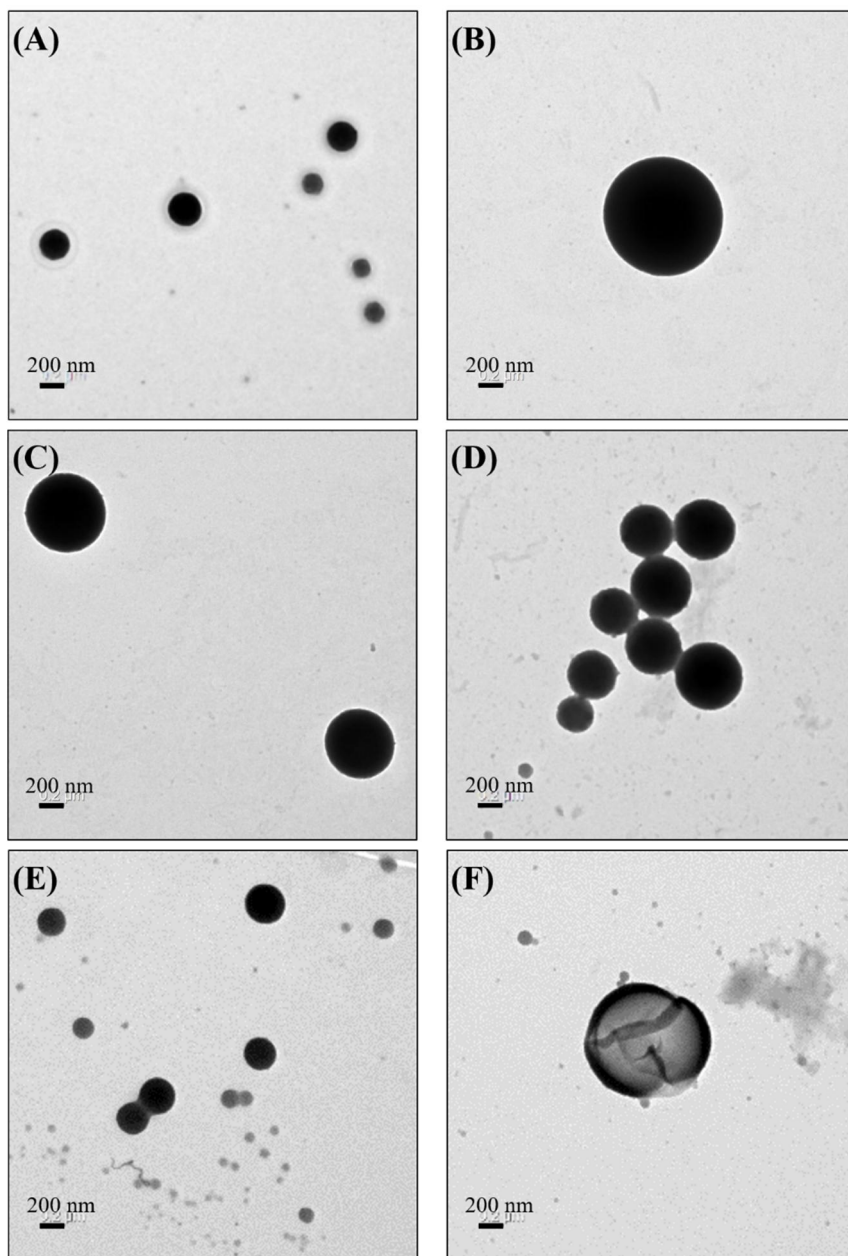
Figure 2-12. TEM images of (A) KLNP-C2, (B) KLNP-F1, (C) KLNP-F2, (D) KLNP-F3, (E) KLNP-F4, and (F) KLNP-F5

3.3. Particle surface charge

Zeta potential is one of the important characteristics in evaluating the physical stability of colloidal systems (Kumar & Dixit, 2017). Mainly nanoparticles with a zeta potential outside -30 mV to 30 mV have a high degree of colloidal stability. In this study, zeta potential values for all samples except KLNP-C6 exceeded -35 mV, indicating relatively high water stability. The pre-dialysis concentration of lignin strongly negatively affected zeta potential (R^2 = 0.94). But no significant trend of changing zeta potential value concerning the size of KLNP was observed (Table 2-7), although it has been reported that zeta potential increases with increasing particle size (Fairhurst, 2013; Hyam et al., 2008).

3.4. Storage stability of the particle in pure water

The storage stability of colloidal nanoparticles is an important issue of the processes and applications. To investigate the stability in terms of size and surface chemistry of KLNPs, peak size and zeta potential were analyzed at different times.

Stability tests of KLNP-Cs showed slight particle size changes, representing the most problematic aggregation issue during suspension storage, after 28 days of storage in deionized water (Table 2-8 and Figure 2-13). Peak 1 size of KLNP-C2 and C4 grew with time, less than 3% per week (2.4% and 2.1%, respectively), while the size of KLNP-C1 and C6 increased more rapidly (4.5% and 3.5%, respectively). However, since the increase rates are still low, there is no significant particle size instability with long-time storage.

The surface charge of the lignin nanoparticles decreased over time (Figure 2-13). The zeta potential value of KLNP-Cs increased with time from -42.6, -38.6, -36.7, and -29.1 mV to -38.4, -34.2, -33.9, and -25.4 mV, respectively. The relatively high negative zeta potential, less than -30 mV, induces sufficient electrical repulsion between the lignin particles to hinder growth by coagulation. As a result, the lignin nanoparticle dispersion was very stable in pure water, and no specific collision and condensation occurred within 28 days.

Table 2-8. Summary of kraft lignin nanoparticle stability in the pure water of change in time

		Days after synthesis					
		0 days	3 days	7 days	14 days	21 days	28 days
Peak 1 size (nm)	KLNP-C1	193 ± 18	220 ± 47	210 ± 45	223 ± 26	224 ± 48	228 ± 22
	KLNP-C2	274 ± 52	253 ± 39	280 ± 63	283 ± 82	300 ± 55	292 ± 40
	KLNP-C4	389 ± 47	387 ± 73	422 ± 89	418 ± 91	422 ± 73	421 ± 104
	KLNP-C6	712 ± 272	750 ± 77	748 ± 159	770 ± 90	782 ± 108	813 ± 68
Zeta potential (mV)	KLNP-C1	-42.6 ± 1.4	-37.9 ± 1.2	-37.6 ± 0.4	-38.3 ± 0.9	-39.1 ± 0.4	-38.4 ± 1.5
	KLNP-C2	-38.6 ± 0.2	-37.3 ± 0.3	-37.8 ± 0.8	-37.4 ± 0.6	-34.4 ± 1.1	-34.2 ± 1.0
	KLNP-C4	-36.7 ± 0.2	-35.1 ± 0.6	-35.1 ± 0.7	-36.6 ± 0.7	-32.6 ± 0.7	-33.9 ± 1.7
	KLNP-C6	-29.1 ± 0.4	-28.4 ± 0.6	-25.9 ± 0.5	-26.3 ± 0.8	-26.0 ± 0.1	-25.4 ± 0.7
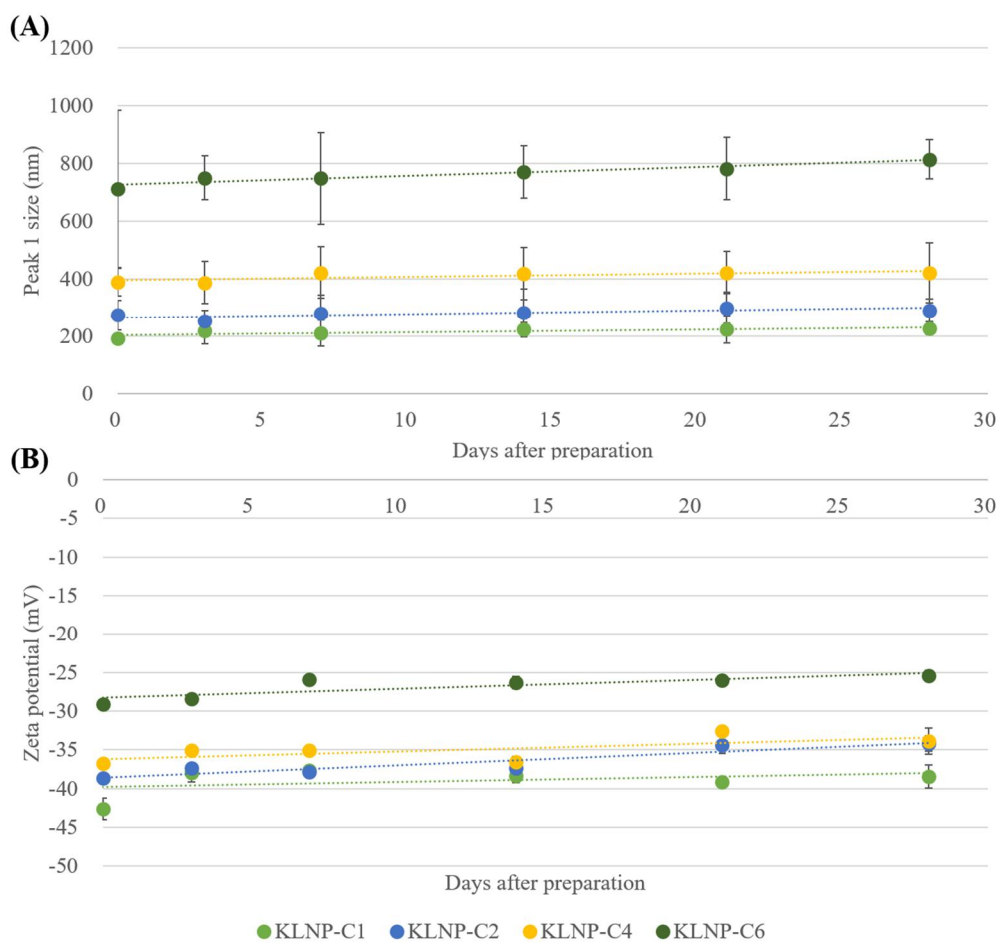
Figure 2-13. (A) Peak size and (B) zeta potential stability of KLNP-Cs in pure water as a function of time

3.5. *In vitro* cell viability

Cell viability assessment is widely used to measure the cytotoxicity of nanoparticles. Various studies have revealed cytotoxicity correlated with the size, shape, surface charge, chemical composition, and aggregation properties of carbon/polymer nanoparticles (Kumar & Dixit, 2017; Lewinski et al., 2008). Thus, the cytotoxicity of KLNPs in A549 and LLC cell lines by the CCK-8 assay was evaluated.

Generally, KLNPs exhibited extremely low cytotoxicity to A549 cell lines at concentrations of 25 and 50 µg mL^{-1} (Figure 2-14). In addition, nanoparticles synthesized from fractionated KLs showed good biocompatibility in all concentrations that were tested (Figure 2-14B–D). However, KLNP without fractionation represented relatively low biocompatibility, particularly at higher concentrations (Figure 2-14A). Generally, it can be inferred that large particle size may have reduced cell viability (Yoshioka et al., 2016). There were no clear correlations, in this case, between the particle size of KLNPs and A549 cell viability. In comparison, it is very hard to determine the cytotoxicity of KLNPs because most of the A549 cells in the control group disappeared within 72 h. It could be triggered by serum starvation causes apoptosis-induced cell death (Rashid & Coombs, 2019). Interestingly. A549 cell lines with KLNPs exhibited a much higher survival rate even after 72 h compared with the serum-free control. Several researches reported that the lignin-polymer scaffold as an antioxidant and subsequent oxygen-free radical scavenging properties is applied for nerve regeneration (Ugartondo et al., 2009; Wang et al., 2018). Therefore, further study is required to prove that the cell lines in the presence of KLNPs do not die without FBS.

The LLC cell lines were also ascertained by CCK-8 assay for 72 h. However, LLC in blank control (serum-free DMEM) died after 24 h (Figure 2-15). Since KLNP-introduced cell lines showed higher viability than in blank control, it was

difficult to determine the relative cell viability for 48 and 72 h (Azouz et al., 2008; Kundranda et al., 2005). Next, the cytotoxicity of KLNPs in LLC was examined. LLC cell lines were incubated with KLNPs for 8, 16, and 24 h, and their viability was measured. While there was no remarkable change in cell viability with any of the samples until 16 h, KLNP-C2 led to a marked decrease in cell viability (Figure 2-16A). However, the cell proliferation with KLNP-C2 almost recovered within 24 h. As a result, raw kraft lignin-based nanoparticles caused weak or no significant cytotoxicity at concentrations up to 250 µg mL^{-1} for 72 h (A549 cell line) or 24 h (LLC cell line).
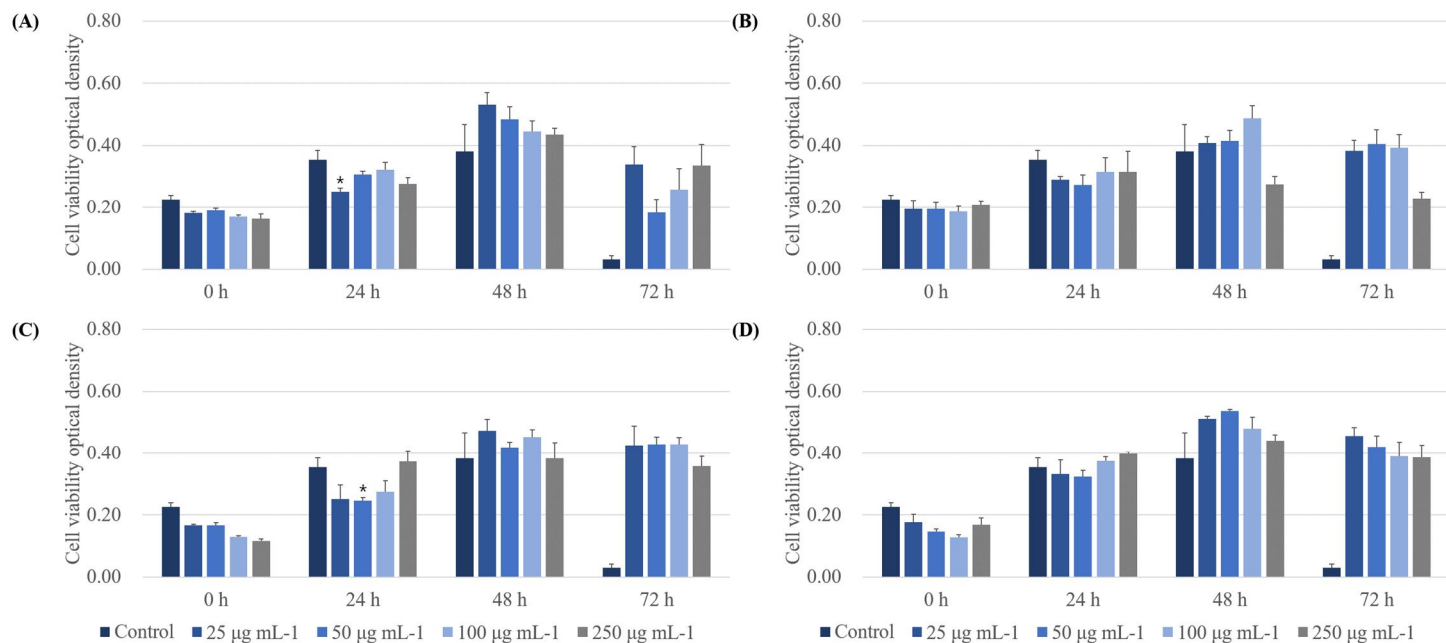
Figure 2-14. Cytotoxic effects of KLNPs on A549 cells. (A) KLNP-C2, (B) KLNP-F1, (C) KLNP-F2, and (D) KLNP-F3. The viability was determined by the Cell Counting Kit-8 assay, and all data sets were compared to the control (serum-free DMEM containing 1% of Antibiotic-Antimycotic). The data are presented as the mean ± standard deviation of three independent experiments. The level of the significant differences was set at probabilities of $*p < 0.05$, $**p < 0.01$, and $***p < 0.001$.
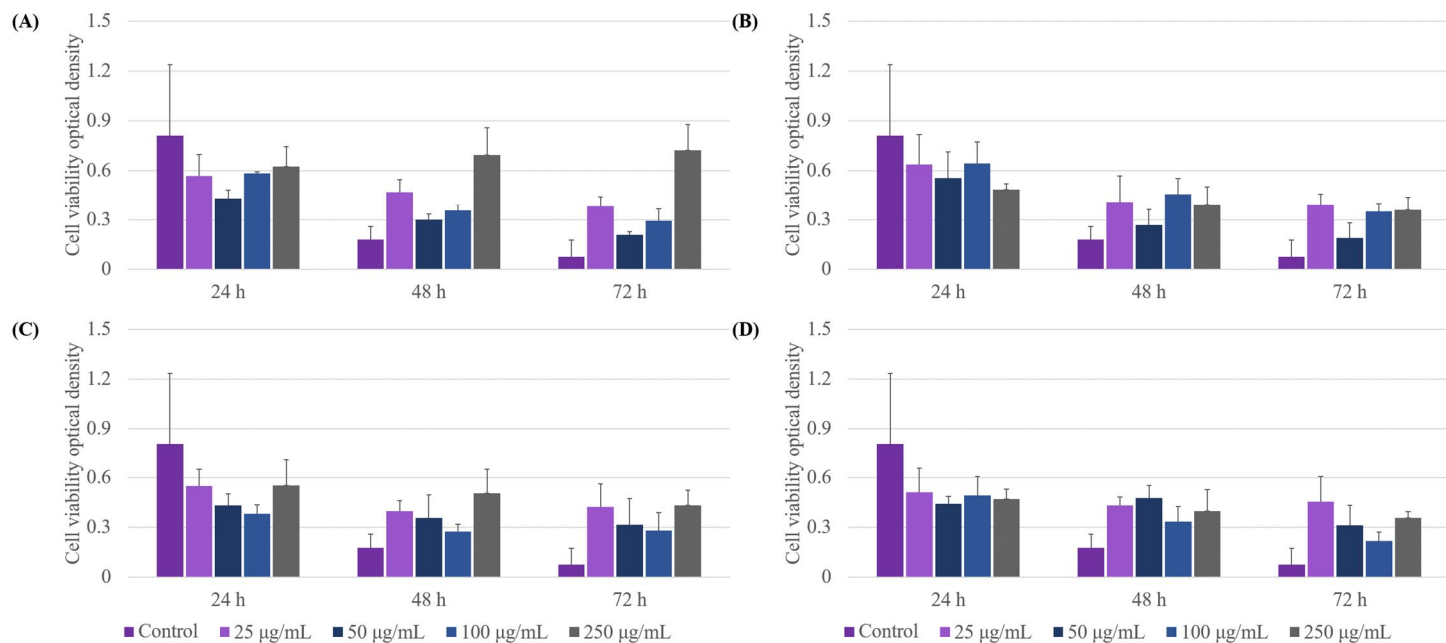
Figure 2-15. The measured absorbance values of CCK-8 assay of LLC cells in the presence of KLNPs as a function of time (24, 48, and 72 h). (A) KLNP-C2, (B) KLNP-F1, (C) KLNP-F2, and (D) KLNP-F3. All data sets were compared to the blank control (serum-free DMEM containing 1% of Antibiotic-Antimycotic). The data are presented as the mean ± standard deviation of three independent experiments.
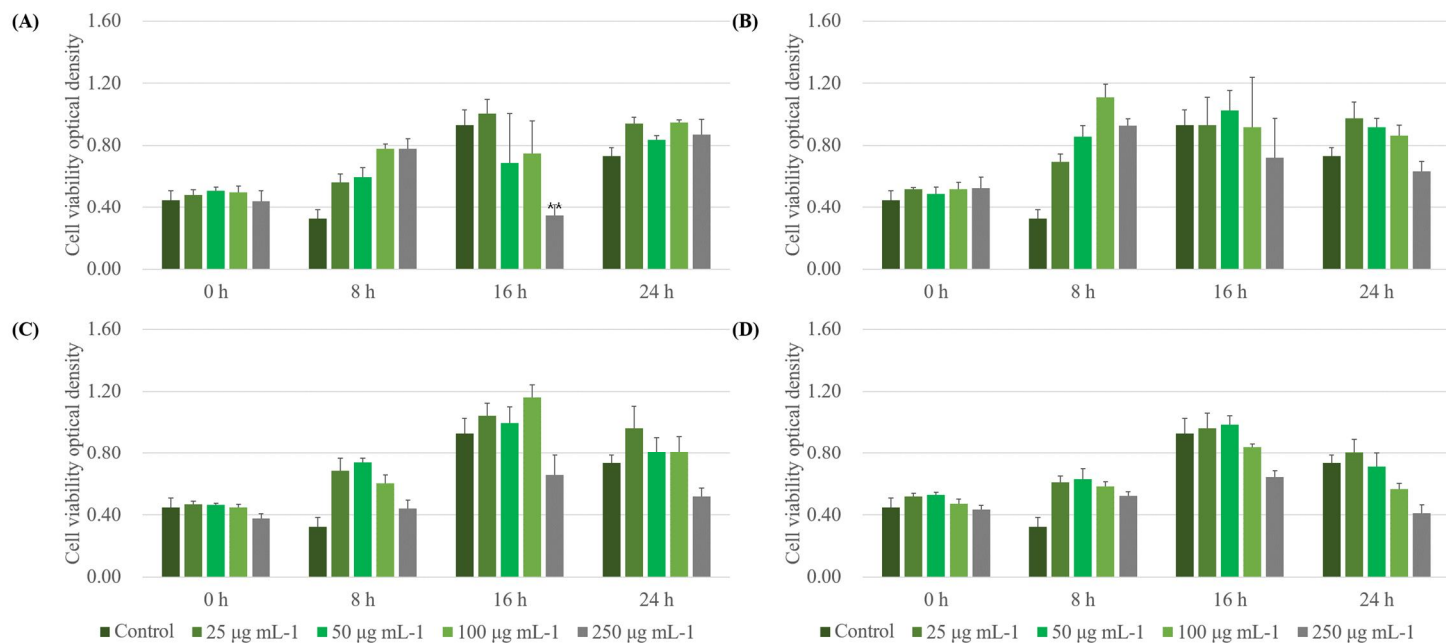
Figure 2-16. Cytotoxic effect of KLNPs on LLC cells. (A) KLNP-C2, (B) KLNP-F1, (C) KLNP-F2, and (D) KLNP-F3. The viability was determined by the Cell Counting Kit-8 assay, and all data sets were compared to the blank control (serum-free DMEM containing 1% of Antibiotic-Antimycotic). The data are presented as the mean ± standard deviation of three independent experiments. The level of the significant differences was set at probabilities of $*p < 0.05$, $**p < 0.01$, and $***p < 0.001$.

3.6. Hemocompatibility

Hemolysis is a blood cell burst in circulation *in vivo* (Dobrovolskaia et al., 2008). Many nanoparticles can cause RBCs rupturing; thus, preclinical determination of hemolytic ability is needed for KLNPs with anticipated delivery modes having blood contact.

Hemolysis results were evaluated by hemoglobin release after exposure to different concentrations of KLNPs and are shown in Figure 2-17. For the four KLNPs tested, the hemoglobin releases were less than 10% for concentrations ranging from 200 to 800 μg mL^{-1}. In detail, the hemoglobin release of KLNP-C2 was $0.32 \pm 0.09\%$, $1.46 \pm 0.07\%$, and $5.70 \pm 0.31\%$ at 200, 400, and 800 μg mL^{-1}, respectively. On the other hand, the hemoglobin release profiles of KLNP-F1 and F2 at 200 μg mL^{-1} were found to be $0.34 \pm 0.13\%$ and $0.05 \pm 0.05\%$, respectively. They increased to $2.71 \pm 0.16\%$ and $0.22 \pm 0.04\%$ at 400 μg mL^{-1} and $4.45 \pm 0.29\%$ and $2.56 \pm 0.47\%$ at 800 μg mL^{-1}, respectively. The highest hemoglobin release of KLNP-F3 among the samples was identified to be $1.53 \pm 0.09\%$, $4.53 \pm 0.70\%$, and $8.09 \pm 0.28\%$ at 200, 400, and 800 μg mL^{-1}, respectively. It is well known that an *in vitro* hemolysis below 10% is considered non-hemolytic, while values higher than 25% are considered hemolytic (Amin & Dannenfelser, 2006). Even if taking the possibility of longer exposure time *in vivo* into consideration, it can be assumed that all the tested KLNPs are safe for possible use as a drug delivery system.
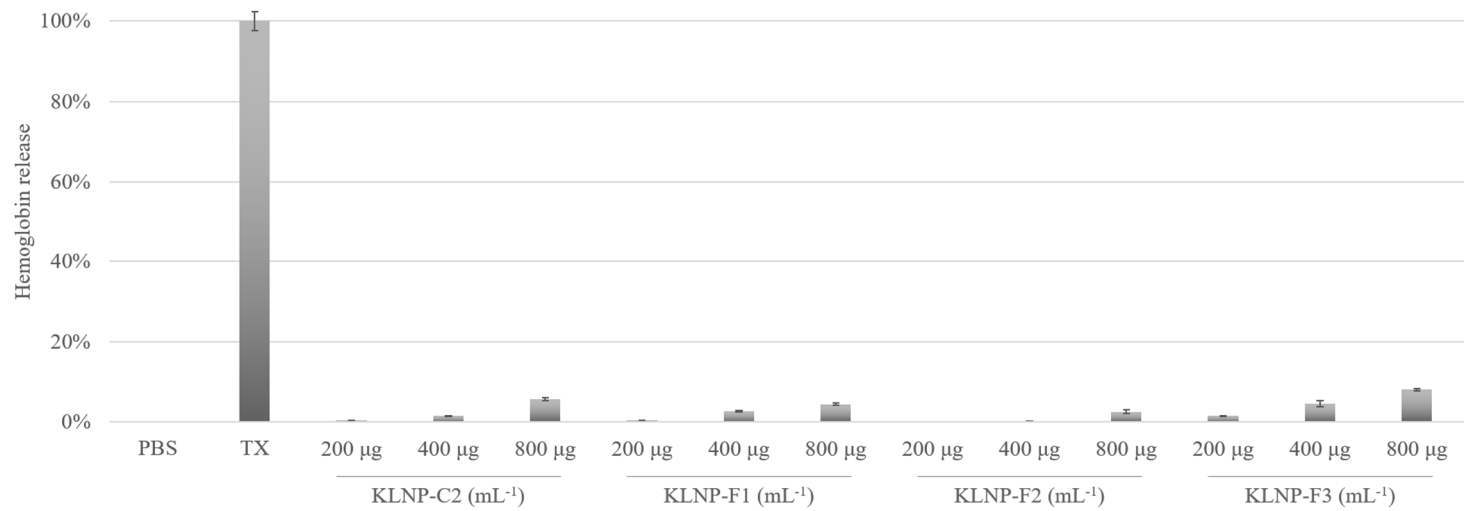
Figure 2-17. Hemoglobin release of KLNPs

4. Conclusion

In this study, sequential solvent extraction of KL was performed to obtain fractions with different molecular weights and structures, which were then handled to synthesize spherical pure lignin nanoparticles by nanoprecipitation. Comprehensive analysis indicated that the lignin fractions with small sizes of molecules contained a higher total amount of hydroxyl and methoxyl groups and relatively condensed structures compared to fractions with larger sized molecules. Unexpectedly, however, the low-molecular-weight fractions generated KLNPs with an enlarged diameter was in contrast with other polymer materials previously reported. It is assumed that the relatively short and uniform structure of the lignin molecule forms a larger nanoparticle. Although there was a significant size difference between each KLNP, they showed comparable and good colloidal stability. *In vitro* cell viability tests confirmed that KLNPs exhibited low cytotoxicity, which encourages the potential use of KLNPs as being appropriate for DDS, such as encapsulated nanoparticles or nano-sized drug conjugates. Consequently, lower molecular weight and higher hydroxyl group content in the lignin encouraged nanoparticle size growth during the nanoprecipitation process. On the contrary, the relatively irregular structure of raw KL demands a small amount of molecule to reach the end of condensation.

Chapter 3

In vivo and *in vitro* evaluation of drug-encapsulated lignin nanoparticles for release control

1. Introduction

In recent decades, the cancer survival rate has increased with special medical treatments, including surgery, chemotherapy, and radiotherapy. Among them, chemotherapy uses a number of agents called chemotherapeutic drugs that act against malignant tumors (DeVita & Chu, 2008). The chemotherapeutic drug is often classified into a traditional cytotoxic drug and a targeted drug (Aggarwal, 2010). Generally, conventional drug treatment exhibits strong anticancer effects but has some limitations. First, most chemotherapeutic drugs are hydrophobic. They require ideal non-water solvents to give an injection in the living organism, which can cause cell toxicity. Second, a non-targeted effect of cancer regression can cause critical damage to normal cells. Third, long-term chemotherapy can increase the drug-efflux pump on the cell membrane that increases multidrug resistance. Doxorubicin (DOX) as an intravenously-injected cytotoxic chemotherapeutic agent, for example, is on the World Health Organization's List of Essential Medicines and widely applied in therapeutic strategies such as combination chemotherapies (Table 3-1 and Figure 3-1A). However, repeated high-dose of DOX can cause multiple side effects such as pain, nausea, low blood counts, and fertility problems (Thorn et al., 2011). An uncommon but serious side effect of DOX is cardiotoxicity, which can trigger congestive heart failure at worst (Figure 3-1B).

To overcome the challenges of the adverse effect of chemotherapy, nanotherapeutic technology is needed for cancer treatment. Nanomedicine and nano-based drug delivery systems have several important advantages; longer shelf life and circulation time, improved biodistribution, controlled and sustained drug release, etc. (Patra et al., 2018; Tiwari et al., 2012). Among the systems, a polymeric nanoparticle is a promising encapsulation structure for drug delivery with up to several hundred nanometers in diameter (El-Say & El-Sawy, 2017). In recent years, nanoparticles have been preferably utilized because of their

controllable intracellular uptake and controlled drug-release ability (Couvreur, 2013; Li et al., 2019). Especially, controlled release by nanostructures of the particle allows the drugs to avoid premature release, reach the targeted site, and decrease side effects by minimizing exposure to normal locations of the body (Crucho & Barros, 2017; Mora-Huertas et al., 2010; Tiwari et al., 2012).

There are many types of chemotherapeutic drugs and/or drugs often used during chemotherapy. Each drug has a different molecular structure, hydrophilicity (or hydrophobicity), mechanism of action, and electric charge. Therefore, no single polymer can afford to form nanoparticles with all the cancer drugs. In addition, there is a rapid increase in demand for natural polymers that have sustainability at low cost, biodegradability, and/or biocompatibility (Idrees et al., 2020; Wurm & Weiss, 2014). Lignin is the second most abundant natural polymer containing polyphenolic structures. Due to its abundance and biocompatibility (Chen et al., 2018; Figueiredo et al., 2017; Kai et al., 2018), lignin is a promising polymer candidate for the synthesis of pharmaceutical drug-encapsulated nanoparticles (Chen et al., 2016; Dai et al., 2017; Figueiredo et al., 2017; Zhou et al., 2019).

This chapter, based on the results in the previous chapter, aimed to synthesize the nano-sized drug delivery system by nanoprecipitation of high-quality kraft lignin. Coumarin 6 (drug model compound) and DOX were chosen as the hydrophobic drug for encapsulation by lignin. After successful drug encapsulation, the size, surface charge, and releasing properties of encapsulated lignin nanoparticles (ELNPs) were determined. The relationship between the properties of lignin and derived nanoparticle were also examined. Their biocompatibility and antitumor efficacy were tested *in vitro* and/or *in vivo* to evaluate their antitumorigenic potential.

Table 3-1. Common combination chemotherapy regimens which doxorubicin (DOX) has participated (Corrie, 2008)

Type	Drugs
Breast cancer	DOX and cyclophosphamide
Hodgkin's lymphoma	Docetaxel, DOX, and cyclophosphamide
	DOX, bleomycin, vinblastine, and dacarbazine
Non-Hodgkin's lymphoma	Cyclophosphamide, DOX, vincristine, and prednisolone
Bladder cancer	Methotrexate, vincristine, DOX, and cisplatin
Lung cancer	Cyclophosphamide, DOX, vincristine, and vinorelbine
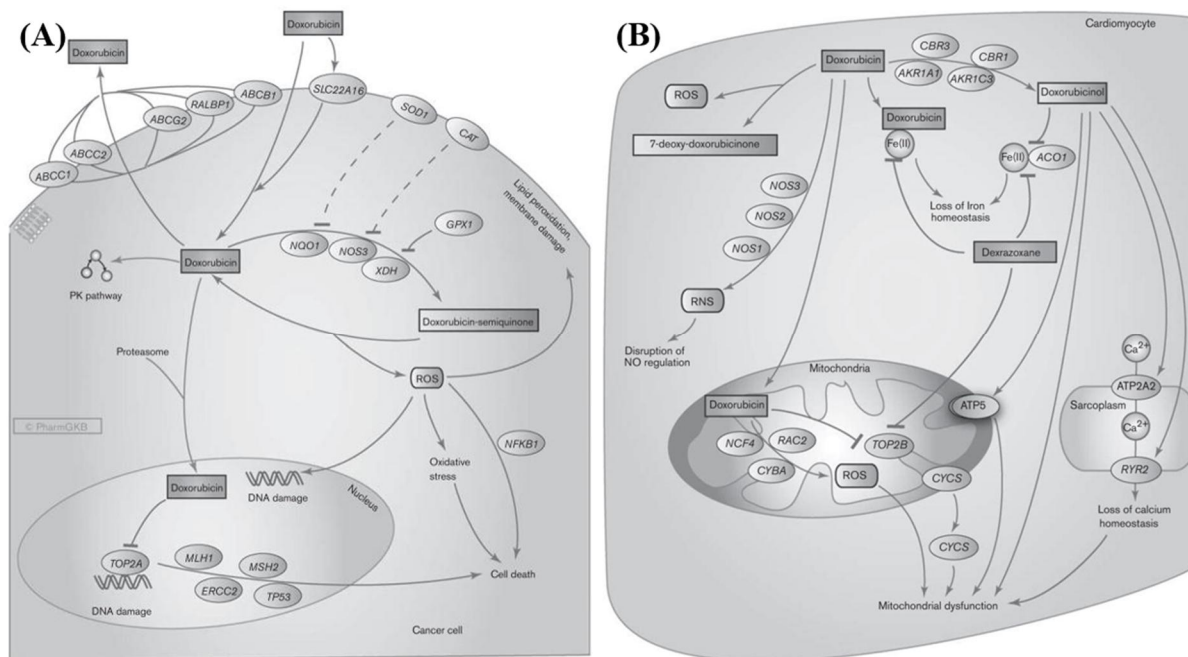
Figure 3-1. Graphical representation of proposed mechanisms by which DOX acts in the (A) cancer cell and (B) cardiomyocytes (Thorn et al., 2011)

2. Materials and methods

2.1. Materials

A commercial pine kraft lignin (BioChoice® Lignin, KL) extracted by the LignoBoost process was provided by Domtar Inc., Plymouth, NC, USA. Ethyl acetate-soluble fraction of KL (KL-F1) was obtained applying Park's method, as described in the previous chapter (Park et al., 2018b).

Coumarin 6 (Figure 3-2) as a hydrophobic drug model compound, ethyl acetate, tetrahydrofuran (THF), triethylamine (TEA), dimethyl sulfoxide (DMSO), and the dialysis tubing (molecular weight cut-off 14,000 Da) were purchased from Sigma-Aldrich Korea (Yongin, Republic of Korea).

Doxorubicin hydrochloride (DOX·HCl) was purchased from Tokyo Chemical Industry Co., Ltd. (Tokyo, Japan). It was deprotonated to obtain a hydrophobic free base of DOX (Figure 3-2). DOX·HCl was stirred with a 3-mole ratio of TEA in DMSO overnight under darkroom conditions to remove hydrochloride (Kim et al., 2008; Nittayacharn et al., 2020).

(A)
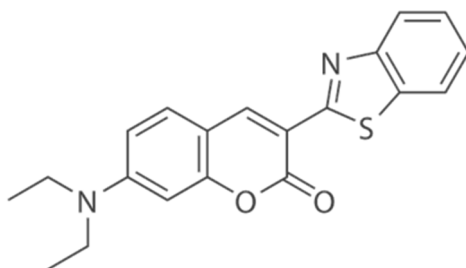
(B)
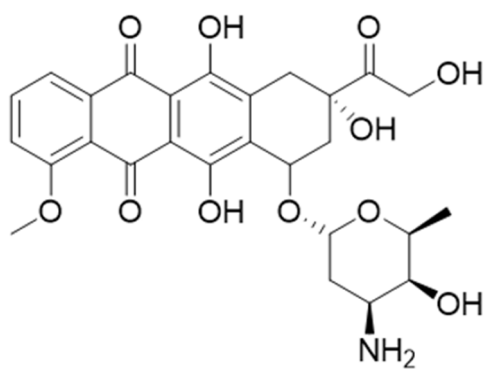
Figure 3-2. Chemical structures of (A) coumarin 6 and (B) DOX

2.2. Animals and ethics

C57BL/6 mice (male, 7-8 weeks) were supplied by Koatech Inc. (Pyeongtaek, Republic of Korea). All animals were housed at 24°C with a 12/12-h light/dark cycle. The Institutional Animal Care and Use Committee (IACUC) of Seoul National University (reg. no. SNU-200326-9) approved all animal studies.

2.3. Synthesis of encapsulated lignin nanoparticle

2.3.1. Coumarin 6-encapsulated nanoparticle

Synthesis of coumarin 6-encapsulated lignin nanoparticles (CELNP) was conducted using the nanoprecipitation method. KL and KL-F1 were dissolved in 10 mL of THF at three different concentrations (1, 2, and 4 mg mL^{-1}), and the solutions were then filtered with a 0.50 μm syringe filter. Coumarin 6 was dissolved in the lignin-THF solution at a fixed concentration of 0.2 mg mL^{-1}. The solution was poured into a pre-soaked dialysis tube and was immersed in 2 L of deionized water (replaced at intervals of 3 h) for over 12 h while stirring at 300 rpm. Products (CELNP and CELNP-F1) at concentrations of 1, 2, and 4 mg mL^{-1} were denoted CELNP-C1, CELNP-C2, CELNP-C4, CELNP-F1-C1, CELNP-F1-C2, and CELNP-F1-C4, respectively. Each experimental variable was run in triplicate.

2.3.2. DOX-encapsulated nanoparticle

Based on the results of coumarin 6-encapsulated nanoparticle in Section 3.1.2., KL was selected as a polymer to synthesize DOX-encapsulated nanoparticles (DELNP). KL was dissolved in 9 mL of THF at three different concentrations (1, 2, and 4 mg mL^{-1}), and the solutions were then filtered with a 0.50 μm syringe filter. 2 mg of DOX in 1 mL of DMSO was added to the lignin-THF solution to set the total solution 10 mL (0.2 mg mL^{-1} DOX). The nanoprecipitation process was followed with the immersion of the THF solution in a dialysis tube in deionized water for 12 h with stirring at 300 rpm. Product nanoparticles were labeled as DELNP-C1, DELNP-C2, DELNP-C4, respectively. Each variable was also run in triplicate.

2.4. Characterization of encapsulated nanoparticle

2.4.1. Determination of physical properties of nanoparticle

The particle size distribution, mean particle diameter, and electrokinetic potential in colloidal dispersion were calculated using a Zetasizer Nano ZS instrument (Malvern Panalytical Ltd., Worcestershire, UK). The samples were diluted and measured at a constant temperature of 25 °C. Peak size (mean size and width for each separate peak of the distribution) and Z-average size (harmonic intensity averaged size) were presented. The surface charges were measured and converted into zeta potential values by Smoluchowski's formula. Each value was obtained by averaging measurements of three samples.

2.4.2. Drug loading

Drug encapsulation efficiency (EE) of CELNPs was measured by an ultraviolet-visible light detector (UV-Vis, Evolution™ 201 UV-Visible spectrophotometer, Thermo Fisher Scientific, Waltham, MA, USA). Ethanol was introduced to the CELNP suspension in water for over 10 h under stirring to dissolve the uncovered coumarin 6 and sediment the CELNPs. The mixture was centrifuged at 12,000 rpm for 10 min. Coumarin 6 amount in the supernatant was measured using a calibration curve plotting the UV absorbance at 460 nm as a function of the concentration. The correlation coefficient (R^2) obtained for the calibration curve was 0.98, indicating good linearity. The EE and drug loading degree (LD) were calculated according to the following equations:

$$Encapsulation\ efficiency\ (\%) = W_t/W_i \times 100 \qquad (1)$$
$$Drug\ loading\ degree\ (\%) = W_t/(W_i + W_{np}) \times 100 \qquad (2)$$

where W_i is the total amount of ingredient added initially, W_t is the total amount of encapsulated ingredients in the nanoparticles, and W_{np} is the total amount of nanoparticles.

In the case of DELNPs, the suspension was centrifuged at 12,000 rpm for 10 min. This procedure was repeated twice again. The absorbance of the supernatant was measured at 500 nm with a UV-Vis to detect the DOX amount inside. The correlation coefficient obtained for the calibration curve was 0.99. The EE and LD were also calculated using Eq. (1) and (2).

2.4.3. *In vitro* release study

In vitro release profiles of CELNPs and DELNPs were evaluated by performance in sink conditions in phosphate-buffered saline (PBS) pH 5.5 and 7.4 buffer. For that, 120 μg of pure ingredient and 200 μg of CELNPs or DELNPs were immersed in 200 mL and 20 mL of PBS, respectively. The samples were stirred at 150 rpm and 37 °C. At the scheduled time intervals (10, 20, 40, 60, 120, 180, 240, 1,440, and 2,880 min), five-milliliter aliquots were taken out and replaced by the same volume pre-heated PBS to keep the volume of the release medium constant. The samples were centrifuged at 12,000 rpm for 10 min to observe the drug release by UV-Vis at 460 nm (coumarin 6), 480 nm (DOX·HCl), or 500 nm (DOX). Drug release kinetics of ingredients were analyzed by Korsmeyer–Peppas model using the first > 60% drug release data (Bezuidenhout et al., 2015; Korsmeyer & Peppas, 1983). The model describes some release mechanisms simultaneously by the following equation:

$$M_t/M = Kt^n \tag{3}$$

where M_t/M is the fraction of drug release at the time, K is the Korsmeyer–Peppas constant, t is the time (hour), and n is the release exponent.

2.5. Biocompatibility tests

2.5.1. CCK-8 assay

The cytotoxicity of DOX and DELNPs (C1, C2, and C4) on A549 cells (ATCC®, CCL-185™, Manassas, VA, USA) and Lewis Lung Carcinoma cells (LLC, ATCC®, CRL-1642™) was ascertained by Cell Counting Kit-8 (CCK-8) assays. The cells were first grown in Dulbecco's Modified Eagle Medium (DMEM, Thermo Fisher Scientific, Waltham, MA, USA) containing 10% fetal bovine serum (FBS, Atlas Biologicals, Fort Collins, CO, USA) and 1% Antibiotic-Antimycotic solution (GeneDireX, Las Vegas City, NV, USA) followed by seeding and attaching onto 96-well plates (3×10^3 cells per well) overnight. After the medium was removed, serum-free DMEM containing 1% Antibiotic-Antimycotic and DOX (25, 50, 100, and 250 $\mu g\ mL^{-1}$) or DELNPs with various concentrations (25, 50, 100, and 250 $\mu g\ mL^{-1}$ DOX Equiv. $\mu g\ mL^{-1}$ based on the EE) were added. The cell lines were cultured at various time intervals (24, 48, and 72 h for A549 and 8, 16, and 24 h for LLC). To examine cell viability, 10 μL of CCK-8 (Dojindo Molecular Technologies Inc., Kumamoto, Japan) was added into each well and incubated for 3 h at 37 °C. The absorbance of the media at 450 nm was measured using a microplate reader (Sunrise™, TECAN Group Ltd., Männedorf, Switzerland). Cells incubated with DMEM supplemented with 10% FBS and 10% Triton X-100 (TX, LPS solution, Daejeon, Republic of Korea) were used as positive and negative controls, respectively. Three replicates were used for each assay. All results were reported as the mean ± standard deviation ($n = 3$).

2.5.2. Hemolysis assay

The blood samples (0.6 mL) were collected from rats by tail-vein or retro-orbital blood collection. Subsequently, an anticoagulant (BD Vacutainer® K₂EDTA 5.4 mg, BD Life Sciences, Franklin Lakes, NJ, USA) was added. The blood sample was used within 0.5 h. After centrifugation at 2,140 rpm and room temperature for 2 min, the red blood cells (RBCs) were washed until the supernatant was clear and diluted by PBS to obtain a 5×10^8 cell mL^{-1} suspension. 250 µg mL^{-1} of DOX or various concentrations of the DELNP samples (10, 100, and 250 µg mL^{-1} DOX Equiv. µg mL^{-1}) were mixed with 1 mL of RBC suspension and incubated for 1 h at 37 °C. The negative and positive controls were pure PBS and 1% TX in PBS, respectively. After centrifugation at 3,090 rpm and room temperature for 2 min, the hemoglobin releases were detected at 540 nm using a SpectraMax® iD3 multi-mode microplate readers (Molecular Devices, San Jose, CA, USA). The hemolytic degree was expressed by the hemoglobin release as the following Eq. (4):

$$Hemoglobin\ release\ (\%) = (OD_{sample} - OD_{negative})/(OD_{positive} - OD_{negative}) \times 100 \quad (4)$$

where OD is a calculated optical density value.

2.5.3. *In vivo* detection of an allergic reaction

42 male C57BL/6 mice (8~9 weeks) were housed in individually ventilated cages under a 12h light/dark cycle at a temperature of 24~26 °C and humidity of 30~50% and with *ad libitum* access to food and water. Mice (n=6 per group) were anesthetized with 2% of isoflurane and then intravenously injected with DOX (10 mg kg^{-1}), and DELNP (10 mg DOX Equiv. mg kg^{-1}), and KLNP, whose net gram amount was the same as those used for preparing DELNP, via retro-orbital plexus every other day for five times. Two days after the final administration, mice were sacrificed via CO_2 inhalation. Their blood was collected from the heart, followed by being incubated in a serum-separating tube (BD Life Sciences, Franklin Lakes, NJ, USA) for 20 minutes at room temperature. The serum samples were then obtained by centrifugation at 3,000 G for 20 min at room temperature. Total IgE serum levels were measured using an ELISA kit (cat. no. 88-50460-22, Thermo Fisher Scientific, Waltham, MA, USA) according to the manufacturer's instructions. Briefly, 96-well plates were coated overnight at 4 °C with 100 µL capture antibody per well (provided by the kit). Following two washes with wash buffer, plates were blocked with 250 µL of blocking buffer at room temperature for 2 h. Plates were washed twice with wash buffer, and 100 µL serum sample (1:50) was added to each well. Plates were further incubated at room temperature for 2 h. Next, 100 µL of biotinylated detection antibody per well was added and incubated at room temperature for 1 h. Following four-time washes, 100 µL of streptavidin-horseradish peroxidase per well was added and incubated at room temperature for 30 min. Wells were further washed 4 times, 100 µL of substrate solution was added per well, and samples were incubated for 30 min at room temperature. Finally, a stop solution was added, and OD values were measured at 450 nm.

2.6. *In vivo* anticancer efficacy

C57BL/6 mice were anesthetized with 2% isoflurane and subcutaneously engrafted with one million LLC cells in the left flank. On day 4, mice were randomly allocated (N = 6) and intravenously injected every other day for a total of five times with PBS, DOX (3.0 mg kg^{-1}), DELNP (3.0 mg kg^{-1} DOX Equiv. mg kg^{-1}), or neat KLNP whose net gram amount was same as those used for preparing DELNP. After 28 days of final administration, mice were euthanized with CO_2 inhalation. In the case where tumor volume reached more than 2,000 mm^3, animals were humanely sacrificed as described above. The tumor volume was measured every three or four days and calculated as (width)^2 × (length) × 0.5.

2.7. Statistical analysis

Statistical differences among groups were analyzed by analysis of variance (ANOVA), and multiple t-tests were performed to compare differences between the two groups. A p-value of <0.05 was considered significant.

3. Results and discussion

3.1. Particle size and encapsulation efficiency

3.1.1. Coumarin 6-encapsulated nanoparticle

Particle size and distribution are the key parameters that affect drug release, stability, safety, and efficacy. Here, the influences of lignin concentration and types of ingredients on the particle size, distribution, and drug uptake have been studied. First, this study aimed to set the appropriate experimental conditions for the synthesis of ELNPs by using a drug model compound, coumarin 6, before using DOX.

The lignin concentration influenced the average particle size and distribution of CELNPs, but the relationship between them was not significant (Table 3-2). The smallest peak size of 176 nm was obtained at 2 mg mL^{-1} lignin concentration. Also, CELNP-C2 had a single peak with the narrowest peak width, which indicates a finer particle size distribution (Figure 3-3). CELNP-C4 exhibited a relatively bigger single peak size of 374 nm. However, CELNP-C1 had two different peaks - one is a large peak of small particles (256 nm), and the other is a small but broad peak that might be from particle clusters (Caputo et al., 2019). Compared to the pure lignin nanoparticles (KLNP-Cs) mentioned in the previous chapter, interestingly, the peak sizes did not significantly change without regard to coumarin 6 added. It is assumed that the growth by condensation ends at a similar period regardless of the addition of a small number of ingredients since overall pre-dialysis lignin concentration did not change (Martinez Rivas et al., 2017).

CELNPs synthesized from KL-F1 lignin fraction with the lower M_w, M_w/M_n, and higher phenolic hydroxyl group content showed significantly bigger sizes than the neat lignin group. This result agrees with the results from the previous chapter.

The trend in the particle size and distribution, however, is similar between CELNPs and CELNP-F1s. The smallest peak size and the narrowest peak width were obtained at 2 mg mL^{-1} lignin concentration. While the particles obtained at 1 or 4 mg mL^{-1} lignin concentration exhibited larger and broad-distributed sizes.

The EE and LD of each CELNP are presented in Figure 3-4. The EE and LD in the CELNP-C1, C2, and C4 were 59 ± 5, 54 ± 10, and $39 \pm 3\%$, and 11 ± 1, 5 ± 1, and $2 \pm 0\%$, respectively. On the other hand, The EE and LD in the CELNP-F1-C1, C2, and C4 were 28 ± 5, 37 ± 7, $20 \pm 12\%$, and 5 ± 1, 4 ± 1, $1 \pm 1\%$, respectively. Compared to the EE of lignin-based nanoparticle from the studies using benzazulene, sorafenib (Figueiredo et al., 2017), and resveratrol (Dai et al., 2017) (77 ± 10, 68 ± 19, and max. 95.2% respectively), EE in the CELNP, especially in the CELNP-C4 and CELNP-F1-Cs, is relatively low. It is suspected that the EE of nanoparticles shows a decreasing trend with the increasing encapsulated lignin particle size ($R^2 = 0.76$).

Table 3-2. Size properties of coumarin 6-encapsulated lignin nanoparticles (CELNPs)

	Peak size (nm)				Z-average size (nm)	PDI
	Peak 1	Intensity (%)	Peak 2	Intensity (%)		
CELNP-C1	256	94.0	3,811	6.0	193.8	0.261
CELNP-C2	176	100	-	-	328.9	0.349
CELNP-C4	374	100	-	-	367.4	0.260
CELNP-F1-C1	1,123	100	-	-	915.9	0.175
CELNP-F1-C2	916	100	-	-	1,465	0.490
CELNP-F1-C4	1,133	94.0	5,403	6.0	1,520	0.388
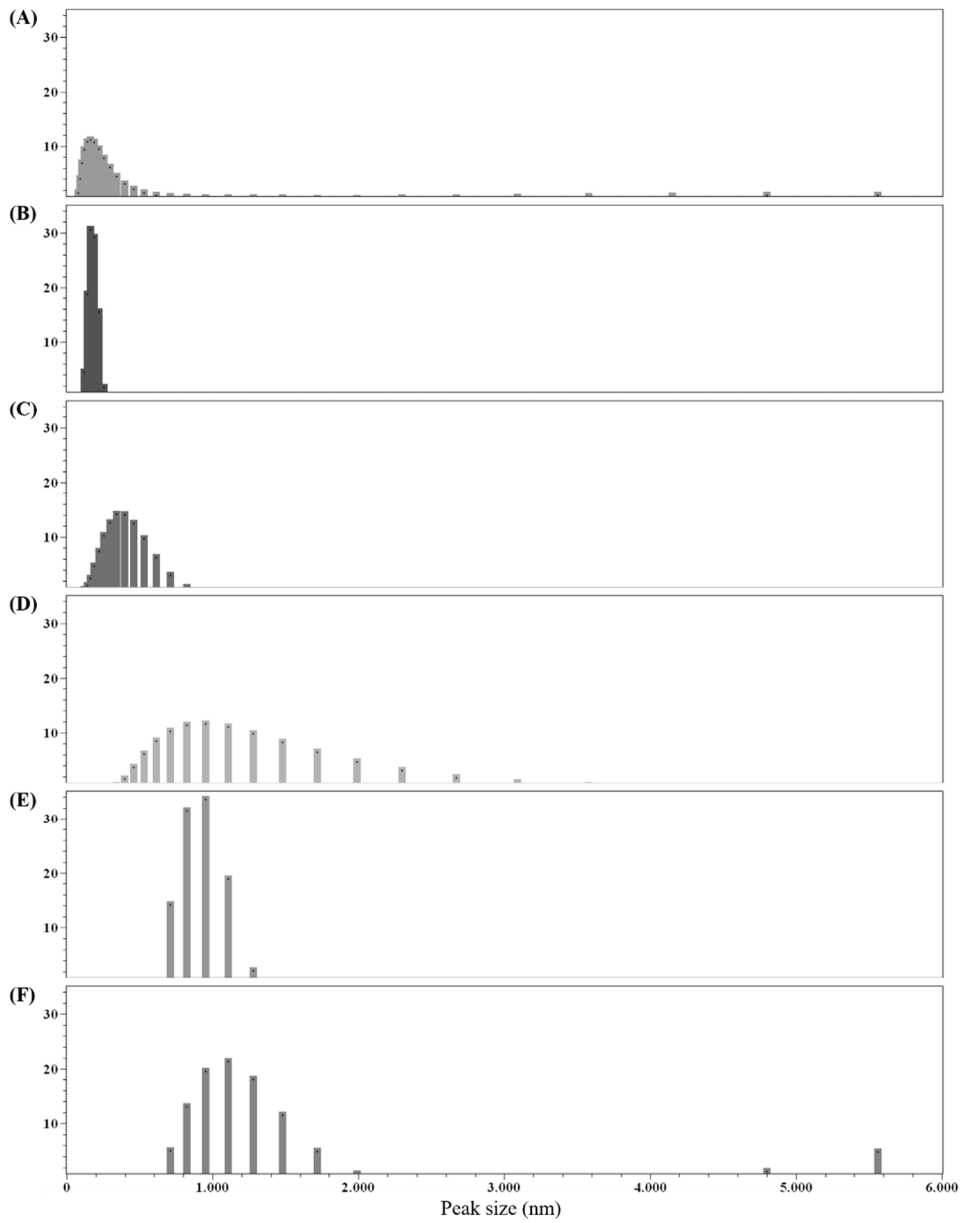
Figure 3-3. Peak size graph of different CELNPs with pre-dialysis concentrations. (A) CELNP-C1, (B) CELNP-C2, (C) CELNP-C4, (D) CELNP-F1-C1, (E) CELNP-F1-C2, and (F) CELNP-F1-C4.
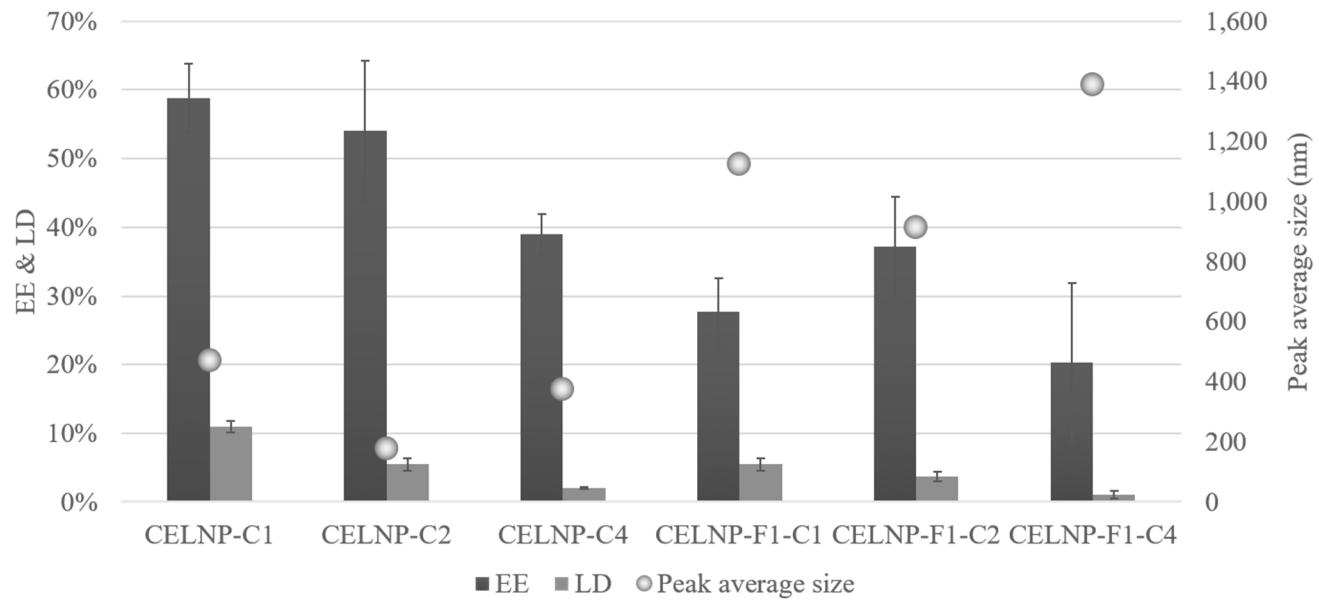
Figure 3-4. Drug encapsulation properties of CELNPs as a function of pre-dialysis concentration

3.1.2. DOX-encapsulated nanoparticle

In the previous section, poor drug-entrapment properties of ethyl acetate fraction-derived nanoparticles (CELNP-F1s) were examined. Therefore, only neat KL as a polymer was chosen to form DOX-encapsulated particles.

Before encapsulation by lignin, nanoprecipitation of free DOX has carried out. 2 mg of DOX in 10 mL of DMSO was immersed in a dialysis tube in deionized water for 12 h with stirring at 300 rpm. Nanoprecipitated DOX particles exhibited a size of 2,868 nm (Table 3-3). Note that the free DOX particle in deionized water, however, was completely sedimented within 48 h because of its water-insolubility and low colloidal stability.

The smallest peak size of 327 nm was obtained at 1 mg mL^{-1} lignin concentration. Although the peak 1 size was 146 nm, there was another long and broad tail peak (1,141 nm) in DELNP-C1. Differently, DELNP-C2 and C4 had a small peak derived from condensed particles. Compared to the pure lignin nanoparticles (KLNP-Cs), the peak sizes of DELNPs did not significantly change even DOX was added, but the size distribution showed a weak bimodal pattern. The average particle size of DELNPs suggests that they can not only release drugs but also directly go through fenestrated tumor vascular endothelium (200~780 nm) or lung (1~400 nm) (Gaumet et al., 2008).

The EE and LD of each DELNP are presented in Figure 3-6. The EE and LD in the DELNP-C1, C2, and C4 were 64 ± 13, 73 ± 7, and 69 ± 11%, and 12 ± 2, 7 ± 1, and 4 ± 0%, respectively. Despite the larger DOX size (543.52 g mol^{-1}) than coumarin 6 (350.40 g mol^{-1}), DELNP has a higher drug-entrapping ability than CELNP. Since DOX has a similar polyphenolic structure and phenolic hydroxyl group to lignin, both hydrogen bonding and the π–π stacking interaction could positively affect DOX encapsulation by ELNP. In contrast to CELNPs, there was no remarkable correlation between DELNP particle size and encapsulated DOX amount.

Table 3-3. Size properties of DOX and DOX-encapsulated lignin nanoparticles (DELNPs)

	Peak size (nm)				Z-average size (nm)	PDI
	Peak 1	Intensity (%)	Peak 2	Intensity (%)		
DOX	2,868	100	-	-	3,025	0.197
DELNP-C1	146	79.0	1,141	18.6	155.3	0.335
DELNP-C2	315	97.3	4,681	2.7	234.5	0.339
DELNP-C4	258	96.3	4,989	3.7	256.7	0.219
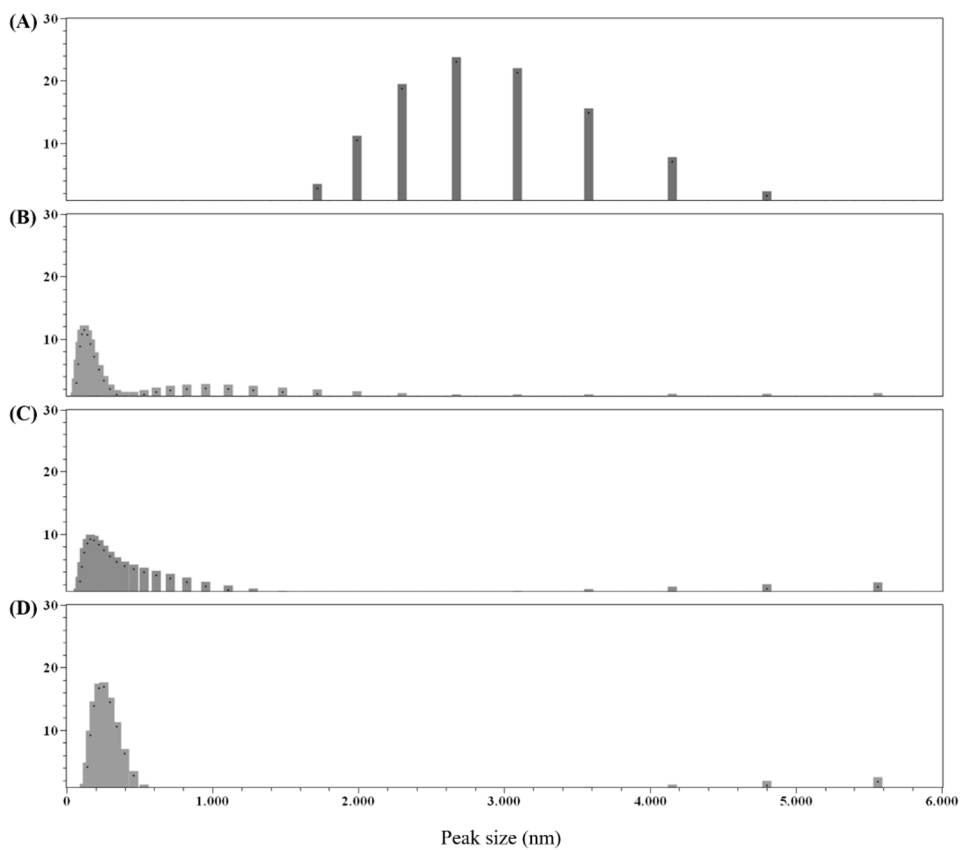
Figure 3-5. Peak size graph of DOX and different DELNPs with pre-dialysis concentrations. (A) DOX, (B) DELNP-C1, (C) DELNP-C2, and (D) DELNP-C4.
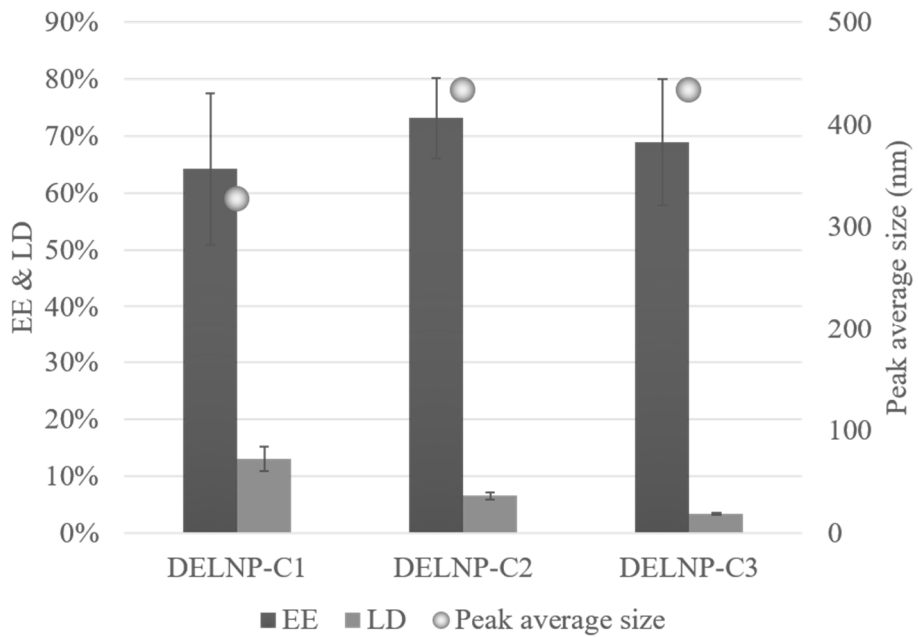
Figure 3-6. Drug encapsulation properties of DELNPs as a function of pre-dialysis concentration

3.2. Particle surface charge

Zeta potential, an electrical potential at the shear plane, of ELNPs were determined in this study. If two adjacent particles in colloid have zeta potentials less than -30 mV, we generally predict they will not agglomerate due to enough repulsive electrostatic forces between them (Sapsford et al., 2011).

Zeta potential values for both CELNPs and DELNPs exceeded -30 mV, indicating relatively high stability in water. Only CELNP-Cs showed a weak decreasing trend of zeta potential with increasing pre-dialysis lignin concentration. No significant trends of changing zeta potential with respect to pre-dialysis conditions in other particle groups were observed. Compared with the zeta potential of non-encapsulated KL nanoparticles (KLNP-Cs, Table 2-7), a slight decrease in the CELNP group was found. On the contrary, there was no remarkable change in the zeta potential of DELNPs compared to KLNPs. These trends are strong evidence of successful drug encapsulation by lignin since if the drug molecules are adsorbed on the surface of the lignin particle, then its colloidal stability changes (Wang et al., 2013).
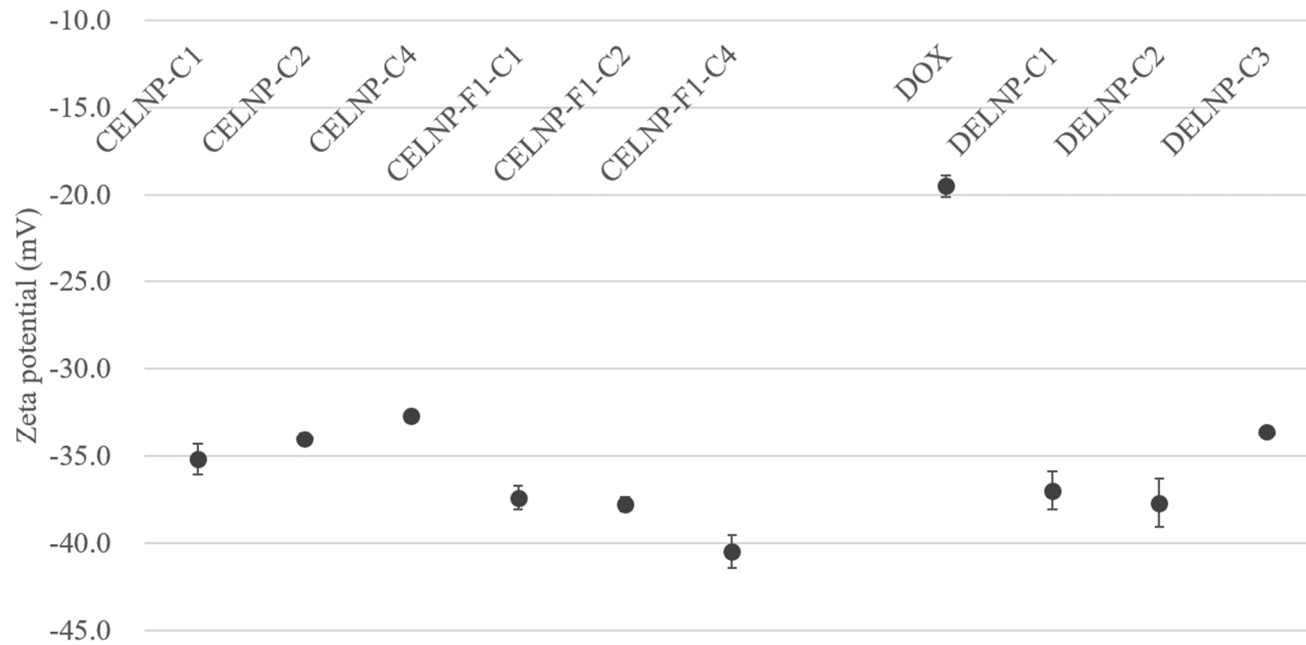
Figure 3-7. Zeta potential values of DOX, CELNPs, and DELNPs as functions of various conditions

3.3. *In vitro* drug release

The drug release of CELNPs and DELNPs was evaluated in two different PBS conditions to simulate the tumor microenvironment or intracellular endosomes (pH 5.5) and the normal blood (pH 7.4). For coumarin 6 in the pH 5.5 buffer, over 80% of the total encapsulated ingredient amount was released within the initial stage (0~4 h), and a release was almost finished afterward (Figure 3-8A). On the other hand, less than 50% of total encapsulated coumarin 6 was released within the initial stage at pH 7.4 and a slow-release till 48 h (Figure 3-8B). A much higher release rate of coumarin 6 at a lower pH than pH 7.4 was reported in another research (Chen et al., 2016). The rapid release rate of CELNP under acidic conditions may be explained by the protonation of coumarin 6 in low pH (Mina et al., 2013) since protonated molecules could weaken the bonding of capsules.

For DOX in the buffers, the rapid release of DELNPs within the initial stage, followed by a slow-release at pH 5.5 and comparatively slower release at pH 7.4, was also determined (Figure 3-9). Compared with the release rate of CELNPs, the releasing trend of DELNPs was similar, but the final release amount of DOX was lower than coumarin 6. It may be explained that the relatively lower protonation ability of DOX (1 site mol^{-1} compared with 2 sites mol^{-1} for coumarin 6) and higher interaction strength between lignin and DOX caused by the hydrogen bonding and/or π–π stacking. It is suggested that the rapid release of ELNP is suitable for hydrophobic drugs, which need a quick sustained release and declined side effects.

Korsmeyer–Peppas model, one of the non-linear regression models used in the drug-releasing porous polymer matrix, was used to determine the release kinetics of each ELNPs (Table 3-4). Both drug release profiles of CELNPs and DELNPs fit the model well since the release rate was higher in the initial stage. Since almost all the release profiles of ELNPs represented release exponent value lower than 0.5, it can be suggested that the ELNPs follow the Fickian diffusion rather than the non-Fickian one (both diffusion and swelling) (Bezuidenhout et al.,

2015). There are huge differences in Korsmeyer-Peppas constant (time-dependent) between DELNP and CELNP or pH 5.5 and 7.4. Therefore, it could be assumed that the drug molecule types and pH conditions affect the drug diffusion rate of the nanoparticle.
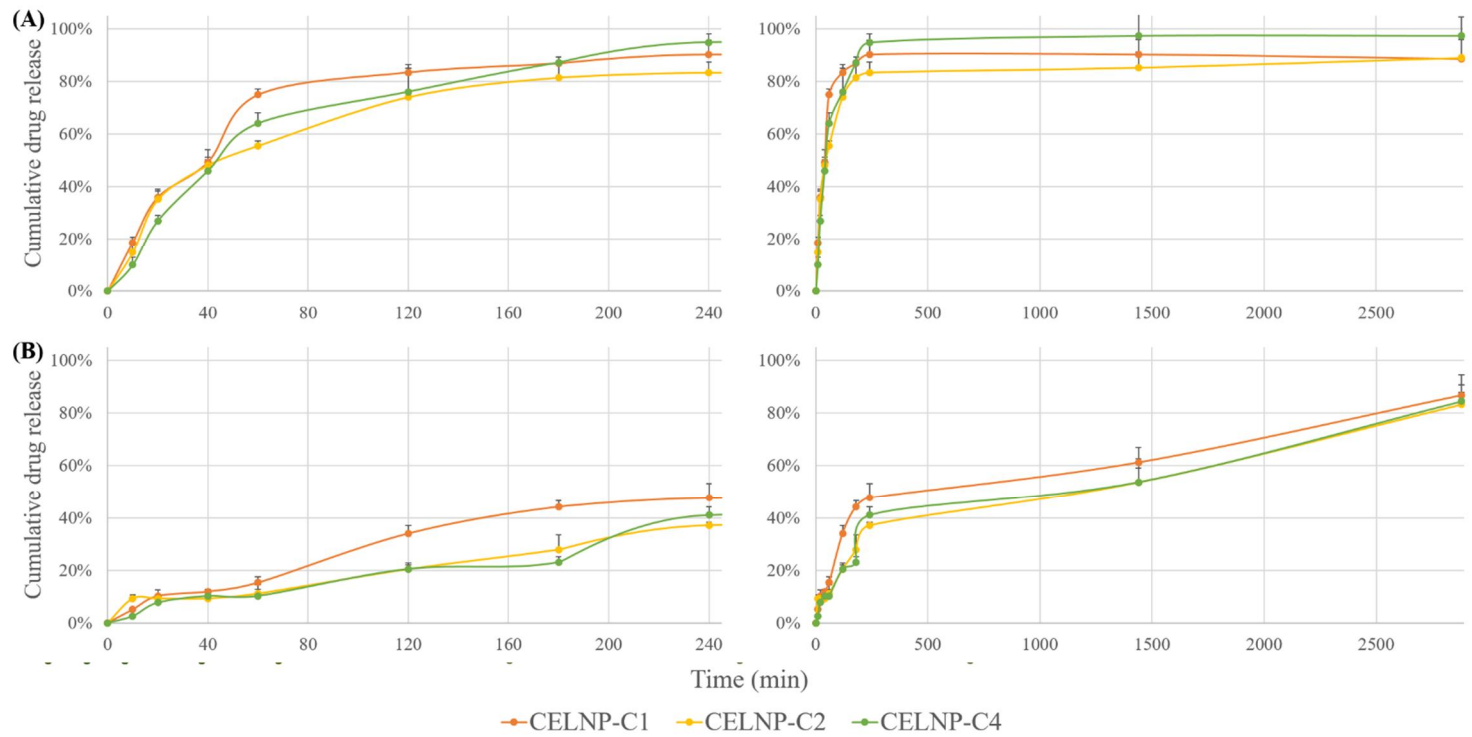
Figure 3-8. Coumarin 6 release kinetics of CELNPs in PBS at (A) pH 5.5 and (B) pH 7.4 conditions
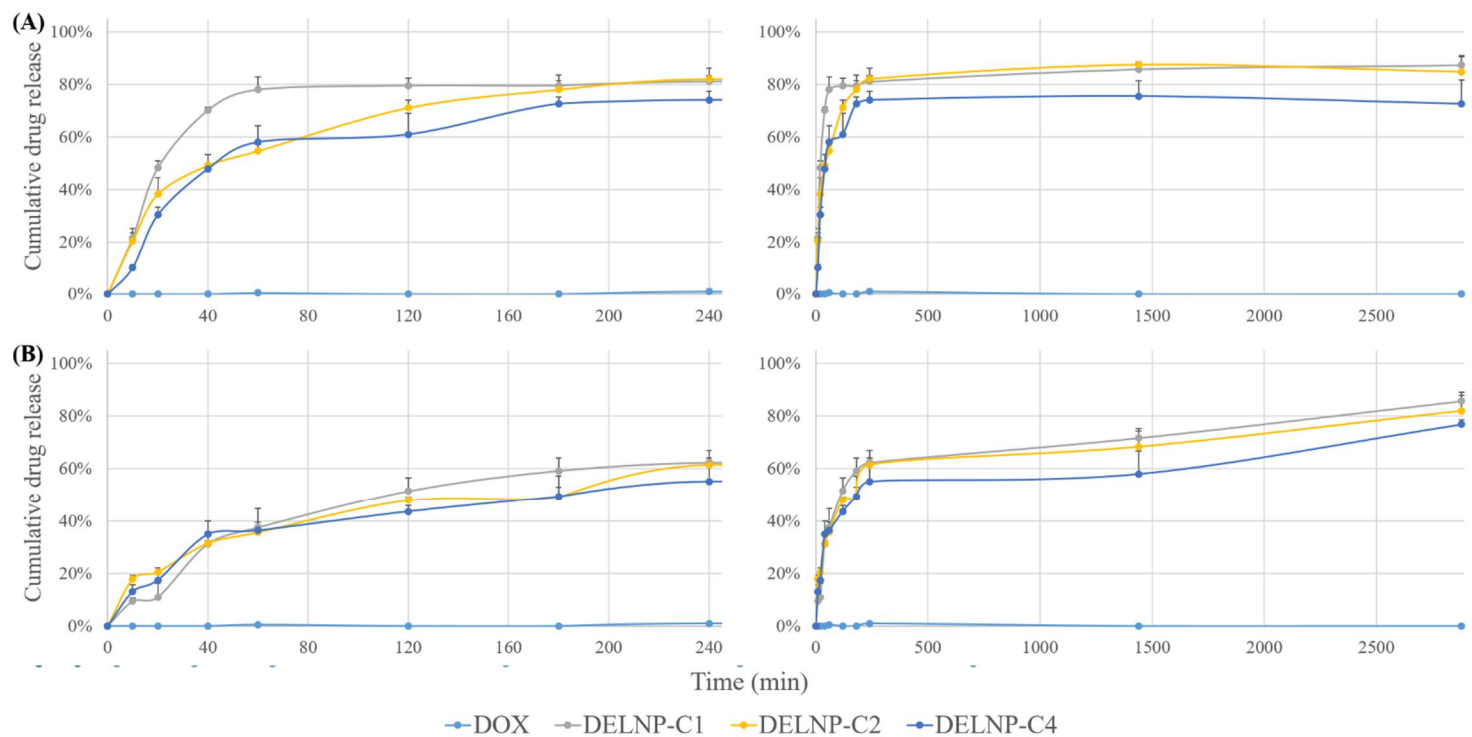
Figure 3-9. DOX release kinetics of DELNPs in PBS at (A) pH 5.5 and (B) pH 7.4 conditions

Table 3-4. R-square and equation values of fitting curves of Korsmeyer–Peppas model for drug release

Samples		Korsmeyer-Peppas constant	Release exponent	Coefficient of determination (R^2)
pH 5.5	CELNP-C1	0.33	0.14	0.979
	CELNP-C2	0.28	0.16	0.917
	CELNP-C4	0.26	0.18	0.975
pH 7.4	CELNP-C1	0.05	0.34	0.893
	CELNP-C2	0.03	0.42	0.930
	CELNP-C4	0.02	0.44	0.927
pH 5.5	DELNP-C1	0.40	0.11	0.958
	DELNP-C2	0.29	0.15	0.938
	DELNP-C4	0.27	0.15	0.841
pH 7.4	DELNP-C1	0.04	0.51	0.929
	DELNP-C2	0.07	0.39	0.981
	DELNP-C4	0.14	0.20	0.828

3.4. *In vitro* cytotoxicity

Although an examination of cell viability is generally used to measure the cytotoxicity of polymeric nanoparticle itself, it is fitted more to the drug-encapsulation effect of nanoparticles in the case of DELNPs, since the drugs can exhibit much higher cytotoxicity than lignin. The high biocompatibility of lignin-based nanoparticles was already revealed in the previous chapter. Herein, the difference of cytotoxicity (or chemotherapeutic effect) as a function of time between free DOX and DELNPs in A549 and LLC cell lines was evaluated by the CCK-8 assay.

Fatal and rapid cytotoxic activity of free DOX was determined in both A549 and LLC cell lines. Specifically, A549 cell death at all the concentrations was remarkable within 24 h after treatment (Figure 3-10A). Also, DOX exhibited very high cytotoxicity to LLC cell lines at all the concentrations except 25 μg mL^{-1} within 8 h (Figure 3-11A). However, DELNPs steadily decreased the number of cells. All DELNPs showed a negligible antiproliferation effect to A549 until 24 h and significant cytotoxicity after 48 h (Figure 3-10B–D). In the LLC cell line, DELNPs showed no cytotoxic activity until 8 h, although the effect was significant within 16 h. As a result, it was revealed that the drug-encapsulation and diffusion-based controlled release of DELNP slowed down, but not decreased, the cytotoxic effect of DOX.
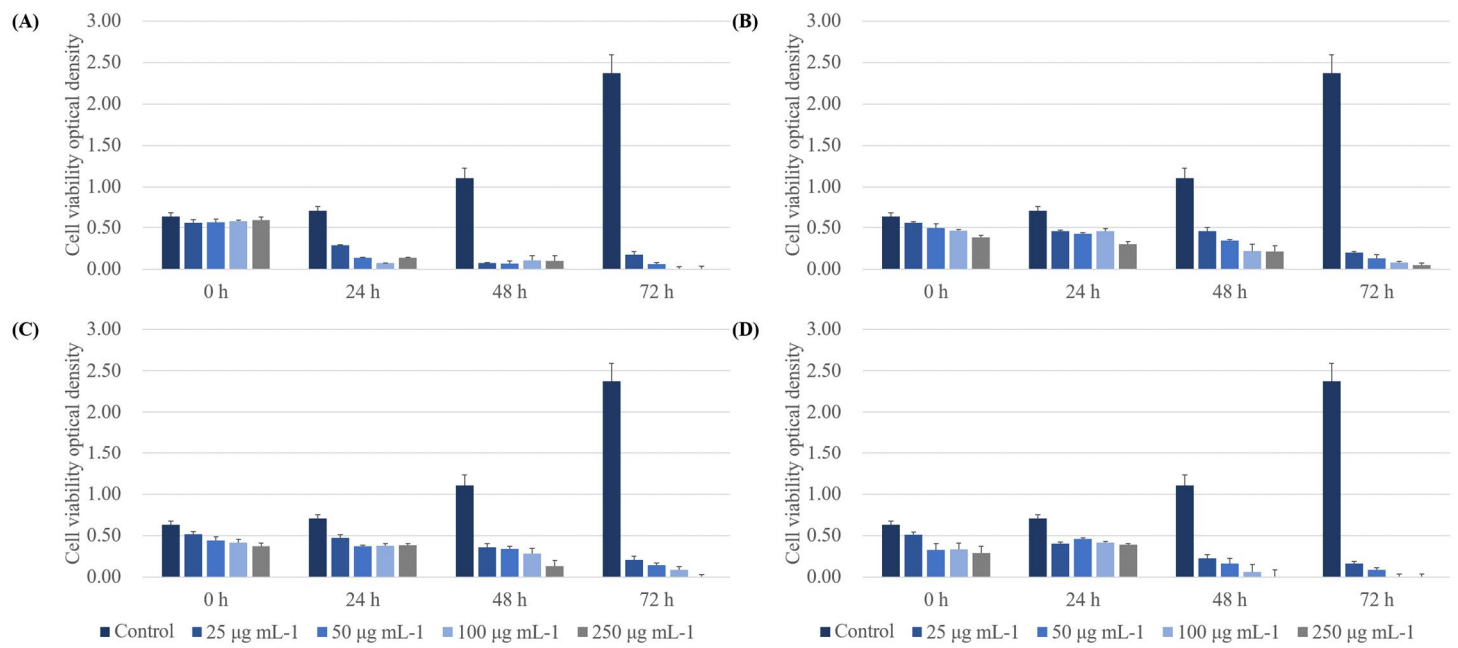
Figure 3-10. Cytotoxic effect of DELNPs on A549 cells. (A) DOX, (B) DELNP-C1, (C) DELNP-C2, and (D) DELNP-C4. The viability was determined by the Cell Counting Kit-8 assay, and all data sets were compared to the blank control (serum-free DMEM containing 1% of Antibiotic-Antimycotic). The data are presented as the mean ± standard deviation of three independent experiments.
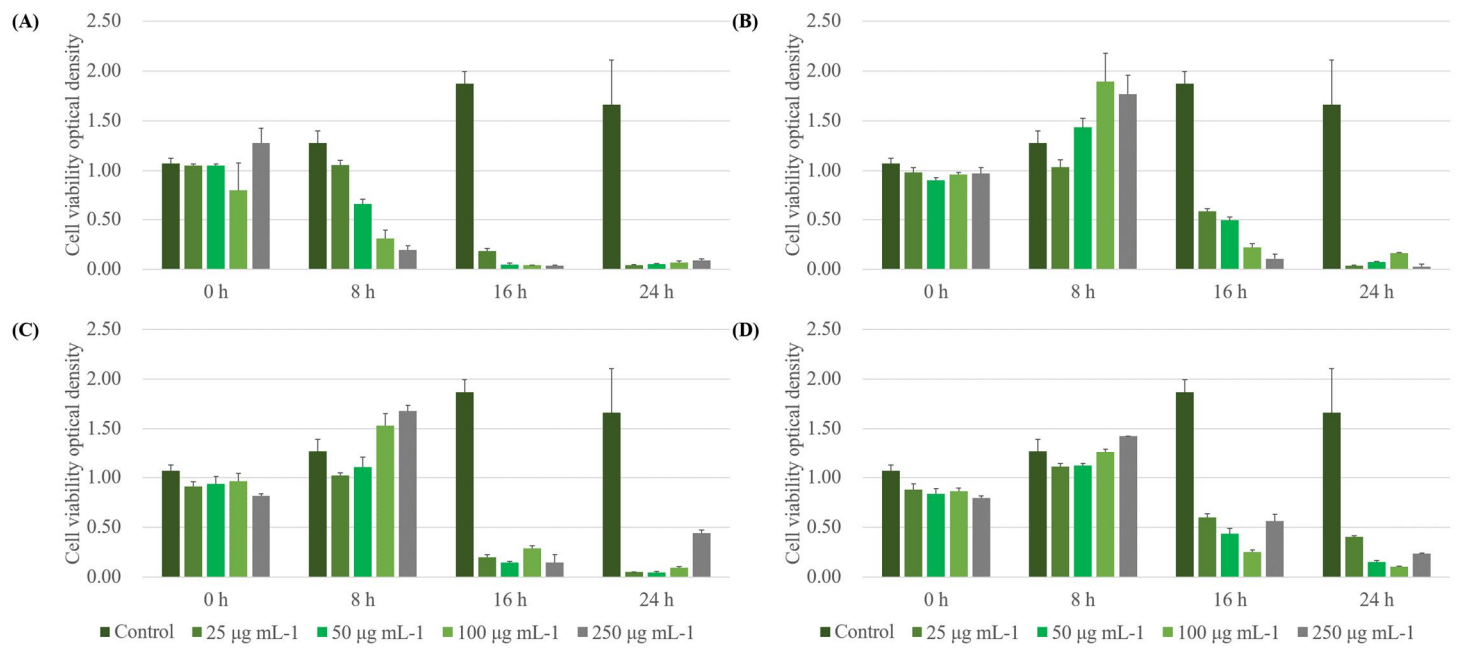
Figure 3-11. Cytotoxic effect of DELNPs on LLC cells. (A) DOX, (B) DELNP-C1, (C) DELNP-C2, and (D) DELNP-C4. The viability was determined by the Cell Counting Kit-8 assay, and all data sets were compared to the blank control (serum-free DMEM containing 1% of Antibiotic-Antimycotic). The data are presented as the mean ± standard deviation of three independent experiments.

3.5. Hemocompatibility

The hemolysis effect of pure DOX or DELNPs was evaluated by hemoglobin release after exposure to DOX or different DOX-equivalent concentrations of DELNPs (Figure 3-12). Although it is reported that drug-induced hemolysis is relatively rare, the potential hemolytic effect should be considered before application. For example, significant deconstruction of human RBC induced by free DOX (around 20%) was reported (Lee et al., 2017).

For the three different DELNPs tested, the hemoglobin releases were less than 2% for concentrations ranging from 10 to 250 µg mL^{-1} DOX Equiv. µg mL^{-1}. In detail, the hemoglobin release induced by DOX was $8.7 \pm 1.7\%$. However, the release results of DELNPs (10, 100, and 250 µg mL^{-1} DOX Equiv. µg mL^{-1}) were found to be 0.18 ± 0.08, 0.22 ± 0.12, and $1.04 \pm 0.05\%$, respectively. Since it is known that an *in vitro* hemolysis below 10% is non-hemolytic (Amin & Dannenfelser, 2006), even DELNP with the highest DOX concentration can be considered safe. In addition, a decrease in DOX hemotoxicity by lignin encapsulation (more than 87%) was detected.
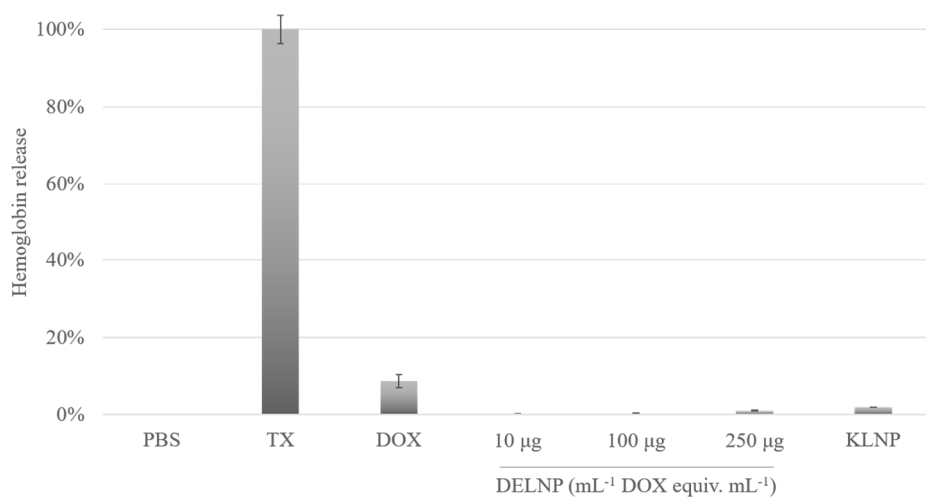
Figure 3-12. Hemoglobin release of DOX, KLNP, and DELNPs with different DOX mass equivalent concentrations

3.6. Hypersensitivity test

Drug-induced allergy or drug hypersensitivity is one of the severe side effects of anticancer. In IgE-mediated reactions, an immune system overreacts to a drug by producing IgE causing the majority of in-hospital anaphylaxis cases (Park et al., 2017). In this study, IgE was selected as the indicator for the evaluation of the hypersensitivity reaction.

The IgE concentrations of PBS (control), DOX, KLNP, and DELNP 7-day after injection were 398 ± 93, 467 ± 118, 622 ± 81, and 538 ± 185 ng mL^{-1}, respectively. The upregulation of the IgE levels of mice due to the excessive amount of DOX was not significant. The levels in the KLNP and DELNP groups were even slightly higher than that of DOX but also tended to be normal. Nevertheless, the IgE level in all the groups exhibited no remarkable change in comparison with the control group. It was confirmed that these nanoformulations have good biocompatibility and could substantially reduce the risk of hypersensitivity.
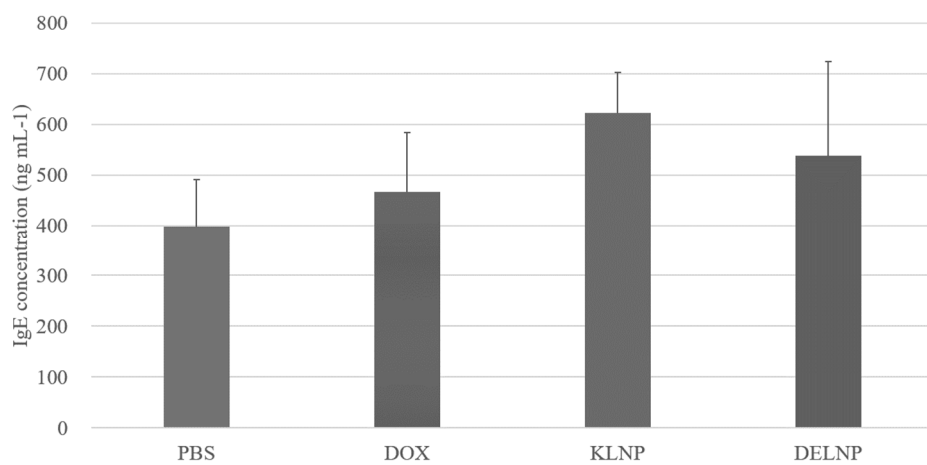
Figure 3-13. Immunoglobulin E (IgE) level induced by DOX, KLNP, and DELNP

3.7. *In vivo* antitumor efficacy

The tumor inhibition effect of DELNP was determined in vivo using LLC-bearing mice. Tumors in each group were carefully grown to reach around the volume of 40 mm^3. The PBS (negative control) and neat KLNP groups had no antitumor effects (Figure 3-14A). In contrast, DELNP (3 mg kg^{-1} Equiv. mg kg^{-1}), DOX extra- (6 mg kg^{-1}), and normal-dose (3 mg kg^{-1}) groups exhibited certain chemotherapeutic effects (Figure 3-15). However, during chemotherapy, weight loss or stalled weight gain in free DOX-treated groups were significant (Figure 3-14B). In addition, after 5-time chemotherapy, all of the DOX extra-dose group died within day 16, and 33% of the DOX normal-dose group died within day 24 (Figure 3-14C). In the case of the DELNP group, tumor inhibition efficacy was found without significant visible side effects. While a sustained-release effect was insignificant compared to the DOX normal-dose group, DELNP displayed an excellent property to reduce toxic and adverse effects of DOX.

(A)

(B)

(C)
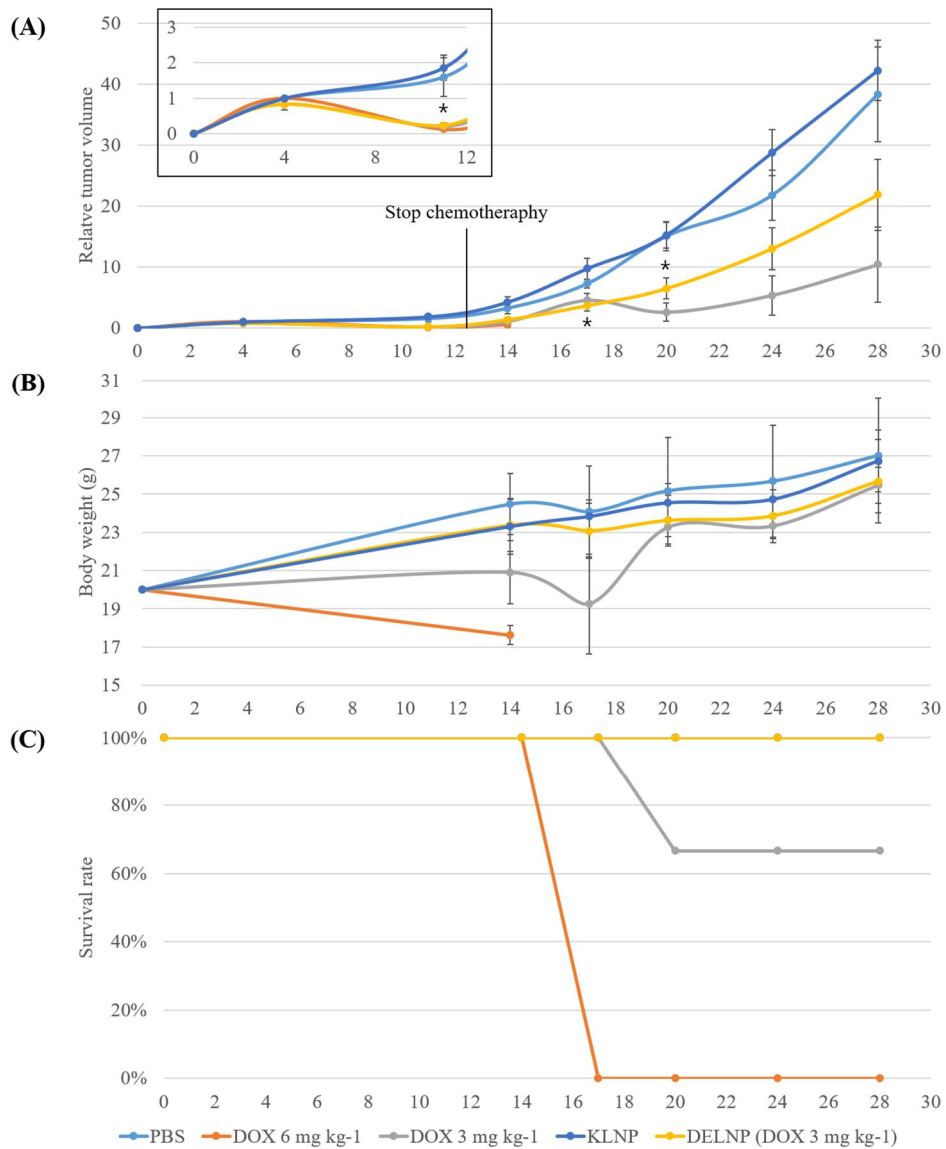
Figure 3-14. Results of DOX-induced tumor inhibition study; (A) Relative tumor volume, the level of the significant differences of DELNP was set at probabilities of *$p < 0.05$, **$p < 0.01$, and ***$p < 0.001$, (B) body weight, and (C) survival rates of tumor-bearing mice with different drug formulations
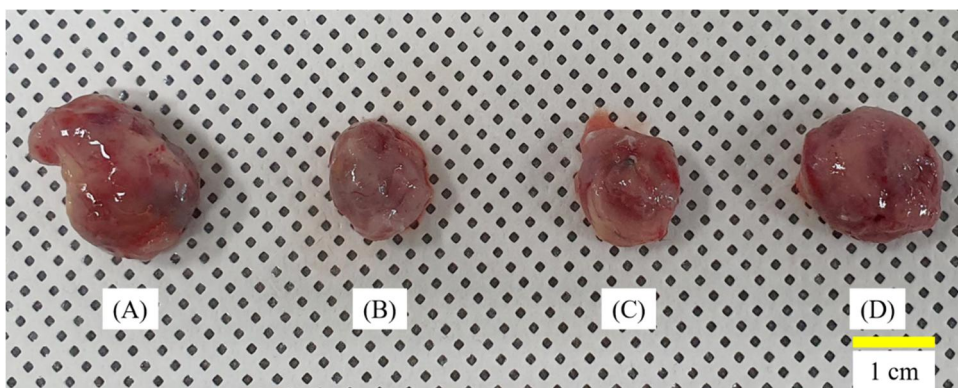
Figure 3-15. Tumor photographs from different groups on day 28. Tumors with (A) PBS (control), (B) DOX 3 mg kg^{-1}, (C) DELNP 3 mg kg^{-1} Equiv. mg kg^{-1}, and (D) KLNP.

4. Conclusion

In this study, a synthesis of a nano-sized drug delivery system was performed using high-quality kraft lignin. Coumarin 6 as a drug model compound and DOX as an anticancer were encapsulated by nanoprecipitation with dissolved lignin. The comprehensive analysis of ELNPs determined that the pre-dialysis lignin concentration weakly influenced the average particle size and distribution of ELNPs. In addition, the addition of drugs did not significantly affect the average particle size of ELNP, but the size distribution became relatively bimodal. The drug encapsulation efficiency of the particle showed a decreasing trend with the increasing particle size. However, the influence of interactions between the drug and lignin were much significant.

Specifically, in the case of DOX, drug-encapsulation by nanoprecipitation improved the size, distribution, and surface charge properties. The average size of DELNPs (327~433 nm) agrees with the requirements for tumor treatments. All the DELNPs exceeded a zeta potential of -30 mV, indicating high stability in water. Besides, there was no remarkable change in the zeta potential of ELNPs compared to neat KLNPs. It suggests the low possibility of drug deposition on the DELNP surface. The diffusion-based controlled drug release profile of ELNPs could be explained by Korsmeyer–Peppas model. The drug release rate was faster in the pH 5.5 (over 70% within the initial stage) than the pH 7.4 (less than 50%). *In vitro* cytotoxicity test also revealed the drug release effect of ELNPs, delaying the cytotoxic activity of DOX in the cancer cells. Both *in vitro* hemotoxicity and *in vivo* allergic reaction tests showed high biocompatibility of DELNPs in the body of living organisms. Due to its relatively quick release, DELNP showed insignificant sustained-release efficacy for *in vivo* tumor inhibition assay compared to free drug. However, drug-encapsulation noticeably decreased the DOX-induced side effects and mortality rates.

As a result, lignin-based ELNPs had important features for biomedical

applications, including very good hemocompatibility, low allergenic properties, high colloidal stability, hydrophobic drug loading efficiency, release profile, and decrease of side effect. This study suggests that the synthesis of ELNPs would be one of the effective methods for the hydrophobic drug delivery system, which also has advantages in environmental and economic sustainability.

Chapter 4

Effect of chemoselective methylation of the phenolic hydroxyl group on lignin nanoparticle synthesis

1. Introduction

Lignin is a natural and three-dimensional phenolic polymer, which accounts for 10~30% of the mass in lignocellulosic biomass. Lignin composed of three kinds of lignin monomer (monolignol, C6C3) including *p*-coumaryl, coniferyl, and sinapyl alcohol with several intermolecular linkages such as β-O-4 (40~60%), β-5 (4~10%), biphenyl (3.5~25%), and α-O-4 (3~5%) (Calvo-Flores et al., 2015; Glasser, 2019). In recent decades, the interest in the utilization of technical lignin as a high-value source has increased since around 70 million tons of lignin byproduct has been generated annually in worldwide pulping/paper industry (kraft, sulfite, etc.) and also in biorefinery (10 million tons per year) (Fang & Smith Jr, 2016; Ragauskas et al., 2014). However, 98% of the extracted lignin solution is just combusted for heat in pulp plants, and only less than 2% of the lignin byproduct is converted into commercial products.

Several research types have been carried out on lignin nanoparticle synthesis in a wide range of industry fields. For example, lignin can be used as a reducing and capping agent to synthesize metallic nanoparticles (Hu & Hsieh, 2016). Also, the synthesis of lignin/sodium dodecyl sulfate composite nanoparticles with high antiphotolysis and antioxidant properties was reported (Pang et al., 2017). In addition, lignin nanoparticle as a material for the novel drug delivery system provides high-value to lignin (Chen et al., 2018; Figueiredo et al., 2017; Kai et al., 2018; Ma et al., 2020; Pang et al., 2020).

In previous studies in chapters 2 and 3, a high potential of LignoBoost kraft lignin as a source of a biocompatible nano-sized drug delivery system was evaluated. Chapter 2, especially, focused on the effect of the lignin structure on the size of the nanoparticles. Six lignin fractions with significant differences in molecular size, weight, number of functional groups and internal linkages, and polydispersity were applied in the nanoprecipitation process. And the correlations between particle sizes and several features of the lignin was examined. However,

it was hard to clarify their correlation because of not only the considerable structural difference between each fraction but also the high size polydispersity of each nanoparticle. Therefore, it was concluded that an additional modification of specific lignin structure is required.

The objective of this study was to examine and discuss the effect of hydroxyl group amount in lignin on the controlling physical properties of lignin nanoparticle, especially on the particle size. The role of the phenolic hydroxyl group on the physicochemical properties of nanoparticle was investigated using functionalized lignin with different amounts of phenolic hydroxyl group content, based on the results from chapter 2. First, an alkaline/soda lignin (AL) from soda pulping was fractionated by sequential solvent extraction to obtain six different fractions with structural differences. At the same time, the phenolic hydroxyl group in AL was selectively blocked by methylation to eliminate the phenolic hydroxyl group's effect in the lignin nanoprecipitation process, which is suspected of controlling the lignin nanoparticle growth by condensation (Figure 2-11). The formation of the AL-based nanoparticle was carried out by the nanoprecipitation method. The physicochemical properties (particle size, distribution, polydispersity, zeta potential, and colloidal stability) of the particles were determined using dynamic light scattering (DLS) and transmission electron microscopy (TEM). The difference of nanoparticle properties between phenolic hydroxyl group-blocked AL by methylation was carefully determined. The possible cytotoxicity was also assessed by the Cell Counting Kit-8 (CCK-8) test.

2. Materials and methods

2.1. Materials

Alkaline/soda lignin (AL) extracted from wheat straw was provided by Asian Lignin Manufacturing Pvt. Ltd., Chandigarh, India. Elemental analysis (CHNSO) was performed using an elemental analyzer (628 Series, Sulfur add-on module, LECO Co., St. Joseph, MI, USA). Determination of structural carbohydrates, lignin, and ash was conducted according to the NREL standard procedures (Sluiter et al., 2005a; Sluiter et al., 2005b). The oxygen and carbohydrate contents were determined by difference. All the results with the corresponding values are listed in Table 4-1.

Acetone, 2-butanone, 1,4-dioxane, ethyl acetate, methanol, tetrahydrofuran (THF), and dialysis tubing cellulose membrane (molecular weight cut-off 14,000 Da) were purchased from Sigma-Aldrich Korea (Yongin, Republic of Korea).

Table 4-1. Elemental and chemical composition of herbaceous soda lignin

Properties	Value
Elemental analysis (wt%)	
Carbon	60.7 ± 0.1
Hydrogen	5.9 ± 0.4
Nitrogen	0.0 ± 0.0
Oxygen[*]	33.4 ± 0.3
Proximate analysis (wt%, dry basis)	
Carbohydrates[*]	8.6 ± 1.6
Acid-insoluble lignin	81.6 ± 1.6
Acid-soluble lignin	4.8 ± 0.2
Ash	5.1 ± 0.1

[*] calculated by difference

2.2. Functionalization of lignin

Sequential organic solvent fractionation of AL was performed according to the previous work, and the recovered fractions were denoted AL-F1, AL-F2, AL-F3, AL-F4, AL-F5, and AL-F6 (1,4-dioxane-insoluble). The yield of each soda lignin fraction (ALF) was determined gravimetrically.

Chemoselective methylation of AL was conducted to block the phenolic hydroxyl group (Kim et al., 2018). 1.6 g of AL was dissolved in 80 mL of aqueous 0.7 M sodium hydroxide at 25 °C. A different amount of dimethyl sulfate (0, 1, 2, and 6 mL) was introduced to each 1.6g of AL, and the mixture was heated to 70 °C for 2 h under vigorous stirring (Figure 4-1). The resulting products were then acidified with 2 M hydrochloric acid (pH below 2) to recover solid precipitates, followed by washing with deionized water three times and freeze-drying. Methylated lignin (ALM) powders were denoted AL-M0, AL-M1, AL-M2, and AL-M6 depending on the amount of added dimethyl sulfate, respectively.
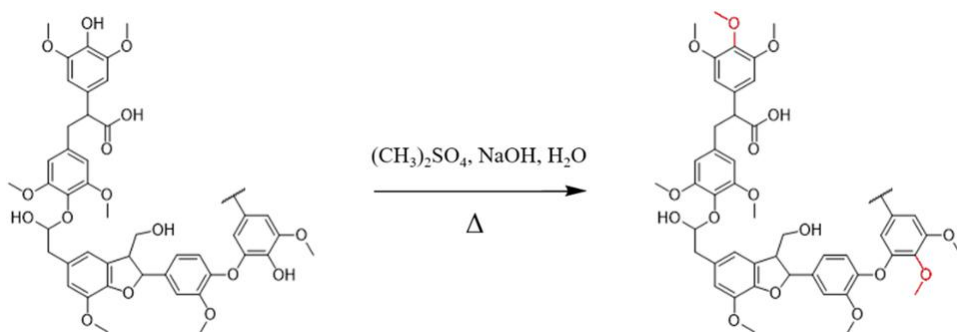
Figure 4-1. Chemoselective methylation of phenolic hydroxyl groups in lignin by dimethyl sulfate

2.3. Characterization of lignin

Quantification of lignin hydroxyl group content in lignin was performed using ^{31}P NMR spectra (Pu et al., 2011). 20 mg of lignin fraction was dissolved in 0.55 mL of pyridine/CDCl₃ mixture (1.6:1, v/v) under stirring and phosphorylated with 70 μL of 2-chloro-4,4,5,5-tetramethyl-1,3,2-dioxaphospholane (TMDP, Sigma-Aldrich Korea, Yongin, Republic of Korea). This product was then analyzed by a Bruker AVANCE 600 MHz instrument (Bruker, Billerica, MA, USA).

Lignin structures and lignin-carbohydrate complex (LCC) linkages were quantified by 2D-^{1}H-^{13}C HSQC NMR analysis (Sette et al., 2013). 60 mg of lignin dissolved in 1 mL of DMSO-d_6 was analyzed by a Bruker AVANCE™ 600 MHz applying a pulse sequence "hsqcedetgpsp.3" with a 90° pulse, 0.16 s acquisition time, 1.5 s relaxation delay, 32 scans, and acquisition of 1024 data points (for ^{1}H) over 512 increments (for ^{13}C). The central DMSO solvent peak was used as a reference (δ_C = 40.1; δ_H = 2.5). Relative quantitative analysis based on the 2D-HSQC spectra was carried out using the MestReNova® v12.0 software (Mestrelab Research, Santiago de Compostela, Spain) (Wen et al., 2013).

Methoxyl group content in lignin was determined by Baker's method (Baker, 1996). Lignin was reacted with hydroiodic acid at 130 °C for 30 min to release methyl iodide from the methoxyl groups, followed by the introduction of pentane and ethyl iodide (internal standard) under vigorous shaking. Finally, the pentane phase was analyzed using gas chromatography-mass spectrometry systems (5975C Series GC/MSD System, Agilent Technologies Inc.) to quantify the amount of methyl iodide formed by cleavage of the methoxyl group (Table 2-3).

The number and weight average molecular weights of ALFs were determined by GPC. Roughly 25 mg of sample dissolved in 1 mL of THF was introduced into 1260 Infinity II LC Systems (Agilent Technologies Inc., Santa Clara, CA, USA) equipped with a PLgel 5 μm MIXED-C column (300 × 7.5 mm, Agilent Technologies Inc.) and a RI detector (Table 2-2). Low molecular polystyrene

standards (Mp 266-66,000 Da, PSS Polymer Standards Service GmbH, Mainz, Germany) were used to calibrate the molecular weights of the analyte in the effluent (1.0 mL min^{-1}).

2.4. Synthesis of lignin nanoparticle

2.4.1. Pre-dialysis concentration

Synthesis of AL nanoparticles (ALNP) was conducted by modification from Lievonen's method (Lievonen et al., 2016). AL dissolved in THF at various concentrations was filtered with a 0.50 μm syringe filter. Because AL is partially dissolved in THF, the initial lignin input amount was adjusted to set pre-dialysis concentration (1, 2, 4, and 6 mg mL^{-1}) (Figure 4-2). This solution was then introduced into a dialysis tubing, which was pre-soaked and washed. The tubing was immersed in excess deionized water (replaced at intervals of 3 hours) for over 12 hours under stirring. Products were denoted ALNP-C1, ALNP-C2, ALNP-C4, and ALNP-C6, respectively. Each experimental variable was run in triplicate. The recovery of ALNP-Cs was calculated using Eq. (1):

$$Recovery\ of\ ALNPs\ (\%) = W_{ALNP}/W_t \times 100 \tag{1}$$

where W_t is the weight of total lignin and W_{ALNP} is the weight of ALNPs obtained by lyophilization (over 48 h) of a whole lignin suspension.
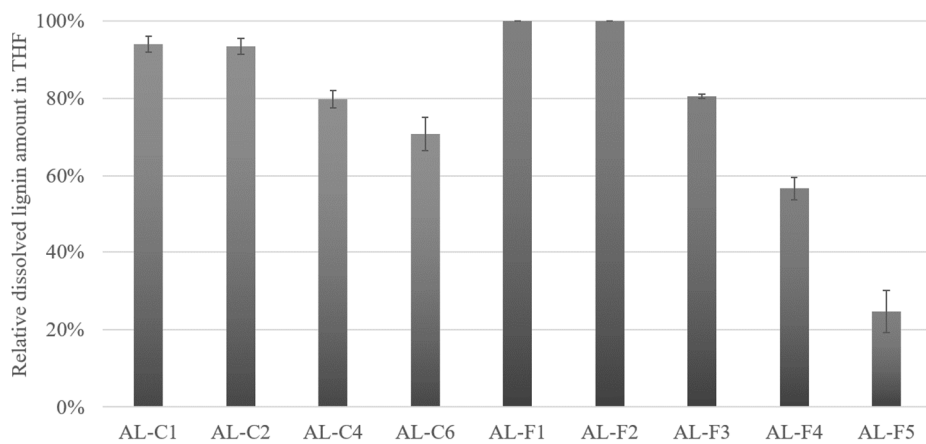
Figure 4-2. Relative dissolved amount of soda lignin (AL) in THF; AL-Cχ, χ mg AL mL^{-1} THF; AL-Fχ, 4 mg AL-Fχ mL^{-1} THF.

2.4.2. Functionalized lignin

Based on the pre-dialysis lignin concentration results in Section 3.2, ALFs and ALMs were dissolved in THF at a fixed concentration of 4 mg mL^{-1} (Figure 4-2). Filtration with a 0.50 μm syringe filter was followed by the nanoparticle formation process mentioned above. Products from ALFs were denoted ALNP-F1, ALNP-F2, ALNP-F3, ALNP-F4, and ALNP-F5, respectively. ALM-derived nanoparticles were also denoted ALNP-M0, ALNP-M1, ALNP-M2, and ALNP-M6, respectively. Each variable was also run in triplicate. The recovery rates of ALNP-Fs and ALNP-Ms were also calculated using Eq. (1).

2.5. Characterization of lignin nanoparticle

TEM image was obtained with the use of a LIBRA® 120 (Carl Zeiss, Oberkochen, Germany). The samples were deposited on thin carbon-coated copper 400 mesh TEM grid (Ted Pella, Inc., Redding, CA, USA), followed by solvent evaporation.

Mean diameter, PDI (the square of standard deviation/the square of mean diameter), and electrokinetic potential of ALNPs in colloidal dispersion by DLS were calculated using a Zetasizer Nano ZS instrument (Malvern Panalytical Ltd., Worcestershire, UK) along with a polystyrene cuvette (DTS0012, Malvern Panalytical Ltd.) and a folded capillary zeta cell (DTS1070, Malvern Panalytical Ltd.). Each sample was diluted in deionized water (0.1 mg mL^{-1}) and measured at 25 °C. Both peak sizes and Z-average size (harmonic intensity averaged size) were presented. The measured electrokinetic potential values were converted into zeta potential using Smoluchowski's formula (Hunter, 2013). Each value was obtained by averaging measurements of three samples.

The change of peak 1 size and zeta potential of ALNP-Cs in pure water was measured using the Zetasizer Nano ZS at different times (up to 28 days).

2.6. Biocompatibility test

The biocompatibility of ALNPs (C4, F1, F2, and F3) on A549 cells (ATCC®, CCL-185™, Manassas, VA, USA) and Lewis Lung Carcinoma cells (LLC, ATCC®, CRL-1642™) was ascertained by CCK-8 assays. Cell lines were grown in Dulbecco's Modified Eagle Medium (DMEM, Thermo Fisher Scientific, Waltham, MA, USA) containing 10% of fetal bovine serum (FBS, Atlas Biologicals, Fort Collins, CO, USA) and 1% of Antibiotic-Antimycotic solution (ABAM, GeneDireX, Las Vegas City, NV, USA). Grown cells were seeded and attached to 96-well plates (3×10^3 cells per well) overnight. After the medium was removed, serum-free DMEM with 1% ABAM and ALNPs with various concentrations (25, 50, 100, and 250 µg mL^{-1}) was added and cultured for multiple time conditions (24, 48, and 72 h for A549 and 8, 16, and 24 h for LLC). To examine cell viability, 10 µL of CCK-8 (Dojindo Molecular Technologies Inc., Kumamoto, Japan) was added into each well and incubated for 3 h at 37 °C. Subsequently, the absorbance at 450 nm was measured using a microplate reader (Sunrise™, TECAN Group Ltd., Männedorf, Switzerland). Cells incubated with DMEM supplemented with 10% of FBS, and 10% of Triton X-100 (TX, LPS solution, Daejeon, Republic of Korea) were used as positive and negative controls, respectively. Three replicates were used for each assay. All results were reported as the mean ± standard deviation (n = 3).

2.7. Statistical analysis

Statistical differences among groups were analyzed by analysis of variance (ANOVA), and the multiple t-tests were performed to compare differences between two groups. A p-value of <0.05 was considered significant.

3. Results and discussion

3.1. Characteristics of functionalized lignin
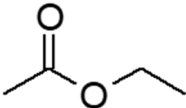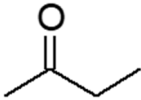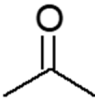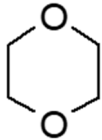
3.1.1. Lignin fractions

AL was sequentially fractionated with five organic solvents with different solubility, which is determined by several solvent properties such as the Hildebrand solubility parameter and Hansen solubility parameter. The solvency of selected solvents is given by a numerical value, the Hildebrand solubility parameter, which is an accurate representation of the square root of the cohesive energy density of the solvent. On the other hand, the Hansen solubility parameter utilizes the values of dispersion, polar, and hydrogen-bonding components of the Hildebrand parameter to quantify solvent–polymer compatibility. The parameters and properties of each solvent used in this study are presented in Table 4-2.

The yields of the six fractions (F1, F2, F3, F4, F5, and F6) were 8.9, 19.6, 32.5, 4.5, 15.4, and 19.1 wt%, respectively (Table 4-3). The number average molecular weights (M_n) and weight average molecular weights (M_w) of AL and its fractions were determined by GPC (Table 4-3 and Figure 4-3). AL had relatively small sizes and uniform molecular structure with M_w of 2,880 Da and dispersity (M_w/M_n) of 2.6 compared to the LignoBoost kraft lignin (KL, 4,580 Da and dispersity of 3.1, respectively). After fractionation, each ALF had a decreased M_w/M_n compared to raw AL. The M_w values of ALF increased from 1,060 Da for AL-F1 to 7,790 Da for AL-F5 as the fractionation progressed. However, GPC data from AL-F6 was could not obtain because it did not dissolve in THF. This trend of increasing molecular weight as sequential extraction progresses is in agreement with previous studies of successive lignin solvent extractions (An et al., 2017; Araujo et al., 2020). AL-F1 to A4 had relatively low M_w/M_n values of 1.7~2.0, and

F5 had a high M_w/M_n of 4.0, the highly polydisperse, compared to raw AL (2.6). Although AL and KL underwent the same solvent extraction process, the yields and molecular weights of AL fractions were different from KL fractions (Table 2-4), implying the molecular structural difference between them.

Table 4-2. Solubility parameters and related properties of five different solvents used in this study

	Solvent (at 25 °C)				
	Ethyl acetate	2-Butanone	Methanol	Acetone	1,4-Dioxane
Hildebrand solubility parameters[a]	9.1	9.3	14.3	9.8	10.0
Hansen solubility parameters[b]	18.1	19.1	29.6	20.0	20.5
Polar component[b]	5.3	9.0	12.3	10.4	1.8
Hydrogen bonding component[b]	7.2	5.1	22.3	7.0	7.4

[a] Hansen (1967)

[b] Barton (1991)

Table 4-3. The fractions yield of AL and their GPC information

	Yield (%)	M_w	M_n	M_w/M_n
AL		2,880	1,130	2.6
AL-F1	8.9	1,060	610	1.7
AL-F2	19.6	1,780	1,050	1.7
AL-F3	32.5	2,920	1,480	2.0
AL-F4	4.5	4,990	2,420	2.0
AL-F5	15.4	7,790	1,950	4.0
AL-F6	19.1	ND[*]	ND	ND

[*] not dissolved in THF
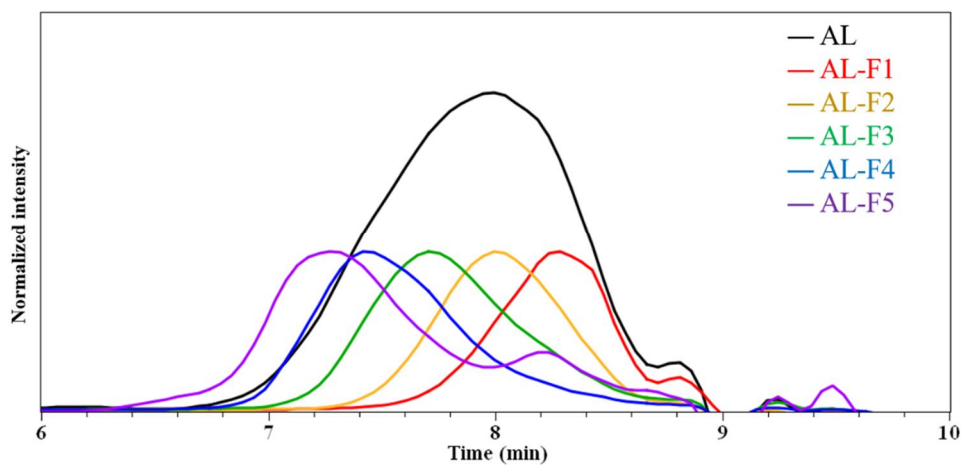
Figure 4-3. GPC curves of AL and its fractions by solvent extraction

Functional group content (methoxyl and hydroxyl) of ALFs was quantitatively determined, and the results are shown in Table 4-4; hydroxyl group (132~150 ppm) regions of ^{31}P NMR spectra are shown in Figure 4-4. The results showed a decrease in total hydroxyl groups as the fractionation progressed. Specifically, total phenolic hydroxyl groups decreased from 2.84 mmol g^{-1} for AL-F1 to 0.98 mmol g^{-1} for AL-F5. In addition, the hydroxyl group from diphenyl ether structure in AL-F4 and F5 disappeared. But only phenolic hydroxyl group content in syringyl unit did not show clear decreasing trend (F2 > F1 > F4 > F3 > F5). Aliphatic hydroxyl group content increased throughout the fractionation process. However, the lowest content of aliphatic hydroxyl groups was obtained from AL-F2, followed by F4 and F3, rather than from F1. Any fractions did not show aliphatic hydroxyl group content over raw AL. Thus it can be predicted that AL-F6, the insoluble fraction, has relatively higher free aliphatic hydroxyl group content.

HSQC spectra consisted of cross-peaks of protons and carbons were analyzed to determine the structure related to phenylpropanoid units and interunit linkages in ALFs. Quantitative measurement of main interunit linkages in AL, β-aryl ether (β-O-4), resinol (β-β), and phenylcoumaran (β-5), was carried out based on the spectra with total aromatic units as an internal standard (Wen et al., 2013). Relative amounts of main interunit linkages in AL and derived fractions are listed in Table 4-5; the sidechain (δ_C/δ_H 50~90/2.5~6.0) and aromatic (δ_C/δ_H 100~135/5.5~8.0) regions of HSQC spectra are shown in Figures 4-5 and 6. In the raw AL spectra, very weak cross signals of major linkages and aromatic groups were observed, inferring its very low abundance of cleavable β-O-4 and the highly condensed molecular structure. Whereas there was a strong signal (δ_C/δ_H 75.4/3.5) that belongs to the phenylglycerol structure, which is suspected to be generated from the cleaved nonphenolic β-O-4 ether bonds by NaOH (Zhao et al., 2019). The relative amount of β-O-4, β-β, and β-5 in AL per 100 aromatic units were 5.8, 5.4, and 2.7, respectively. In the AL-F1 and F2 spectra, strong cross signals of C–H from aromatic moieties were determined, but the signals of C-H from internal

linkages were relatively much weaker than the raw one. This observation correlated with higher phenolic hydroxyl group content and indicates that AL-F1 and F2 are highly condensed phenolic oligomers. AL-F4 and F5 had the highest amount of β-β and β-O-4 linkage, respectively, among the lignin fractions. Note that the cross signals of proton and carbon from AL-F4 and F5 were, unfortunately, too weak to predict their molecular structure.

Table 4-4. Content in hydroxyl groups of AL fractions quantified by ^{31}P NMR and methoxy group

| | Hydroxyl (mmol g^{-1}) | | | | | | Methoxy (mmol g^{-1}) |
| | Phenolic | | | | Carboxylic acids | Aliphatic | |
	H	G	S	4-O-5			
AL	0.29	0.91	0.81	0.14	1.31	2.38	3.59
AL-F1	0.41	1.12	0.76	0.55	2.05	1.57	3.92
AL-F2	0.38	1.11	0.91	0.09	1.41	1.10	3.97
AL-F3	0.22	0.75	0.58	0.03	1.12	1.53	3.55
AL-F4	0.14	0.60	0.69	ND[*]	0.67	1.52	3.40
AL-F5	0.10	0.46	0.42	ND	0.60	2.01	3.07

[*] not detected
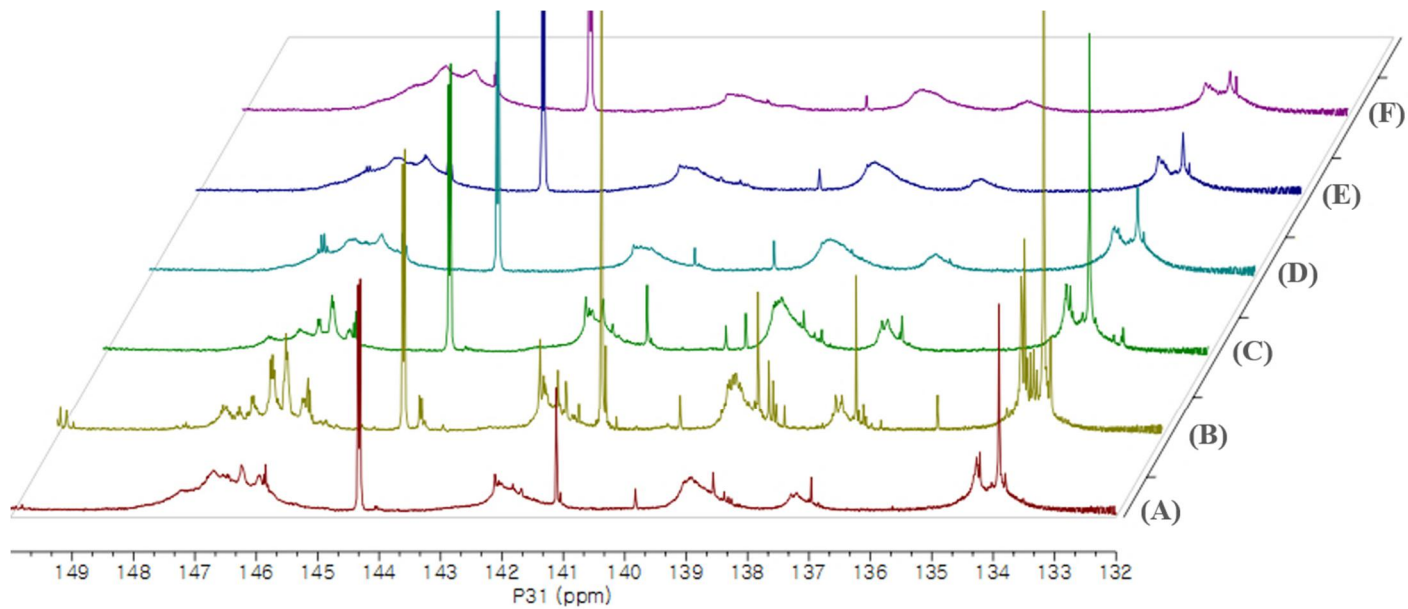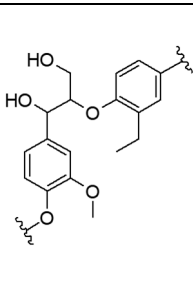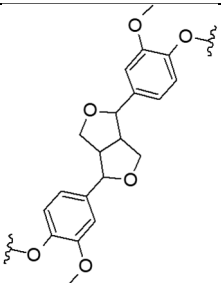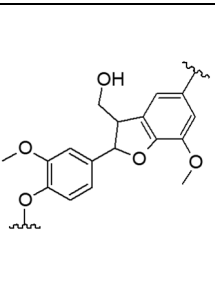
Figure 4-4. ^{31}P NMR spectra of (A) AL, (B) AL-F1, (C) AL-F2, (D) AL-F3, (E) AL-F4, and (F) AL-F5

Table 4-5. Relative amounts of main interunit linkages in AL and its fractions

Samples	Linkage amount (per 100 aromatic units)			
	β-O-4	β-β	β-5	S:G:H
AL	5.8	5.4	2.7	32:48:20
AL-F1	0.5	2.8	0.4	33:44:23
AL-F2	1.9	1.5	0.4	35:48:17
AL-F3	6.1	1.3	0.9	36:50:14
AL-F4	8.8	9.0	ND[*]	37:45:18
AL-F5	12.1	ND	ND	4:82:14

[*] not detected
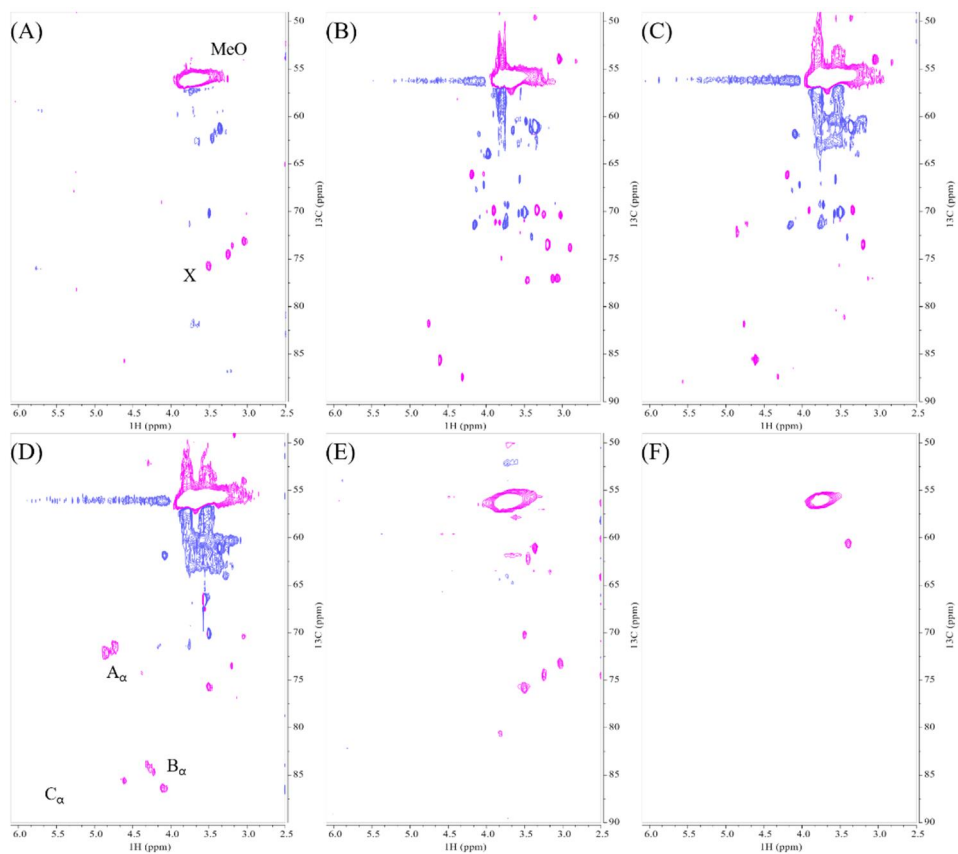
Figure 4-5. Sidechain regions in the 2D-HSQC NMR spectra of (A) AL, (B) AL-F1, (C) AL-F2, (D) AL-F3, (E) AL-F4, and (F) AL-F5; A_α, C_α-H_α in β-O-4; B_α, C_α-H_α in β-β; C_α, C_α-H_α in phenylcoumaran; OMe, C-H in methoxyls; X, C-H in phenylglycerol.
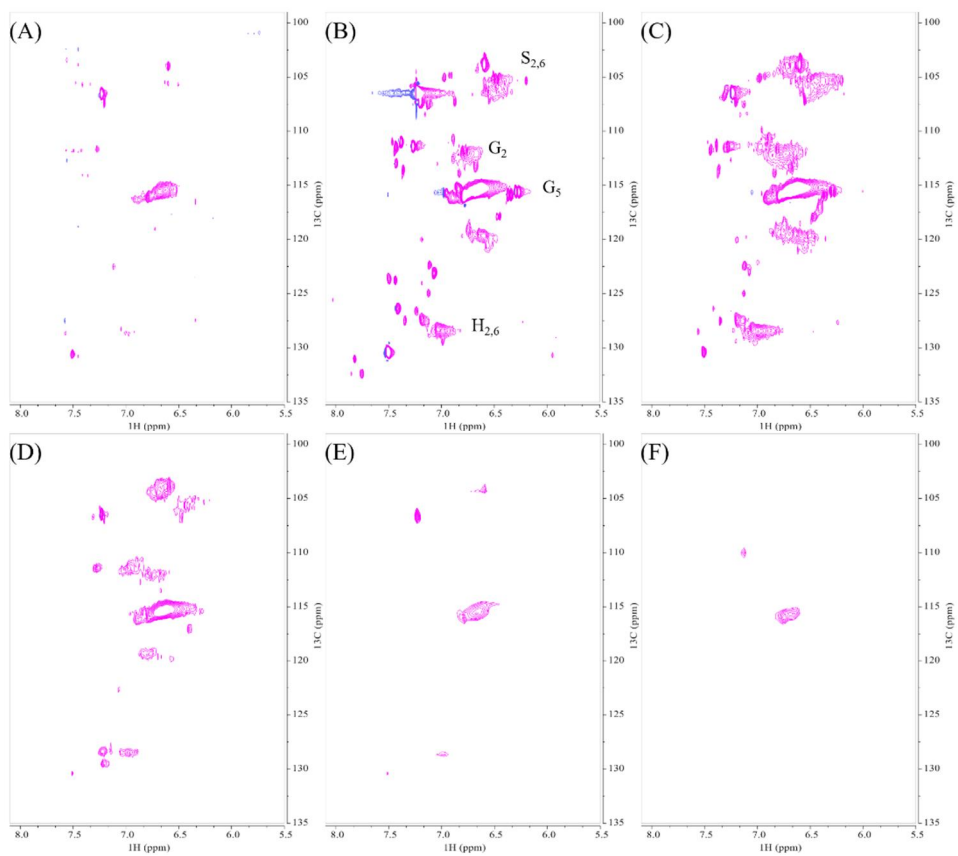
Figure 4-6. Aromatic/unsaturated regions in the 2D-HSQC NMR spectra of (A) AL, (B) AL-F1, (C) AL-F2, (D) AL-F3, (E) AL-F4, and (F) AL-F5; S_n, $C_n–H_n$ in syringyl units; G_n, $C_n–H_n$ in guaiacyl units; H_n, $C_n–H_n$ in hydroxyphenyl units.

3.1.2. Lignin methylation

Phenolic hydroxyl group-selective methylation was carried out in neat DMS as a solvent at 70 °C for 2 h using NaOH due to its relatively mild condition. Quantification of lignin hydroxyl group content in ALMs was performed using ^{31}P NMR spectra. The number and weight average molecular weights of a series of ALMs were also determined by GPC.

Quantitative determination of the phenolic hydroxyl group shows that ALMs were well methylated (Table 4-6). After methylation, total phenolic hydroxyl groups significantly decreased as an increased amount of reacted DMS, from 2.15 mmol g^{-1} for AL to 0.17 mmol g^{-1} for AL-M6. It indicates that the phenolic hydroxyl group-specific methylation of AL was successfully performed.

The M_n and M_w of ALNP-Ms are listed in Table 4-7, and the chromatogram is shown in Figure 4-7. This result showed that the M_w of AL-M0 (heated but non-methylated) was slightly lower than that of AL, but the difference was not significant. The M_w values of ALMs increased from 3,291 Da for AL-M1 to 4,243 Da for AL-F6 as the degree of methylation increased. In addition, M_w/M_n of methylated lignin ranged from 2.4 to 3.2, which did not show a remarkable difference to neat AL.

Table 4-6. Changing the content of phenolic hydroxyl groups in methylated AL quantified by ^{31}P NMR

	Phenolic hydroxyl (mmol g^{-1})			
	H	G	S	4-O-5
AL	0.29	0.91	0.81	0.14
AL-M0	0.22	0.87	0.78	0.14
AL-M1	0.15	0.55	0.43	0.05
AL-M2	0.08	0.30	0.20	0.03
AL-M6	ND[*]	0.08	0.08	0.01

[*] not detected

Table 4-7. GPC information of methylated AL

	M_w	M_n	$M_\mathrm{w}/M_\mathrm{n}$
AL	2,880	1,130	2.6
AL-M0	2,696	1,248	2.2
AL-M1	3,291	1,372	2.4
AL-M2	3,460	1,354	2.6
AL-M6	4,243	1,339	3.2
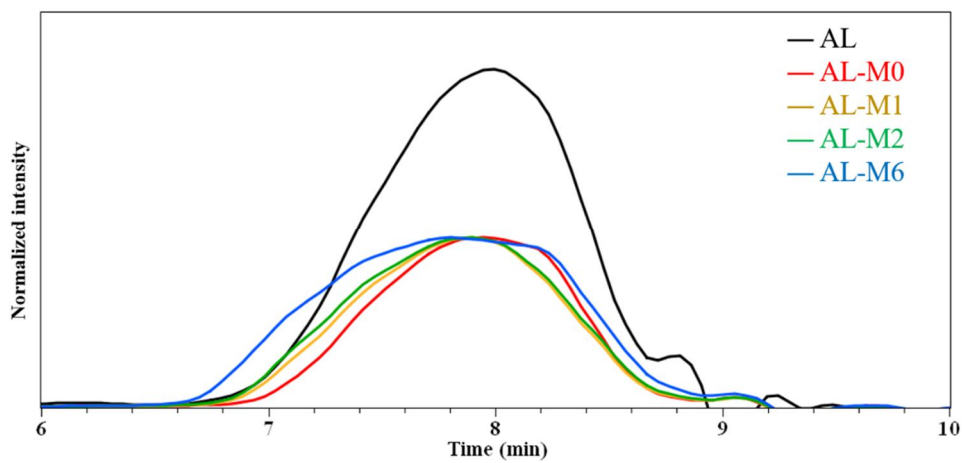
Figure 4-7. GPC curves of raw and methylated ALs

3.2. Effect of lignin characteristics on nanoparticle size

3.2.1. Effect of solvent fractionation

Figure 4-8 shows the recovery of resultant ALNPs that were centrifuged and freeze-dried to determine the conversion rate. All the samples except ALNP-F5 (77.8%) had high nanoparticle yield, from 85.8% for ALNP-F3 to 96.8% for ALNP-F3, a total average yield of 91.6%.

The initial pre-dialysis concentration of lignin guided the average particle size and distribution of nanoparticles. The smallest Z-average size of 671.9 nm and also the narrowest PDI among ALNP-Cs were obtained at 4 mg mL^{-1} concentration (Table 4-8). By contrast, the smallest peak size of 414 nm was obtained at 1 mg mL^{-1} concentration (Figure 4-9). However, ALNP-C1 presented the largest Z-average size among all samples (1,903 nm) and a PDI value of 1.0, which is theoretically the highest value. Despite identifying a clear single peak in the graph, it is hard to dismiss the exceptional result of Z-average cumulant analysis of the measured correlation curve of ALNP-C1. Because this could happen when the largest size peak is larger than the large cut-off of DLS (e.g., very large aggregates or dust). Therefore, ALNP-C4, which showed the smallest Z-average size, PDI, and the second smallest peak size, was chosen to be a representative nanoparticle in this study. On the other hand, the peak sizes and their standard deviation were both enlarged as the lignin concentration increased ($R^2 = 0.66$). But the Z-average sizes and PDI showed a weak decreasing trend as the pre-dialysis concentration increased due to the outlier peak size from ALNP-C1 ($R^2 = 0.29$).

The average particle size and distribution of lignin nanoparticles were affected by the sequential solvent extraction. As shown in Table 4-8, particles derived from low-molecular-weight fractions had bigger sizes than the control group (ALNP-C4) or high-molecular-weight groups. In detail, the largest nanoparticle consisted of fraction 1 with lower M_w and higher hydrophilic functional group content, while

particles with similar size compared to the control were obtained from fractions of higher M_w and lower hydrophilic group content (Figure 4-10). Since THF is exchanged to water by dialysis, hydroxyl group and/or carboxylic group in the polymer could interact with water molecules, interfacial tension increases (Jensen et al., 2004), nucleation rate decreases (D'Addio & Prud'homme, 2011), and less number of initial nuclei forms (Martinez Rivas et al., 2017). Because of the relatively small amount of nuclei, each nucleus could grow larger until a solute concentration is reduced below the equilibrium saturation concentration. In addition, a high tendency for self-association due to the strongly interacting surface hydroxyl groups in ALFs is considerable. Meanwhile, ALNP-F4 and F5 had multi-peak size distributions. Especially three different peaks of ALNP-F5 had a very low intensity, which hints at its varied size and unstable colloidal property.

The correlations between particle size and several features of the lignin are presented in Figure 4-11. There were no very high correlations between particle size and structural characteristics of ALFs. Specifically, fractions with higher M_w highly tend to form smaller nanoparticles ($R^2 = 0.77$). On the other hand, the carboxylic group, phenolic, and total hydroxyl group content in the lignin are correlated well with the increasing Z-average size of ALNP-Fs ($R^2 = 0.67$, 0.63, and 0.61, respectively). A negative correlation between the relative amount of β-O-4 and particle size is also significant ($R^2 = 0.68$). Therefore, it could be assumed that the hydrogen bond formation between hydroxyl groups encourages nucleation or condensation during the nanoprecipitation process. However, the aliphatic hydroxyl group had a low correlation with the particle size ($R^2 = 0.25$).

The morphology of ALNPs was determined by TEM images (Figure 4-12). Nearly spherical shaped particles were obtained while ALNP-F5 had some irregular sphere morphological structures.
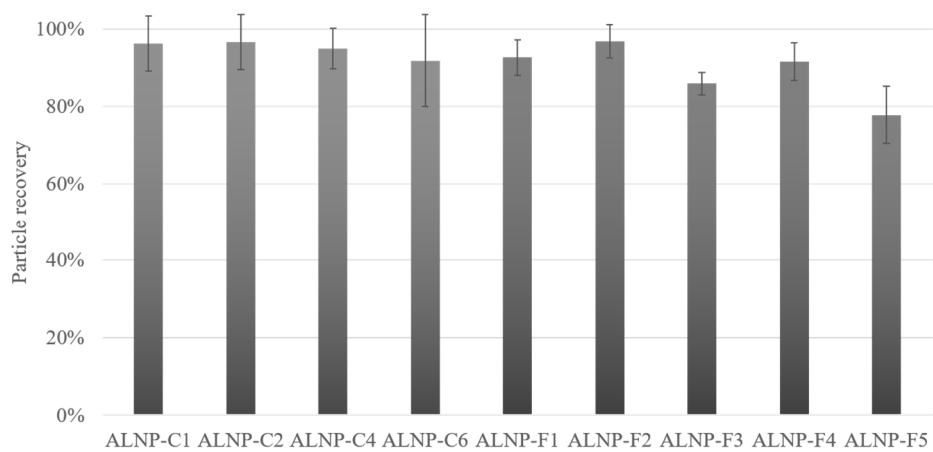
Figure 4-8. Recovery of nanoparticles as functions of pre-dialysis soda lignin concentration and fractionation

Table 4-8. Size properties of fraction-derived AL nanoparticles

	Peak size (nm)						Z-average size (nm)	PDI
	Peak 1	Intensity (%)	Peak 2	Intensity (%)	Peak 3	Intensity (%)		
ALNP-C1	414	100	-	-	-	-	1,903	1.000
ALNP-C2	741	100	-	-	-	-	729.6	0.346
ALNP-C4	721	100	-	-	-	-	671.9	0.118
ALNP-C6	840	100	-	-	-	-	959.9	0.381
ALNP-F1	953	100	-	-	-	-	1,103	0.276
ALNP-F2	732	100	-	-	-	-	704.6	0.002
ALNP-F3	733	100	-	-	-	-	796.8	0.253
ALNP-F4	701	97.0	5,313	3.0	-	-	740.9	0.244
ALNP-F5	128	50.5	1,241	34.9	4,942	14.5	286.9	0.731
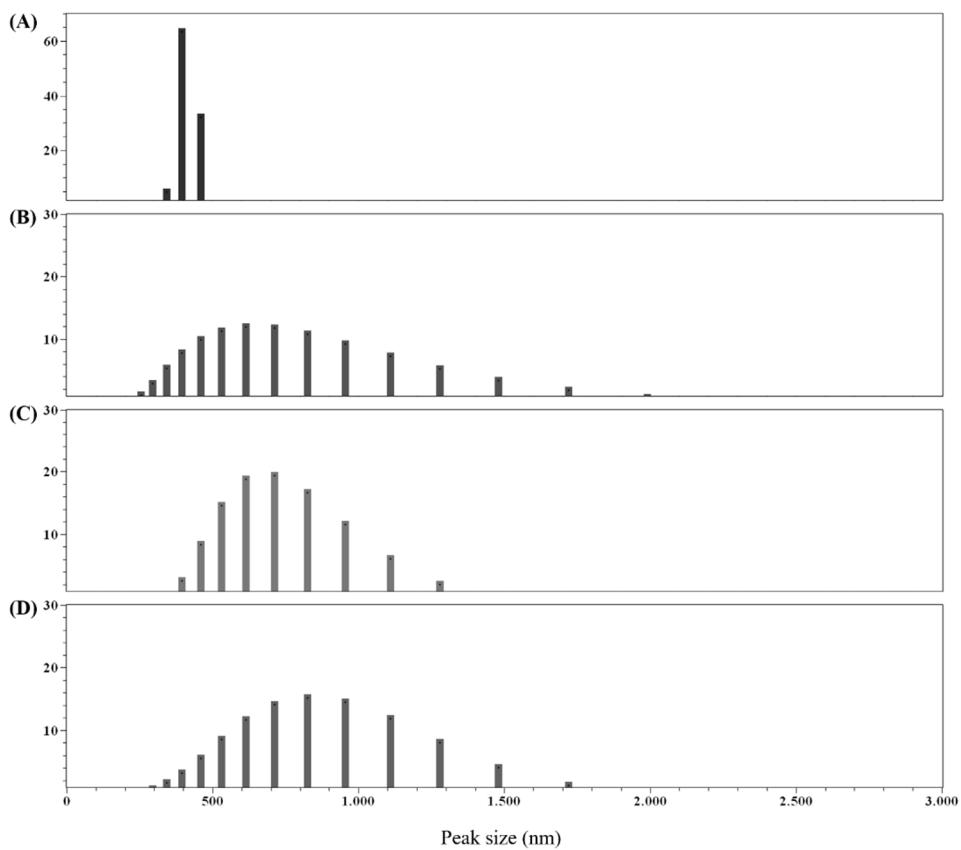
Figure 4-9. Peak size graph of ALNP-Cs. (A) ALNP-C1, (B) ALNP-C2, (C) ALNP-C4, and (D) ALNP-C6.
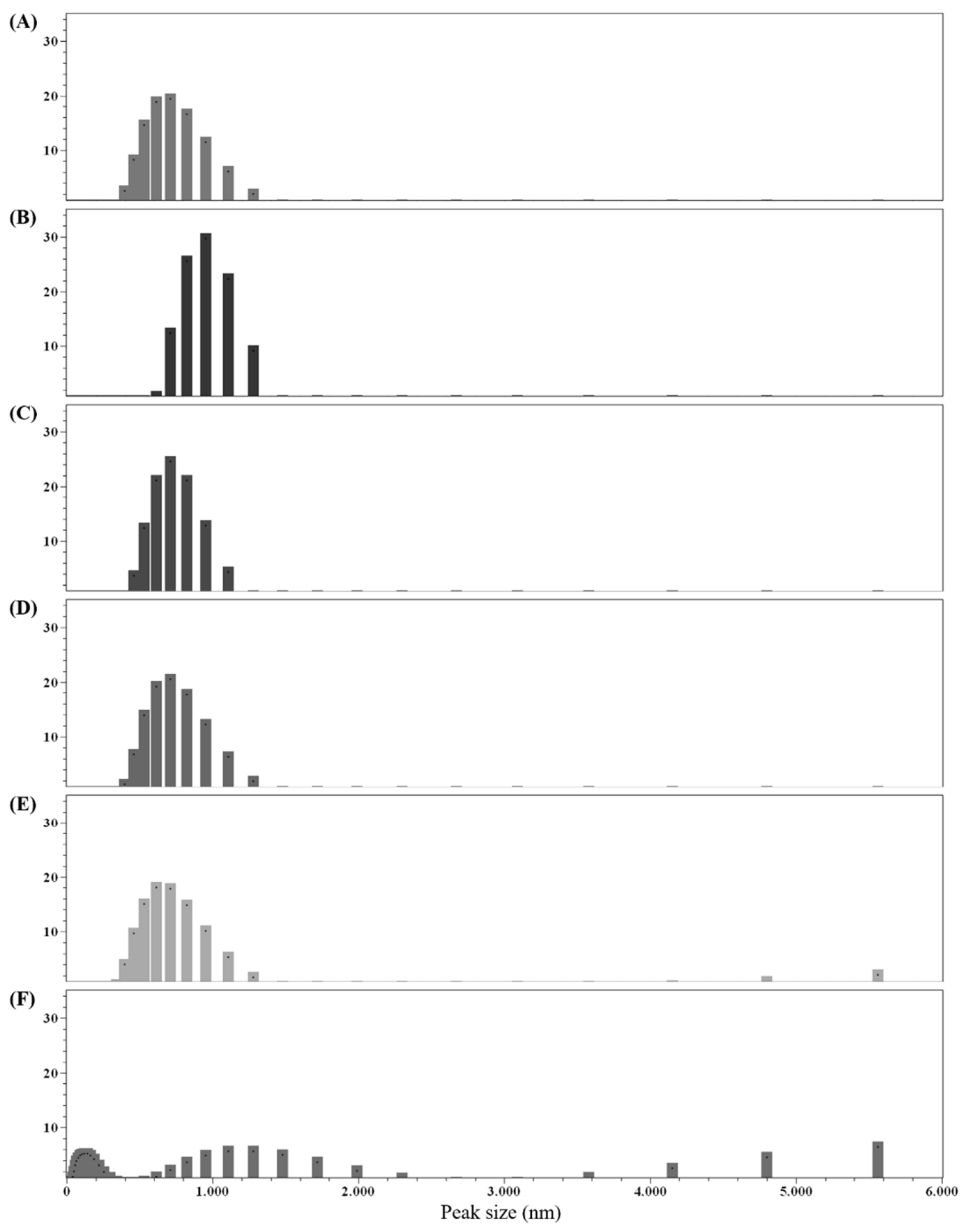
Figure 4-10. Peak size graph of ALNP-Fs. (A) ALNP-C4, (B) ALNP-F1, (C) ALNP-F2, (D) ALNP-F3, (E) ALNP-F4, and (F) ALNP-F5.
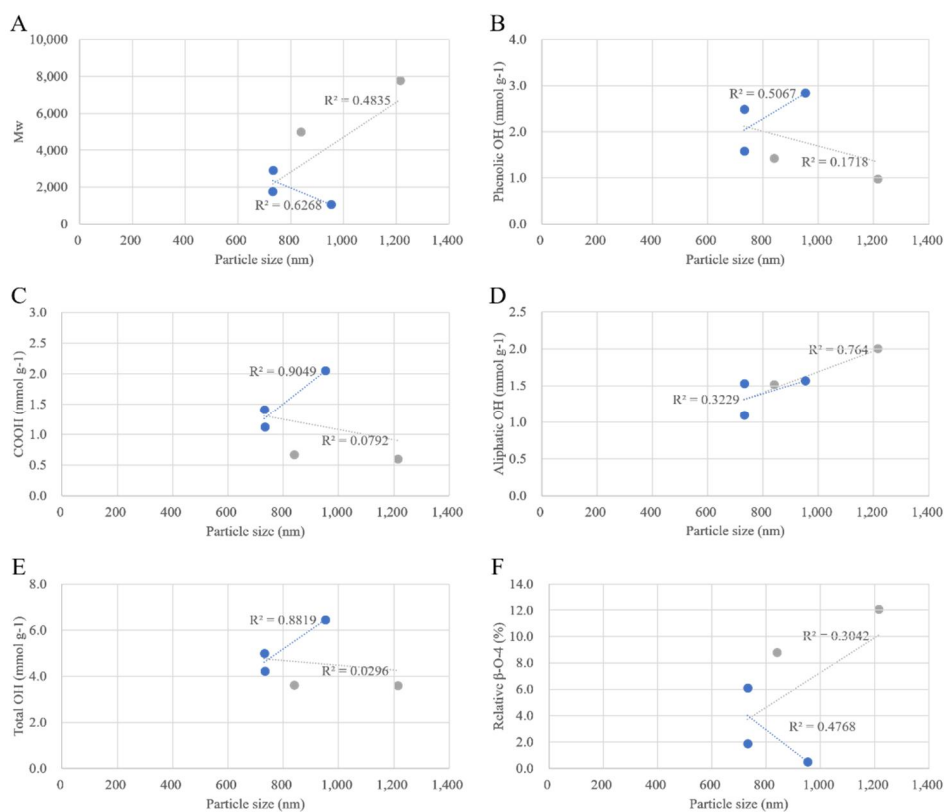
Figure 4-11. Peak average size distribution of ALNPs as functions of structural characteristics. (A) M_w, (B) phenolic hydroxyl, (C) carboxylic acid, (D) aliphatic hydroxyl, (E) total hydroxyl content, and (F) relative β-O-4. Blue dots represent the properties of ALNPs with monomodal size distribution (ALNP-F1, F2, and F3). Achromatic dots represent the properties of ALNPs with multimodal size distribution (ALNP-F4 and F5)
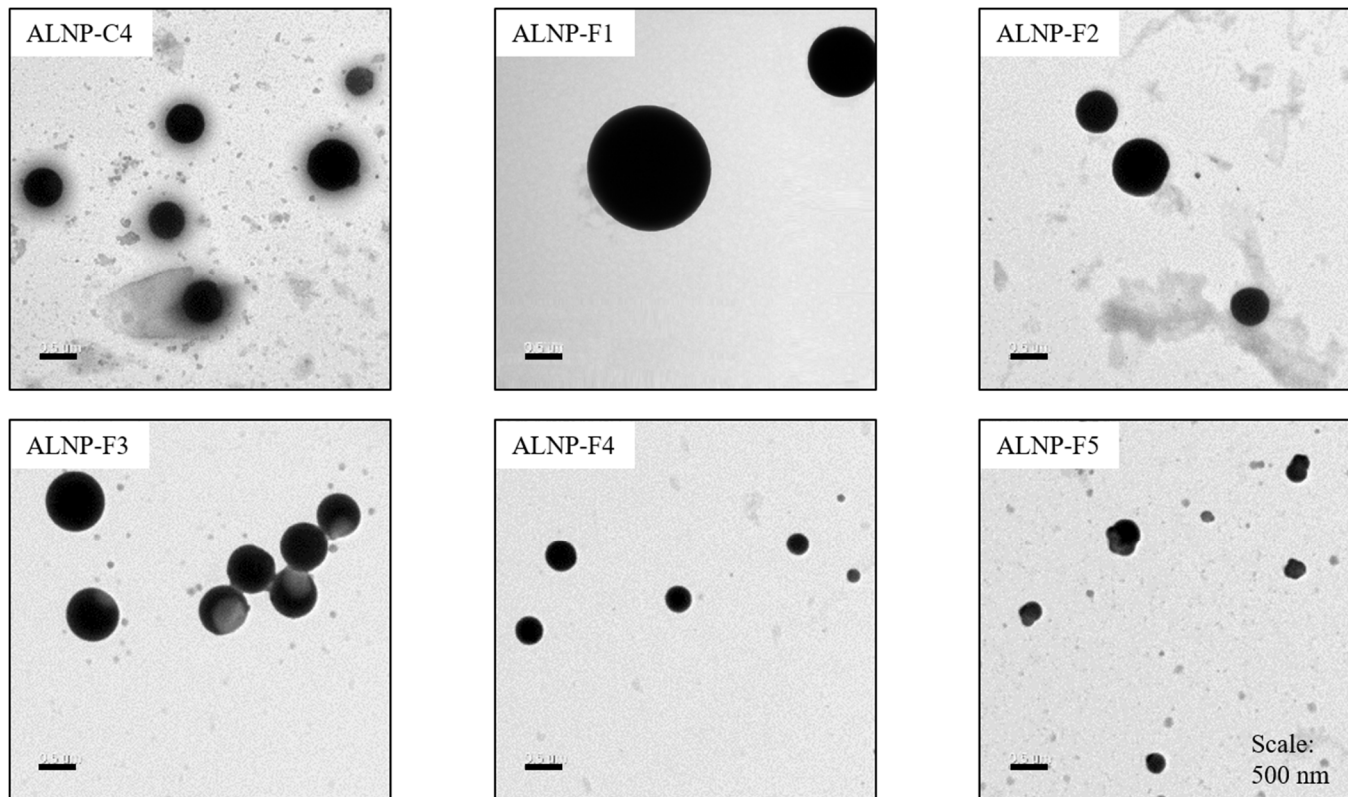
Figure 4-12. TEM images of ALNPs with lignin fractions

3.2.2. Effect of the hydroxyl group

The methylation process influenced the average particle size and distribution of nanoparticles. Both peak sizes and Z-average sizes decreased by decreasing the content of the phenolic hydroxyl group and/or molecular weight (Table 4-9). Although there was no identified remarkable difference between neat AL and AL-M0 structures, the Z-average size was significant (672 and 915 nm, respectively). However, the difference in a single peak of size between AL and AL-M0 was not meaningful. As shown in Figure 4-13, larger nanoparticles consisted of less-methylated lignin with lower M_w and higher phenolic hydroxyl group content (AL-M0 and M1). Simultaneously, smaller particles with multi-peak size distribution were obtained from highly methylated lignin with higher M_w and lower phenolic hydroxyl group content (AL-M2 and especially M6). This result is in agreement with previous works with the formation of nanoparticle from lignin fractions, which have low hydroxyl group content. It is assumed that the higher phenolic hydroxyl group content is related to the synthesis of even-sized lignin nanoparticles.

The correlations between particle size, molecular weight, and hydroxyl groups of the ALNP-Ms are presented in Figure 4-14. There was a very high correlation between particle size and phenolic hydroxyl group content of ALMs ($R^2 = 0.95$). Total hydroxyl group content also showed a very high correlation with the particle size ($R^2 = 0.93$). But it is not meaningful due to the little change of aliphatic and carboxylic hydroxyl group content during the methylation. Consequently, it could be interpreted that the phenolic hydroxyl groups in lignin have the key role of nucleation or condensation during the nanoprecipitation process.

Table 4-9. Size properties of methylated AL nanoparticles

	Peak size (nm)						Z-average size (nm)	PDI
	Peak 1	Intensity (%)	Peak 2	Intensity (%)	Peak 3	Intensity (%)		
ALNP-C4	721	100	-	-	-	-	671.9	0.118
ALNP-M0	754	100	-	-	-	-	915.2	1.000
ALNP-M1	629	100	-	-	-	-	825.5	0.506
ALNP-M2	519	92.8	138	6.0	1,480	1.1	553.5	0.390
ALNP-M6	586	74.6	87	22.2	1,931	3.1	462.6	0.406
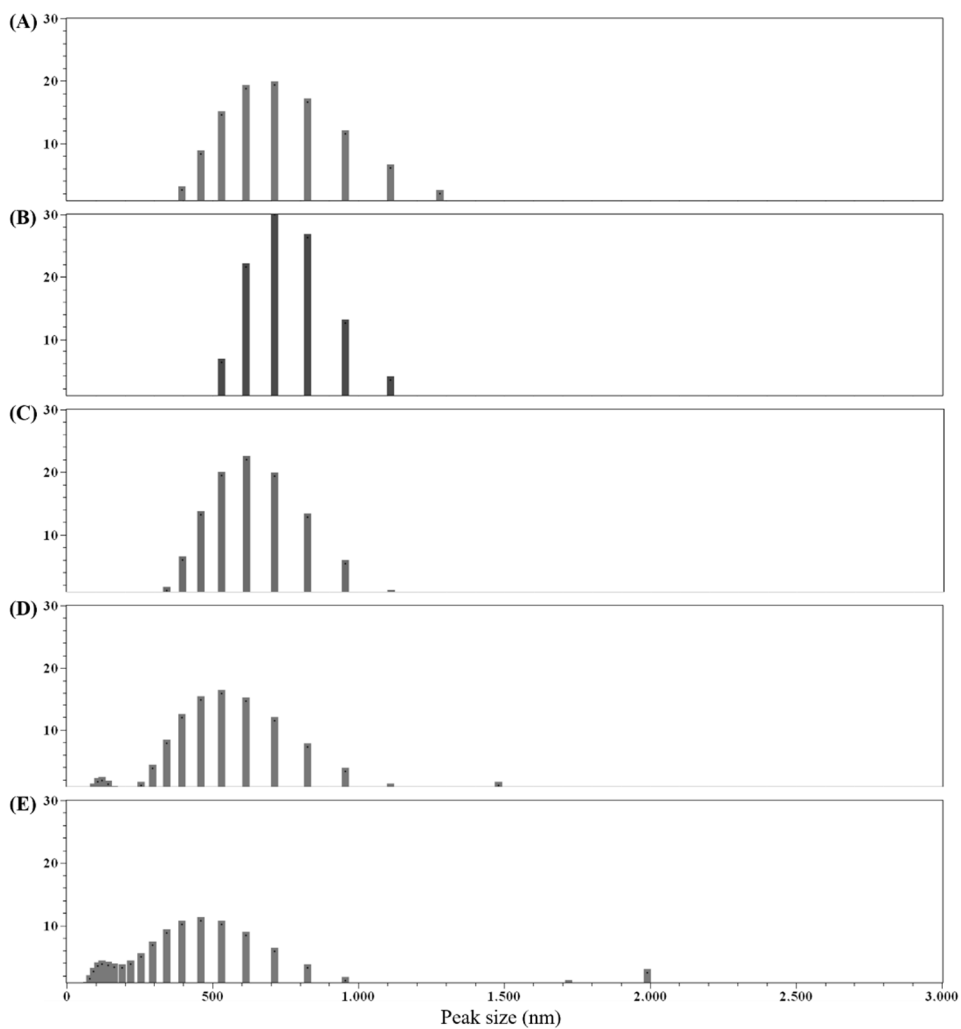
Figure 4-13. Peak size graph of ALNP-Ms. (A) ALNP-C4, (B) ALNP-M0, (C) ALNP-M1, (D) ALNP-M2, and (E) ALNP-M6.
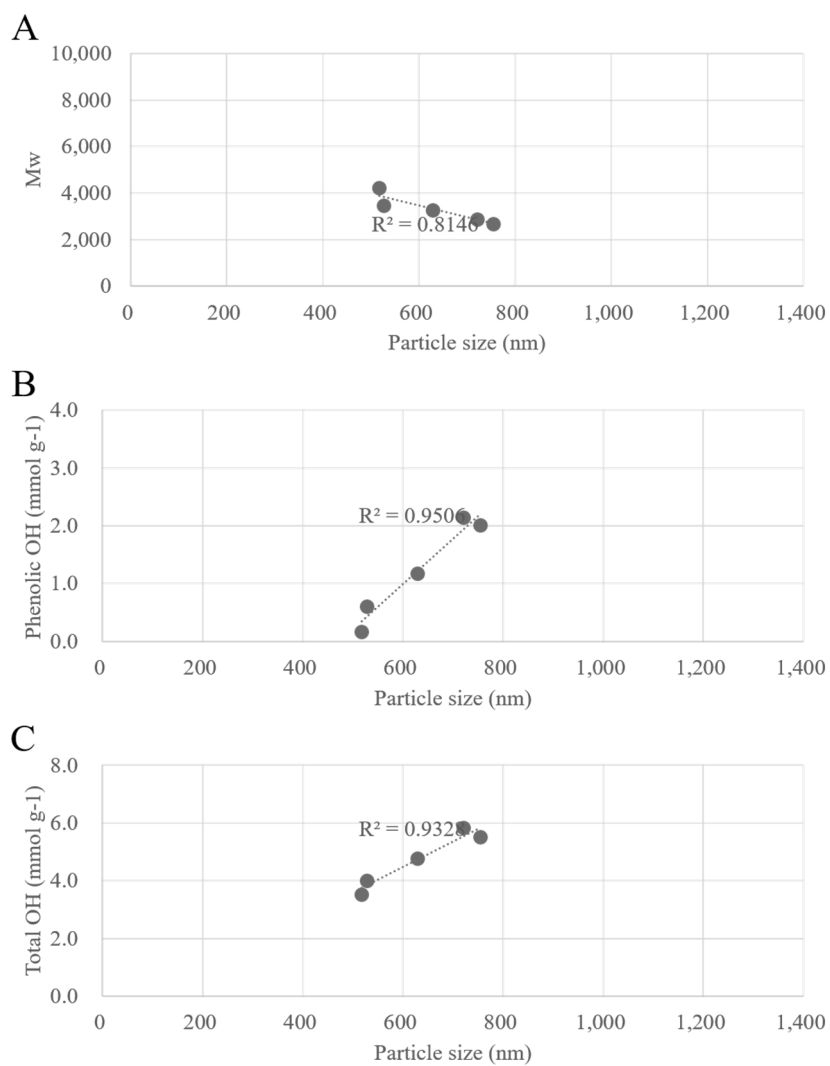
Figure 4-14. Peak average size distribution of ALNPs as functions of structural characteristics. (A) M_w, (B) phenolic hydroxyl, and (C) total hydroxyl content.

3.3. Particle surface charge

Zeta potential is a potential difference between the mobile dispersion medium and the stationary layer of the dispersion medium attached to the dispersed particle, applied to determine electrokinetic potential in colloidal systems (Clogston & Patri, 2011). Zeta potential values are typically in the range of 100 to -100 mV, but the nanoparticles with the values >30 or <-30 usually have a high degree of stability (Sapsford et al., 2011). Lower dispersions zeta potential values will lead to aggregation, coagulation, or flocculation due to van der Waals interparticle attraction (Horie & Fujita, 2011; Sapsford et al., 2011).

In this study, zeta potential values for all samples exceeded -30 mV, indicating relatively high-water stability. Pre-dialysis concentration of lignin negatively affected zeta potential ($R^2 = 0.96$). Zeta potential value decreased from -42.3 mV for ALNP-C1 to -37.2 mV for ALNP-C6 (Figure 4-15). On the contrary, no significant trend of changing zeta potential value concerning the solvent extraction process or the size of ALNP was observed.

The methylation level of lignin hydroxyl groups also negatively affected zeta potential, from -42.3 mV for ALNP-M0 to -33.0 mV for ALNP-M6, but the correlation ($R^2 = 0.69$) was lower than that of pre-dialysis concentration.
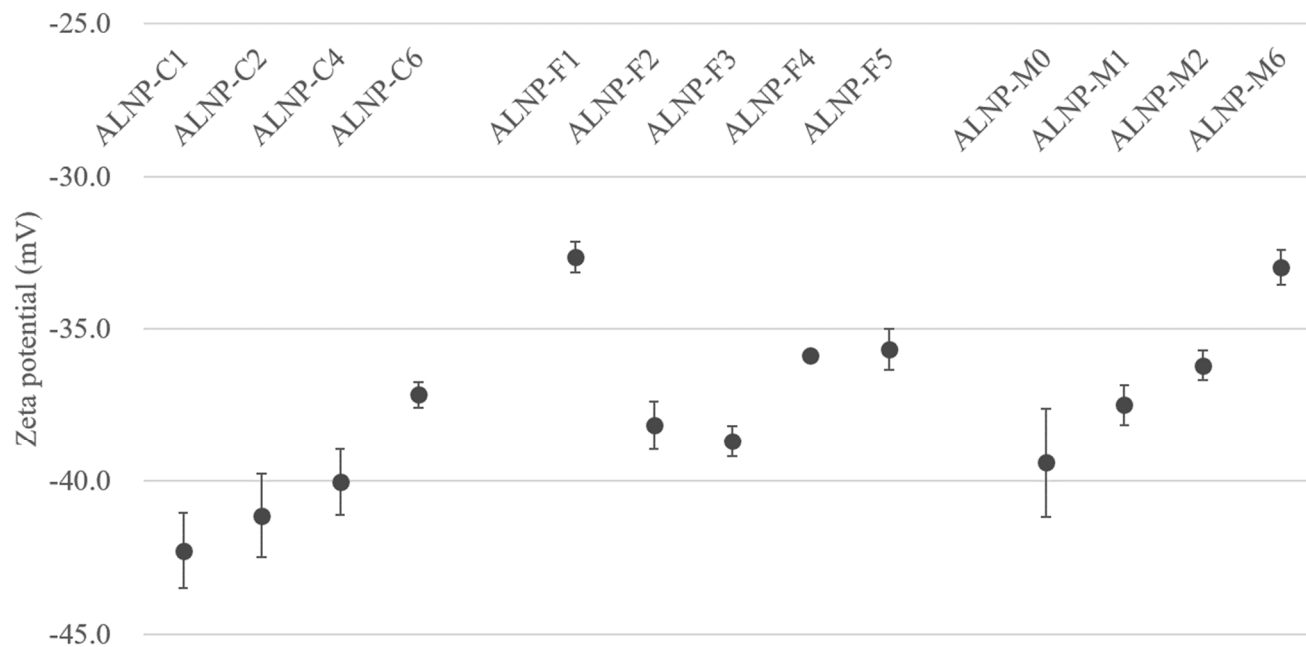
Figure 4-15. Zeta potential values of ALNPs as functions of various conditions

3.4. Storage stability of nanoparticle

To investigate the storage stability of colloidal ALNPs in terms of size and surface charge, peak size and zeta potential were analyzed at a different time interval (Table 4-10 and Figure 4-16).

ALNP-Cs showed slight changes in particle size after 28 days of storage in deionized water. Specifically, ALNP-C1 and C4 led little change of size on average for 28 days, although all the size values were not perfectly matched for the weak increasing tendency. On the other hand, ALNP-C2 and C6 increased steadily from 741 nm and 840 nm to 1,056 nm and 1,035 nm, respectively.

The zeta potential value of ALNP-Cs also increased with time. It means that the surface stability of the particle decreased. Still, it is assumed that the relatively high negative zeta potential impeded the nanoparticle growth by coagulation. Still, the increasing rates of both zeta potential and particle size are low, there is no significant instability with long-time storage.

Table 4-10. Summary of soda lignin nanoparticle stability in the pure water of change in time

		Days after synthesis					
		0 days	3 days	7 days	14 days	21 days	28 days
Peak 1 size (nm)	ALNP-C1	414 ± 7	375 ± 26	374 ± 26	363 ± 13	450 ± 107	401 ± 64
	ALNP-C2	741 ± 65	741 ± 172	772 ± 137	806 ± 100	823 ± 163	1,056 ± 266
	ALNP-C4	721 ± 99	667 ± 85	797 ± 149	708 ± 122	720 ± 178	828 ± 111
	ALNP-C6	840 ± 149	785 ± 108	862 ± 245	799 ± 277	776 ± 303	1,035 ± 186
Zeta potential (mV)	ALNP-C1	-42.3 ± 1.4	-41.3 ± 0.0	-40.0 ± 0.4	-39.9 ± 0.9	-39.0 ± 1.7	-36.0 ± 2.4
	ALNP-C2	-41.1 ± 0.2	-35.9 ± 0.6	-35.0 ± 0.8	-34.7 ± 0.6	-34.4 ± 0.1	-32.7 ± 1.0
	ALNP-C4	-40.0 ± 0.2	-38.1 ± 1.1	-34.9 ± 0.7	-34.2 ± 0.7	-35.0 ± 1.2	-34.5 ± 1.1
	ALNP-C6	-37.2 ± 0.4	-30.9 ± 0.6	-28.0 ± 0.7	-27.0 ± 0.3	-27.1 ± 0.3	-27.0 ± 0.5
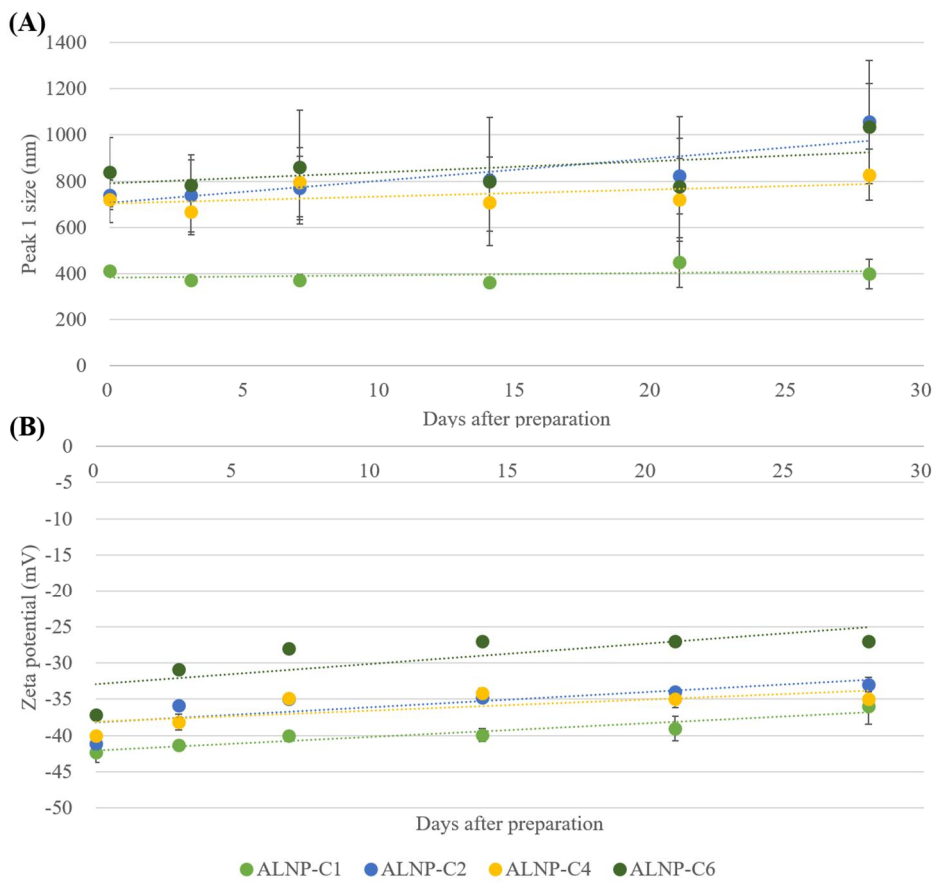
Figure 4-16. (A) Peak size and (B) zeta potential stability of ALNP-Cs in pure water as a function of time

3.5. *In vitro* cell viability

ALNPs exhibited relatively low cytotoxicity to A549 cell lines at concentrations of 25 and 50 μg mL^{-1} (Figure 4-17). Specifically, ALNP-C4 showed no significant biocompatibility in all concentrations that were tested (Figure 4-17A). However, KLNP-F1 represented a decreasing trend of biocompatibility as a function of concentration (Figure 4-17B). At a concentration of 250 μg mL^{-1}, cell viability severely decreased within 24 h and nearly completely dead within 72 h. On the other hand, the antiproliferation effect of ALNP-F2 and F3 was insignificant (Figure 4-17C and D). Besides, A549 cell line culture has more flourished in the presence of ALNP-F2 and F3 compared to in the presence of ALNP-C4.

Similar trends of cell cytotoxicity in the case of LLC was obtained. ALNPs, except for ALNP-F1 at higher concentrations (100 and 250 μg mL^{-1}), showed extremely low cytotoxicity to A549 cell lines at all concentrations tested (Figure 4-18). ALNP-F2 and F3 had no cytotoxic effect even at high concentrations (Figure 4-18C and D). The cell proliferation effect of ALNP-F2 and F3 was lower but comparable to the positive control (data not shown). Therefore, it was examined that the high biocompatibility of ALNPs and the potential of AL as a source of the drug delivery system.
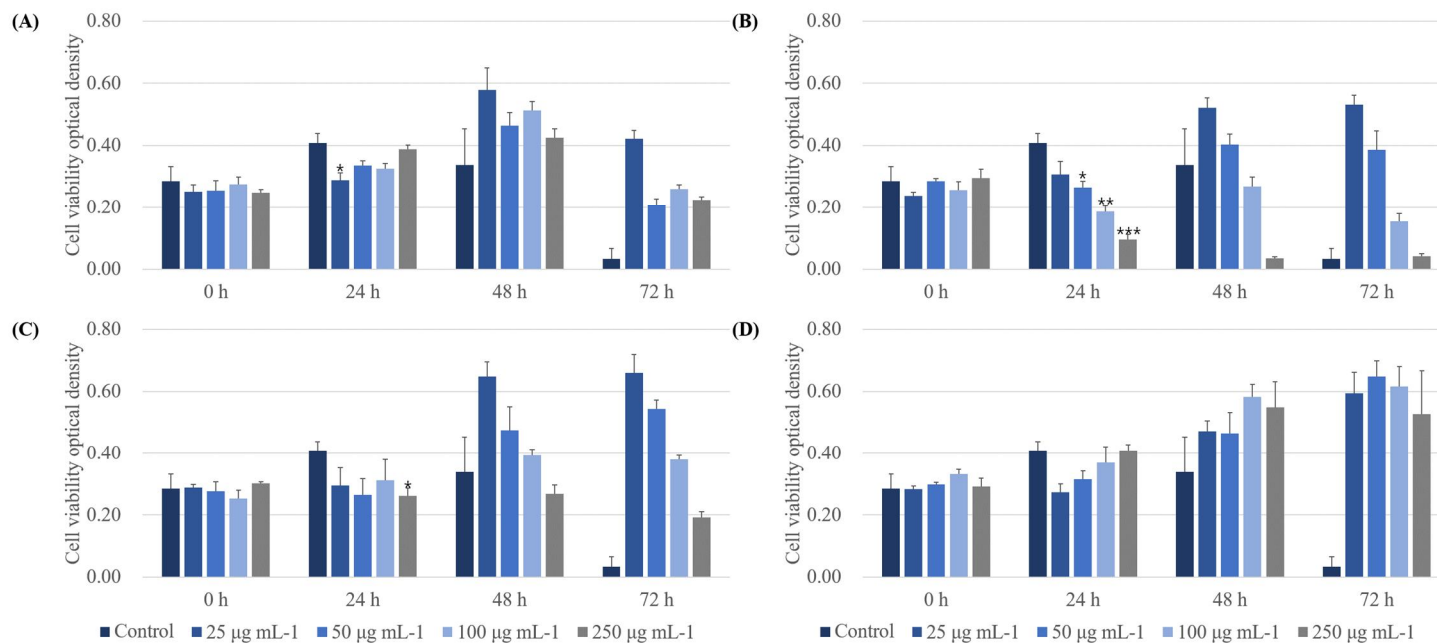
Figure 4-17. Cytotoxic effect of ALNPs on A549 cells. (A) ALNP-C4, (B) ALNP-F1, (C) ALNP-F2, and (D) ALNP-F3. The viability was determined by the Cell Counting Kit-8 assay, and all data sets were compared to the blank control (serum-free DMEM containing 1% of Antibiotic-Antimycotic). The data are presented as the mean ± standard deviation of three independent experiments. The level of the significant differences was set at probabilities of $*p < 0.05$, $**p < 0.01$, and $***p < 0.001$.
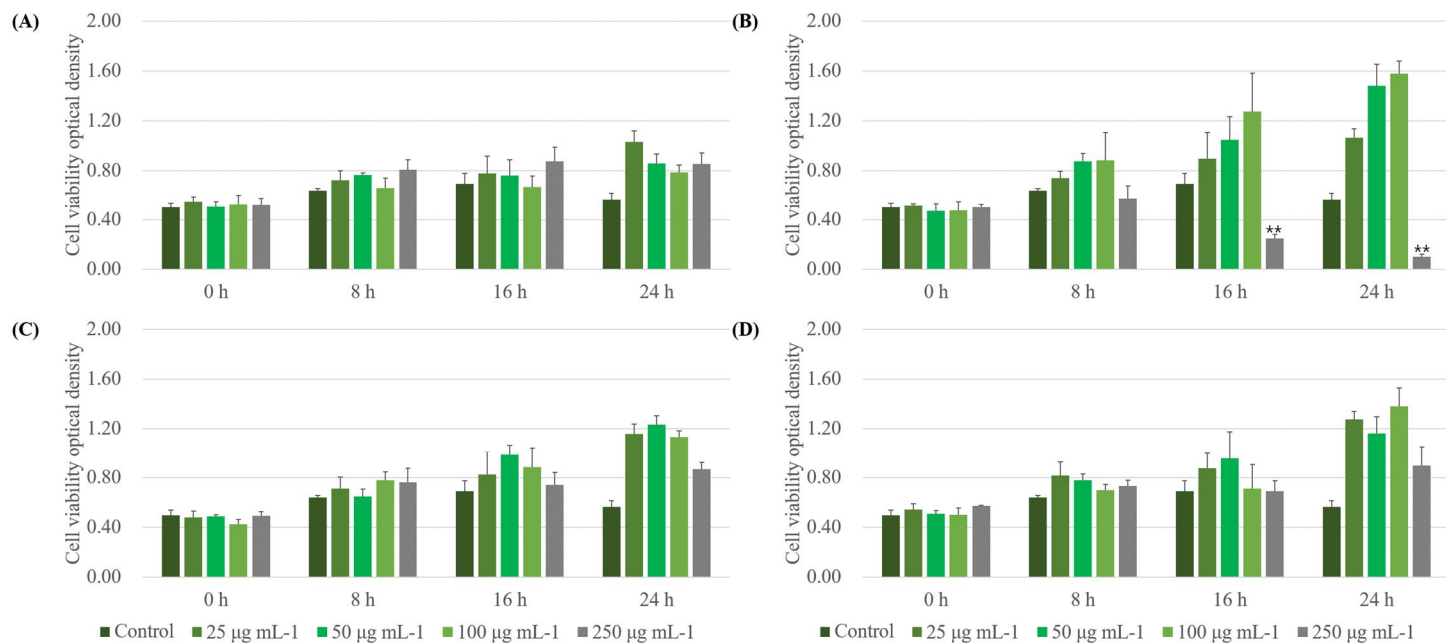
Figure 4-18. Cytotoxic effect of ALNPs on LLC cells. (A) ALNP-C4, (B) ALNP-F1, (C) ALNP-F2, and (D) ALNP-F3. The viability was determined by the Cell Counting Kit-8 assay, and all data sets were compared to the blank control (serum-free DMEM containing 1% of Antibiotic-Antimycotic). The data are presented as the mean ± standard deviation of three independent experiments. The level of the significant differences was set at probabilities of $*p < 0.05$, $**p < 0.01$, and $***p < 0.001$.

4. Conclusion

In this study, both sequential solvent extraction and chemoselective methylation of AL to block its phenolic hydroxyl group were performed to obtain fractions with different molecular weights and structures or decrease the amount of the specific functional group. The modified lignin was then handled to synthesize nano-sized pure lignin particles. Comprehensive analysis indicated that the lignin fractions with small molecular weight contained a higher total amount of functional groups and condensed structures. Also, ALNPs from the low-molecular-weight AL fractions had an enlarged size as previously concerned in chapter 2. The experiments using methylated lignin to clarify the effect of the phenolic hydroxyl group on the size increase of ALNPs revealed a high correlation between phenolic hydroxyl group content and size of the lignin nanoparticle. Every particle showed comparable and good colloidal stability while there was a large size difference between each ALNP. *In vitro* cell viability tests examined that ALNPs had very low cytotoxicity, except ALNP-F1 at high colloidal concentrations, which encourages the potential use of ALNPs as a drug delivery system.

Since it was determined that lignin nanoparticle size could be controlled by blocking specific functional groups and decreasing the interaction between hydroxyl groups, further application of lignin-based nanoparticle with the ideal size is expected. Particle size-reduction for drug-encapsulated nanoparticle and increasing the size would be appropriate for another industrial use such as UV-blocker, anode material, absorbent, or biocidal material.

Chapter 5

Conclusion

Lignin is the second most abundant natural polymer, composed of three different C6C3-type monomers with various interunit linkages. The value-addition of lignin is still challenging in the integrated lignocellulosic biorefinery due to its structural recalcitrance. Thus, various lignin valorization concepts have been investigated to date, but all these lignin uses require proper conversion processes. For this reason, fundamental studies to reveal structural features of the lignin and conversion process must be conducted. On the other hand, an investigation to provide high-value to lignin as a material for drug delivery has been recently carried out. A polymeric nanoparticle is the promising encapsulation structure for intravenous drug delivery since the release control by nanostructures has several advantages, such as reducing drug side effects by decreasing exposure to normal cells. In particular, due to its biocompatibility and abundance, lignin is a promising material for preparing the drug-encapsulated nanoparticle.

This study aimed to synthesize technical lignin-based nanoparticle for utilization as *in vivo* drug delivery. LignoBoost kraft lignin (KL) was chosen as a source of sequential solvent extraction, followed by an in-depth analysis of its characteristics (molecular weights, functional groups, and internal linkages). Then, the effect of structural features of lignin on the formation of the drug-encapsulated nanoparticle was determined. Both *in vitro* and *in vivo* experiments were performed to prove the biocompatibility, drug-encapsulating and releasing efficiency, and enhancement of drug efficacy of the lignin nanoparticle. Alkaline/soda lignin (AL) was also fractionated by solvent extraction or chemoselectively blocked to extensively determine the effect of lignin characteristics on the properties, especially the nanoparticle's size.

Several fractions with different molecular weights and structures were obtained by sequential solvent extraction of KL. The comprehensive analysis revealed that the lignin fractions obtained in the earlier stages of the solvent extraction had low molecular weight, a higher total amount of hydroxyl and methoxyl groups, and condensed structures compared to fractions from the late

stages. KL-derived nanoparticles (KLNPs) from each KL fractions formed by nanoprecipitation showed spherical shape with varied particle sizes (i.d. 193~1,039 nm), distributions, and relatively stable zeta potential values (-29.1~-44.5 mV). In contrast to the low-molecular-weight fraction-derived ones, high-molecular-weight-derived KLNPs exhibited weak bimodal or trimodal patterns of size peak distribution, which forced determining the correlation between particle size and lignin properties difficult. It was determined that some of the lignin properties, including molecular weight, hydroxyl group content, especially phenolic and carboxylic acids, are correlated with the particle size. Still, there was an agreement in the opinion that well-designed additional experiments are required to prove the matter of lignin properties and particle size. Determination of cell cytotoxicity and hemotoxicity of KLNPs showed high biocompatibility, or even possibly cell proliferation effect, *in vitro*. Findings from this study were then employed to synthesize drug-encapsulated forms of KLNPs,

Synthesis of a drug-encapsulated lignin nanoparticle (ELNP) was performed using KL as a polymer source, coumarin 6 as a drug model compound, and doxorubicin (DOX) as a chemotherapeutic drug. Both coumarin 6-encapsulated lignin nanoparticle (CELNP) and DOX-encapsulated lignin nanoparticle (DELNP) were successfully formed. The average sizes and drug encapsulation efficiency (EE) of CELNPs (i.d. 176~469 nm and 39~59 %, respectively) and DELNPs (i.d. 327~433 nm and 64~73 %, respectively) showed that the particle size does not significantly change compared to drug-free KLNP without regard to the addition of drug compounds. Also, the formation of CELNP using ethyl acetate-dissolved KL fraction (CELNP-F1) showed that EE did not increase but decreased by increasing the particle size since the size of the drug core are possibly not changed during the nanoprecipitation process. The drug release of CELNPs and DELNPs was rapidly performed within the initial stage (0~4 h) followed by a slow-release at both pH 5.5 and 7.4, which would be suitable for short-sustained releasing hydrophobic drugs. *In vitro* cytotoxicity and hemotoxicity tests supported the

ability of DELNPs to reduce side effects and red blood cell degradation of DOX. DELNP exhibited comparable antitumor efficacy to the same amount of free DOX, but the side effect was significantly reduced. As a result, DELNP exhibited advantages for biomedical applications (very good hemocompatibility, low allergenic properties, high colloidal stability, hydrophobic drug loading efficiency, release profile, and reduction of adverse effect).

On the other hand, to reveal the effect of lignin properties on the nanoparticle, synthesis of both AL fraction-derived (ALNP-F) and methylated AL-derived nanoparticle (ALNP-M) was carried out. Especially, the size of ALNP-Ms decreased (from 721 nm to 516 nm) by decreasing phenolic hydroxyl group content. The correlations between particle size and hydroxyl groups of the ALNP-Ms are presented as very high (R^2 = 0.95 for phenolic hydroxyl group). Consequently, it is assumed that the phenolic hydroxyl groups in lignin are the main properties that affect the nucleation and/or condensation during the nanoprecipitation process. In addition, the higher phenolic hydroxyl group content encourages the synthesis of lignin nanoparticles with a unimodal pattern of size distribution. ALNP showed extremely low cytotoxicity except for ALNP-F1 at high concentrations of 100 and 250 μg mL^{-1}.

This study investigated the effects of lignin molecular structural properties on synthesizing the drug-encapsulated lignin nanoparticle and its physicochemical characteristics. The potential uses of technical lignin as sources of nanotechnology-enabled drug delivery systems were introduced based on these results. Although more research is required to in-depth understand the properties of lignin as a polymer material and to enhance the drug-releasing strategies by further functionalization, these results proposed that the lignin-based nano-drug delivery system has the future prospects for their high-value application in a low-carbon economy.

<u>References</u>

Aggarwal, S. 2010. Targeted cancer therapies. *Nature Reviews Drug Discovery*, **9**(6), 427-8.

Ameller, T., Marsaud, V., Legrand, P., Gref, R., Renoir, J.M. 2003. In vitro and in vivo biologic evaluation of long-circulating biodegradable drug carriers loaded with the pure antiestrogen RU 58668. *International Journal of Cancer*, **106**(3), 446-54.

Amin, K., Dannenfelser, R.M. 2006. In vitro hemolysis: guidance for the pharmaceutical scientist. *Journal of Pharmaceutical Sciences*, **95**(6), 1173-6.

An, L., Wang, G., Jia, H., Liu, C., Sui, W., Si, C. 2017. Fractionation of enzymatic hydrolysis lignin by sequential extraction for enhancing antioxidant performance. *International Journal of Biological Macromolecules*, **99**, 674-681.

Anwar, Z., Gulfraz, M., Irshad, M. 2014. Agro-industrial lignocellulosic biomass a key to unlock the future bio-energy: a brief review. *Journal of Radiation Research & Applied Sciences*, **7**(2), 163-173.

Araujo, L.C.P., Yamaji, F.M., Lima, V.H., Botaro, V.R. 2020. Kraft lignin fractionation by organic solvents: Correlation between molar mass and higher heating value. *Bioresource Technology*, **314**, 123757.

Arayachukeat, S., Wanichwecharungruang, S.P., Tree-Udom, T. 2011. Retinyl acetate-loaded nanoparticles: dermal penetration and release of the retinyl acetate. *International Journal of Pharmaceutics*, **404**(1-2), 281-288.

Aro, T., Fatehi, P. 2017. Production and Application of Lignosulfonates and Sulfonated Lignin. *ChemSusChem*, **10**(9), 1861-1877.

Axegård, P., STFI-Packforsk, A. 2007. The kraft pulp mill as a biorefinery. *Division Fiber, Pulp Energy and Chemicals. STFI-Packforsk PO Box*, **5604**, 1-6.

Azouz, S.M., Walpole, J., Amirifeli, S., Taylor, K.N., Grinstaff, M.W., Colson, Y.L. 2008. Prevention of local tumor growth with paclitaxel-loaded

microspheres. *The Journal of Thoracic and Cardiovascular Surgery*, **135**(5), 1014-21.

Babu, A., Amreddy, N., Muralidharan, R., Pathuri, G., Gali, H., Chen, A., Zhao, Y.D., Munshi, A., Ramesh, R. 2017. Chemodrug delivery using integrin-targeted PLGA-Chitosan nanoparticle for lung cancer therapy. *Scientific Reports*, **7**(1), 1-17.

Badri, W., Miladi, K., Nazari, Q.A., Fessi, H., Elaissari, A. 2017. Effect of process and formulation parameters on polycaprolactone nanoparticles prepared by solvent displacement. *Colloids and Surfaces A: Physicochemical and Engineering Aspects*, **516**, 238-244.

Baker, S.M. 1996. Rapid methoxyl analysis of lignins using gas chromatography. *Holzforschung*, **50**, 573-574.

Barton, A.F. 2017. *CRC handbook of solubility parameters and other cohesion parameters*. Routledge.

Barton, A.F. 1991. *CRC handbook of solubility parameters and other cohesion parameters*. CRC press.

Beckham, G.T., Bozell, J., Houtman, C., Felby, C., Rinaldi, R., Zhang, X., Bruijnincx, P., Martinez, A., Masai, E., Neidle, E. 2018. *Lignin Valorization: Emerging Approaches*. Royal Society of Chemistry.

Beg, S., Rizwan, M., Sheikh, A.M., Hasnain, M.S., Anwer, K., Kohli, K. 2011. Advancement in carbon nanotubes: basics, biomedical applications and toxicity. *Journal of Pharmacy and Pharmacology*, **63**(2), 141-63.

Bezuidenhout, M.B., van Staden, A.D., Oosthuizen, G.A., Dimitrov, D.M., Dicks, L.M. 2015. Delivery of antibiotics from cementless titanium-alloy cubes may be a novel way to control postoperative infections. *BioMed Research International*, **2015**.

Bianco, A., Kostarelos, K., Prato, M. 2005. Applications of carbon nanotubes in drug delivery. *Current Opinion in Chemical Biology*, **9**(6), 674-679.

Bilati, U., Allemann, E., Doelker, E. 2005. Development of a nanoprecipitation

method intended for the entrapment of hydrophilic drugs into nanoparticles. *European Journal of Pharmaceutical Sciences*, **24**(1), 67-75.

Biswas, S., Dodwadkar, N.S., Sawant, R.R., Torchilin, V.P. 2011. Development of the novel PEG-PE-based polymer for the reversible attachment of specific ligands to liposomes: synthesis and in vitro characterization. *Bioconjugate Chemistry*, **22**(10), 2005-13.

Björkman, A. 1954. Isolation of lignin from finely divided wood with neutral solvents. *Nature*, **174**(4440), 1057-1058.

Bobo, D., Robinson, K.J., Islam, J., Thurecht, K.J., Corrie, S.R. 2016. Nanoparticle-Based Medicines: A Review of FDA-Approved Materials and Clinical Trials to Date. *Pharmaceutical Research*, **33**(10), 2373-87.

Boehm, A.-L.L.R., Zerrouk, R., Fessi, H. 2000. Poly epsilon-caprolactone nanoparticles containing a poorly soluble pesticide: formulation and stability study. *Journal of Microencapsulation*, **17**(2), 195-205.

Boeriu, C.G., Fiţigău, F.I., Gosselink, R.J., Frissen, A.E., Stoutjesdijk, J., Peter, F. 2014. Fractionation of five technical lignins by selective extraction in green solvents and characterisation of isolated fractions. *Industrial Crops & Products*, **62**, 481-490.

Brittain, H.G. 2013. *Profiles of drug substances, excipients, and related methodology*. Academic Press.

Bruschi, M.L. 2015. *Strategies to modify the drug release from pharmaceutical systems*. Woodhead Publishing.

Butun, S., Ince, F.G., Erdugan, H., Sahiner, N. 2011. One-step fabrication of biocompatible carboxymethyl cellulose polymeric particles for drug delivery systems. *Carbohydrate Polymers*, **86**(2), 636-643.

Calderón, L., Harris, R., Cordoba-Diaz, M., Elorza, M., Elorza, B., Lenoir, J., Adriaens, E., Remon, J., Heras, A., Cordoba-Diaz, D. 2013. Nano and microparticulate chitosan-based systems for antiviral topical delivery.

European Journal of Pharmaceutical Sciences, **48**(1-2), 216-222.

Calvo-Flores, F.G., Dobado, J.A., Isac-García, J., Martín-Martínez, F.J. 2015. *Lignin and lignans as renewable raw materials: chemistry, technology and applications*. John Wiley & Sons.

Caputo, F., Clogston, J., Calzolai, L., Rösslein, M., Prina-Mello, A. 2019. Measuring particle size distribution of nanoparticle enabled medicinal products, the joint view of EUNCL and NCI-NCL. A step by step approach combining orthogonal measurements with increasing complexity. *Journal of Controlled Release*, **299**, 31-43.

Cavdar, A.D., Kalaycioglu, H., Hiziroglu, S. 2008. Some of the properties of oriented strandboard manufactured using kraft lignin phenolic resin. *Journal of Materials Processing Technology*, **202**(1-3), 559-563.

Chen, L., Zhou, X., Shi, Y., Gao, B., Wu, J., Kirk, T.B., Xu, J., Xue, W. 2018. Green synthesis of lignin nanoparticle in aqueous hydrotropic solution toward broadening the window for its processing and application. *Chemical Engineering Journal*, **346**, 217-225.

Chen, N., Dempere, L.A., Tong, Z. 2016. Synthesis of pH-responsive lignin-based nanocapsules for controlled release of hydrophobic molecules. *ACS Sustainable Chemistry & Engineering*, **4**(10), 5204-5211.

Chin, S.F., Jimmy, F.B., Pang, S.C. 2018. Size controlled fabrication of cellulose nanoparticles for drug delivery applications. *Journal of Drug Delivery Science & Technology*, **43**, 262-266.

Chorny, M., Fishbein, I., Danenberg, H.D., Golomb, G. 2002. Lipophilic drug loaded nanospheres prepared by nanoprecipitation: effect of formulation variables on size, drug recovery and release kinetics. *Journal of Controlled Release*, **83**(3), 389-400.

Clogston, J.D., Patri, A.K. 2011. Zeta potential measurement. in: *Characterization of nanoparticles intended for drug delivery*, Springer, pp. 63-70.

Corrie, P.G. 2008. Cytotoxic chemotherapy: clinical aspects. *Medicine*, **36**(1), 24-

28.

Couvreur, P. 2013. Nanoparticles in drug delivery: past, present and future. *Advanced Drug Delivery Reviews*, **65**(1), 21-23.

Crucho, C.I.C., Barros, M.T. 2017. Polymeric nanoparticles: A study on the preparation variables and characterization methods. *Materials Science and Engineering C: Materials for Biological Applications*, **80**, 771-784.

D'Addio, S.M., Prud'homme, R.K. 2011. Controlling drug nanoparticle formation by rapid precipitation. *Advanced Drug Delivery Reviews*, **63**(6), 417-26.

Dai, L., Liu, R., Hu, L.-Q., Zou, Z.-F., Si, C.-L. 2017. Lignin nanoparticle as a novel green carrier for the efficient delivery of resveratrol. *ACS Sustainable Chemistry & Engineering*, **5**(9), 8241-8249.

Dai, L., Si, C.-L. 2017. Cellulose-graft-poly (methyl methacrylate) nanoparticles with high biocompatibility for hydrophobic anti-cancer drug delivery. *Materials Letters*, **207**, 213-216.

de Haro, J.C., Allegretti, C., Smit, A.T., Turri, S., D'Arrigo, P., Griffini, G. 2019. Biobased polyurethane coatings with high biomass content: tailored properties by lignin selection. *ACS Sustainable Chemistry & Engineering*, **7**(13), 11700-11711.

Demirbas, A. 2007. Progress and recent trends in biofuels. *Progress in Energy & Combustion Science*, **33**(1), 1-18.

DeVita, V.T., Chu, E. 2008. A history of cancer chemotherapy. *Cancer Research*, **68**(21), 8643-8653.

Ding, R., Wu, H., Thunga, M., Bowler, N., Kessler, M.R. 2016. Processing and characterization of low-cost electrospun carbon fibers from organosolv lignin/polyacrylonitrile blends. *Carbon*, **100**, 126-136.

Dobrovolskaia, M.A., Clogston, J.D., Neun, B.W., Hall, J.B., Patri, A.K., McNeil, S.E. 2008. Method for analysis of nanoparticle hemolytic properties in vitro. *Nano Letters*, **8**(8), 2180-2187.

Domínguez-Robles, J., Tamminen, T., Liitiä, T., Peresin, M.S., Rodríguez, A.,

Jääskeläinen, A.-S. 2018. Aqueous acetone fractionation of kraft, organosolv and soda lignins. *International Journal of Biological Macromolecules*, **106**, 979-987.

Dong, Y., Feng, S.-S. 2004. Methoxy poly (ethylene glycol)-poly (lactide)(MPEG-PLA) nanoparticles for controlled delivery of anticancer drugs. *Biomaterials*, **25**(14), 2843-2849.

Du, X., Li, J., Lindström, M.E. 2014. Modification of industrial softwood kraft lignin using Mannich reaction with and without phenolation pretreatment. *Industrial Crops and Products*, **52**, 729-735.

Dumont, C., Gauvin, R.M., Belva, F., Sauthier, M. 2018. Palladium-Catalyzed Functionalization of Kraft Lignin: Ether Linkages through the Telomerization Reaction. *ChemSusChem*, **11**(10), 1649-1655.

Duval, A., Lange, H., Lawoko, M., Crestini, C. 2015a. Modification of Kraft lignin to expose diazobenzene groups: Toward pH-and light-responsive biobased polymers. *Biomacromolecules*, **16**(9), 2979-2989.

Duval, A., Lange, H., Lawoko, M., Crestini, C. 2015b. Reversible crosslinking of lignin via the furan–maleimide Diels–Alder reaction. *Green Chemistry*, **17**(11), 4991-5000.

El-Say, K.M., El-Sawy, H.S. 2017. Polymeric nanoparticles: Promising platform for drug delivery. *International Journal of Pharmaceutics*, **528**(1-2), 675-691.

Fairhurst, D. 2013. An overview of the zeta potential part 3: uses and applications. *American Pharmaceutical Review*.

Fang, Z., Smith Jr, R.L. 2016. *Production of biofuels and chemicals from lignin*. Springer.

Fenoy, G.E., Maza, E., Zelaya, E., Marmisollé, W.A., Azzaroni, O. 2017. Layer-by-layer assemblies of highly connected polyelectrolyte capped-Pt nanoparticles for electrocatalysis of hydrogen evolution reaction. *Applied Surface Science*, **416**, 24-32.

Fessi, H., Puisieux, F., Devissaguet, J.P., Ammoury, N., Benita, S. 1989. Nanocapsule formation by interfacial polymer deposition following solvent displacement. *International Journal of Pharmaceutics*, **55**(1), R1-R4.

Figueiredo, P., Lintinen, K., Kiriazis, A., Hynninen, V., Liu, Z., Bauleth-Ramos, T., Rahikkala, A., Correia, A., Kohout, T., Sarmento, B., Yli-Kauhaluoma, J., Hirvonen, J., Ikkala, O., Kostiainen, M.A., Santos, H.A. 2017. In vitro evaluation of biodegradable lignin-based nanoparticles for drug delivery and enhanced antiproliferation effect in cancer cells. *Biomaterials*, **121**, 97-108.

García-Mateos, F., Berenguer, R., Valero-Romero, M., Rodríguez-Mirasol, J., Cordero, T. 2018. Phosphorus functionalization for the rapid preparation of highly nanoporous submicron-diameter carbon fibers by electrospinning of lignin solutions. *Journal of Materials Chemistry A*, **6**(3), 1219-1233.

Garti, N. 1997. Double emulsions—scope, limitations and new achievements. *Colloids Surfaces A: Physicochemical and Engineering Aspects*, **123**, 233-246.

Gaumet, M., Vargas, A., Gurny, R., Delie, F.J.E.j.o.p. 2008. Nanoparticles for drug delivery: the need for precision in reporting particle size parameters. *European journal of pharmaceutics & biopharmaceutics*, **69**(1), 1-9.

Gillet, S., Aguedo, M., Petitjean, L., Morais, A., da Costa Lopes, A., Łukasik, R., Anastas, P. 2017. Lignin transformations for high value applications: towards targeted modifications using green chemistry. *Green Chemistry*, **19**(18), 4200-4233.

Glasser, W.G. 2019. About making lignin great again-some lessons from the past. *Frontiers in Chemistry*, **7**, 565.

Gómez-Fernández, S., Ugarte, L., Calvo-Correas, T., Peña-Rodríguez, C., Corcuera, M.A., Eceiza, A. 2017. Properties of flexible polyurethane

foams containing isocyanate functionalized kraft lignin. *Industrial Crops and Products*, **100**, 51-64.

Graglia, M., Pampel, J., Hantke, T., Fellinger, T.-P., Esposito, D. 2016. Nitro lignin-derived nitrogen-doped carbon as an efficient and sustainable electrocatalyst for oxygen reduction. *ACS Nano*, **10**(4), 4364-4371.

Gregorová, A., Košíková, B., Moravčík, R. 2006. Stabilization effect of lignin in natural rubber. *Polymer Degradation and Stability*, **91**(2), 229-233.

Hamaguchi, M., Cardoso, M., Vakkilainen, E. 2012. Alternative Technologies for Biofuels Production in Kraft Pulp Mills—Potential and Prospects. *Energies*, **5**(7), 2288-2309.

Hansen, C.M. 1967. The three dimensional solubility parameter. *Danish Technical: Copenhagen*, **14**.

Held, P. 2009. An absorbance-based cytotoxicity assay using high absorptivity, water-soluble tetrazolium salts. *Application Note. BioTek Instruments, INC., Winooski, Vermont*, **5404**.

Heurtault, B., Saulnier, P., Pech, B., Benoıt, J., Proust, J. 2003. Interfacial stability of lipid nanocapsules. *Colloids and Surfaces B: Biointerfaces*, **30**(3), 225-235.

Himmel, M.E., Ding, S.-Y., Johnson, D.K., Adney, W.S., Nimlos, M.R., Brady, J.W., Foust, T.D. 2007. Biomass recalcitrance: engineering plants and enzymes for biofuels production. *Science*, **315**(5813), 804-807.

Horie, M., Fujita, K. 2011. Toxicity of metal oxides nanoparticles. in: *Advances in molecular toxicology*, Vol. 5, Elsevier, pp. 145-178.

Hu, S., Hsieh, Y.-L. 2016. Silver nanoparticle synthesis using lignin as reducing and capping agents: A kinetic and mechanistic study. *International Journal of Biological Macromolecules*, **82**, 856-862.

Hua, S., Wu, S.Y. 2013. The use of lipid-based nanocarriers for targeted pain therapies. *Frontiers in Pharmacology*, **4**, 143.

Hunter, R.J. 2013. *Zeta potential in colloid science: principles and applications*.

Academic press.

Hyam, R.S., Subhedar, K.M., Pawar, S.H. 2008. Effect of particle size distribution and zeta potential on the electrophoretic deposition of boron films. *Colloids and Surfaces A: Physicochemical and Engineering Aspects*, **315**(1-3), 61-65.

Ibrahim, M.N.M., Zakaria, N., Sipaut, C.S., Sulaiman, O., Hashim, R. 2011. Chemical and thermal properties of lignins from oil palm biomass as a substitute for phenol in a phenol formaldehyde resin production. *Carbohydrate Polymers*, **86**(1), 112-119.

Idrees, H., Zaidi, S.Z.J., Sabir, A., Khan, R.U., Zhang, X., Hassan, S.-u. 2020. A Review of Biodegradable Natural Polymer-Based Nanoparticles for Drug Delivery Applications. *Nanomaterials*, **10**(10), 1970.

Jensen, M.O., Mouritsen, O.G., Peters, G.H. 2004. The hydrophobic effect: molecular dynamics simulations of water confined between extended hydrophobic and hydrophilic surfaces. *The Journal of Chemical Physics*, **120**(20), 9729-44.

Jiang, C., He, H., Jiang, H., Ma, L., Jia, D. 2013. Nano-lignin filled natural rubber composites: Preparation and characterization. *Express Polymer Letters*, **7**(5).

Jiang, X., Savithri, D., Du, X., Pawar, S., Jameel, H., Chang, H.-m., Zhou, X. 2017. Fractionation and characterization of kraft lignin by sequential precipitation with various organic solvents. *ACS Sustainable Chemistry & Engineering*, **5**(1), 835-842.

Jiao, G.-J., Xu, Q., Cao, S.-L., Peng, P., She, D. 2018. Controlled-release fertilizer with lignin used to trap urea/hydroxymethylurea/urea-formaldehyde polymers. *BioResources*, **13**(1), 1711-1728.

Johansson, A., Aaltonen, O., Ylinen, P. 1987. Organosolv pulping—methods and pulp properties. *Biomass*, **13**(1), 45-65.

Kadla, J., Kubo, S., Venditti, R., Gilbert, R., Compere, A., Griffith, W. 2002.

Lignin-based carbon fibers for composite fiber applications. *Carbon*, **40**(15), 2913-2920.

Kai, D., Chong, H.M., Chow, L.P., Jiang, L., Lin, Q., Zhang, K., Zhang, H., Zhang, Z., Loh, X.J. 2018. Strong and biocompatible lignin/poly (3-hydroxybutyrate) composite nanofibers. *Composites Science Technology*, **158**, 26-33.

Kim, D., Lee, E.S., Oh, K.T., Gao, Z.G., Bae, Y.H. 2008. Doxorubicin-loaded polymeric micelle overcomes multidrug resistance of cancer by double-targeting folate receptor and early endosomal pH. *Small*, **4**(11), 2043-2050.

Kim, J.-Y., Heo, S., Choi, J.W. 2018. Effects of phenolic hydroxyl functionality on lignin pyrolysis over zeolite catalyst. *Fuel*, **232**, 81-89.

Kim, J.-Y., Johnston, P.A., Lee, J.H., Smith, R.G., Brown, R.C. 2019. Improving Lignin Homogeneity and Functionality via Ethanolysis for Production of Antioxidants. *ACS Sustainable Chemistry & Engineering*, **7**(3), 3520-3526.

Kim, J.-Y., Lee, J.H., Park, J., Kim, J.K., An, D., Song, I.K., Choi, J.W. 2015. Catalytic pyrolysis of lignin over HZSM-5 catalysts: Effect of various parameters on the production of aromatic hydrocarbon. *Journal of Analytical and Applied Pyrolysis*, **114**, 273-280.

Kim, J.-Y., Oh, S., Hwang, H., Kim, U.-J., Choi, J.W. 2013. Structural features and thermal degradation properties of various lignin macromolecules obtained from poplar wood (Populus albaglandulosa). *Polymer Degradation and Stability*, **98**(9), 1671-1678.

Kim, J.-Y., Park, S.Y., Lee, J.H., Choi, I.-G., Choi, J.W. 2017. Sequential solvent fractionation of lignin for selective production of monoaromatics by Ru catalyzed ethanolysis. *RSC Advances*, **7**(84), 53117-53125.

Koivu, K.A., Sadeghifar, H., Nousiainen, P.A., Argyropoulos, D.S., Sipilä, J. 2016. Effect of fatty acid esterification on the thermal properties of softwood kraft lignin. *ACS Sustainable Chemistry & Engineering*, **4**(10), 5238-5247.

Korsmeyer, R., Peppas, N. 1983. Macromolecular and modeling aspects of swelling-controlled systems. *Controlled Release Delivery Systems*, **1983**(77-90), 83.

Krall, E.M., Serum, E.M., Sibi, M.P., Webster, D.C. 2018. Catalyst-free lignin valorization by acetoacetylation. Structural elucidation by comparison with model compounds. *Green Chemistry*, **20**(13), 2959-2966.

Kumar, A., Dixit, C.K. 2017. Methods for characterization of nanoparticles. in: *Advances in Nanomedicine for the Delivery of Therapeutic Nucleic Acids*, Elsevier, pp. 43-58.

Kundranda, M.N., Henderson, M., Carter, K.J., Gorden, L., Binhazim, A., Ray, S., Baptiste, T., Shokrani, M., Leite-Browning, M.L., Jahnen-Dechent, W. 2005. The serum glycoprotein fetuin-A promotes Lewis lung carcinoma tumorigenesis via adhesive-dependent and adhesive-independent mechanisms. *Cancer Research*, **65**(2), 499-506.

Larrañeta, E., Imízcoz, M., Toh, J.X., Irwin, N.J., Ripolin, A., Perminova, A., Domínguez-Robles, J., Rodríguez, A., Donnelly, R.F. 2018. Synthesis and characterization of lignin hydrogels for potential applications as drug eluting antimicrobial coatings for medical materials. *ACS Sustainable Chemistry & Engineering*, **6**(7), 9037-9046.

Lassalle, V., Ferreira, M.L. 2007. PLA nano-and microparticles for drug delivery: an overview of the methods of preparation. *Macromolecular Bioscience*, **7**(6), 767-783.

Lee, J., Kim, J., Lee, Y.M., Park, D., Im, S., Song, E.H., Park, H., Kim, W.J. 2017. Self-assembled nanocomplex between polymerized phenylboronic acid and doxorubicin for efficient tumor-targeted chemotherapy. *Acta Pharmacologica Sinica*, **38**(6), 848-858.

Lee, J.H., Ahmed, M.A., Choi, I.-G., Choi, J.W. 2020. Fractionation of Cellulose-Rich Products from an Empty Fruit Bunch (EFB) by Means of Steam Explosion Followed by Organosolv Treatment. *Applied Sciences*, **10**(3).

Letchford, K., Burt, H. 2007. A review of the formation and classification of amphiphilic block copolymer nanoparticulate structures: micelles, nanospheres, nanocapsules and polymersomes. *European Journal of Pharmaceutics and Biopharmaceutics*, **65**(3), 259-69.

Lewinski, N., Colvin, V., Drezek, R. 2008. Cytotoxicity of nanoparticles. *Small*, **4**(1), 26-49.

Li, C., Wang, J., Wang, Y., Gao, H., Wei, G., Huang, Y., Yu, H., Gan, Y., Wang, Y., Mei, L. 2019. Recent progress in drug delivery. *Acta Pharmaceutica Sinica B*, **9**(6), 1145-1162.

Li, J., Wang, M., She, D., Zhao, Y. 2017. Structural functionalization of industrial softwood kraft lignin for simple dip-coating of urea as highly efficient nitrogen fertilizer. *Industrial Crops and Products*, **109**, 255-265.

Li, R.J., Gutierrez, J., Chung, Y.-L., Frank, C.W., Billington, S.L., Sattely, E.S. 2018. A lignin-epoxy resin derived from biomass as an alternative to formaldehyde-based wood adhesives. *Green Chemistry*, **20**(7), 1459-1466.

Li, S., Lundquist, K. 1994. A new method for the analysis of phenolic groups in lignins by 1H NMR spectroscopy. *Nordic Pulp Paper Research Journal*, **9**(3), 191-195.

Li, W.-M., Su, C.-W., Chen, Y.-W., Chen, S.-Y. 2015. In situ DOX-calcium phosphate mineralized CPT-amphiphilic gelatin nanoparticle for intracellular controlled sequential release of multiple drugs. *Acta Biomaterialia*, **15**, 191-199.

Lievonen, M., Valle-Delgado, J.J., Mattinen, M.-L., Hult, E.-L., Lintinen, K., Kostiainen, M.A., Paananen, A., Szilvay, G.R., Setälä, H., Österberg, M. 2016. A simple process for lignin nanoparticle preparation. *Green Chemistry*, **18**(5), 1416-1422.

Limayem Blouza, I., Charcosset, C., Sfar, S., Fessi, H. 2006. Preparation and characterization of spironolactone-loaded nanocapsules for paediatric use. *International Journal of Pharmaceutics*, **325**(1-2), 124-31.

Lince, F., Marchisio, D.L., Barresi, A.A. 2008. Strategies to control the particle size distribution of poly-ε-caprolactone nanoparticles for pharmaceutical applications. *Journal of Colloid and Interface Science*, **322**(2), 505-515.

Liu, L.-Y., Hua, Q., Renneckar, S. 2019. A simple route to synthesize esterified lignin derivatives. *Green Chemistry*, **21**(13), 3682-3692.

Liu, Y., Yang, J., Zhao, Z., Li, J., Zhang, R., Yao, F. 2012. Formation and characterization of natural polysaccharide hollow nanocapsules via template layer-by-layer self-assembly. *Journal of Colloid and Interface Science*, **379**(1), 130-140.

Llevot, A., Monney, B., Sehlinger, A., Behrens, S., Meier, M. 2017. Highly efficient Tsuji–Trost allylation in water catalyzed by Pd-nanoparticles. *Chemical Communications*, **53**(37), 5175-5178.

Lora, J. 2008. Industrial commercial lignins: sources, properties and applications. in: *Monomers, polymers and composites from renewable resources*, Elsevier, pp. 225-241.

Lu, F., Ralph, J. 1997. DFRC method for lignin analysis. 1. New method for β-aryl ether cleavage: lignin model studies. *Journal of Agricultural Food Chemistry*, **45**(12), 4655-4660.

Ma, M., Dai, L., Xu, J., Liu, Z., Ni, Y. 2020. A simple and effective approach to fabricate lignin nanoparticles with tunable sizes based on lignin fractionation. *Green Chemistry*, **22**(6), 2011-2017.

Mahata, D., Jana, M., Jana, A., Mukherjee, A., Mondal, N., Saha, T., Sen, S., Nando, G.B., Mukhopadhyay, C.K., Chakraborty, R. 2017. Lignin-graft-polyoxazoline conjugated triazole a novel anti-infective ointment to control persistent inflammation. *Scientific Reports*, **7**, 46412.

Martinez Rivas, C.J., Tarhini, M., Badri, W., Miladi, K., Greige-Gerges, H., Nazari, Q.A., Galindo Rodriguez, S.A., Roman, R.A., Fessi, H., Elaissari, A. 2017. Nanoprecipitation process: From encapsulation to drug delivery. *International Journal of Pharmaceutics*, **532**(1), 66-81.

Mendis, G.P., Hua, I., Youngblood, J.P., Howarter, J.A. 2015. Enhanced dispersion of lignin in epoxy composites through hydration and mannich functionalization. *Journal of Applied Polymer Science*, **132**(1).

Mina, M., Puzyk, I., Puzyk, M. 2013. The effect of acids on fluorescence of coumarin-6 in organic solvents. *Optics & Spectroscopy*, **114**(2), 244-246.

Mora-Huertas, C.E., Fessi, H., Elaissari, A. 2010. Polymer-based nanocapsules for drug delivery. *International Journal of Pharmaceutics*, **385**(1-2), 113-42.

Nittayacharn, P., Abenojar, E., De Leon, A., Wegierak, D., Exner, A.A. 2020. Increasing Doxorubicin Loading in Lipid-Shelled Perfluoropropane Nanobubbles via a Simple Deprotonation Strategy. *Frontiers in Pharmacology*, **11**, 644.

Pang, T., Wang, G., Sun, H., Wang, L., Liu, Q., Sui, W., Parvez, A.M., Si, C. 2020. Lignin Fractionation for Reduced Heterogeneity in Self-Assembly Nanosizing: Toward Targeted Preparation of Uniform Lignin Nanoparticles with Small Size. *ACS Sustainable Chemistry & Engineering*, **8**(24), 9174-9183.

Pang, Y., Wang, S., Qiu, X., Luo, Y., Lou, H., Huang, J. 2017. Preparation of lignin/sodium dodecyl sulfate composite nanoparticles and their application in pickering emulsion template-based microencapsulation. *Journal of Agricultural & Food Chemistry*, **65**(50), 11011-11019.

Panyam, J., Labhasetwar, V. 2003. Biodegradable nanoparticles for drug and gene delivery to cells and tissue. *Advanced Drug Delivery Reviews*, **55**(3), 329-347.

Park, H.-K., Kang, M.-G., Yang, M.-S., Jung, J.-W., Cho, S.-H., Kang, H.-R. 2017. Epidemiology of drug-induced anaphylaxis in a tertiary hospital in Korea. *Allergology International*, **66**(4), 557-562.

Park, J., Hwang, H., Kim, J.Y., Choi, J.W. 2018a. Applicability of lignin polymers for automobile brake pads as binder and filler materials and their performance characteristics. *Environmental Technology*, 1-10.

Park, S.Y., Kim, J.-Y., Youn, H.J., Choi, J.W. 2018b. Fractionation of lignin macromolecules by sequential organic solvents systems and their characterization for further valuable applications. *International Journal of Biological Macromolecules*, **106**, 793-802.

Patra, J.K., Das, G., Fraceto, L.F., Campos, E.V.R., Rodriguez-Torres, M.D.P., Acosta-Torres, L.S., Diaz-Torres, L.A., Grillo, R., Swamy, M.K., Sharma, S., Habtemariam, S., Shin, H.S. 2018. Nano based drug delivery systems: recent developments and future prospects. *Journal of Nanobiotechnology*, **16**(1), 71.

Prego, C., Garcia, M., Torres, D., Alonso, M. 2005. Transmucosal macromolecular drug delivery. *Journal of Controlled Release*, **101**(1-3), 151-162.

Pu, Y., Cao, S., Ragauskas, A.J. 2011. Application of quantitative 31P NMR in biomass lignin and biofuel precursors characterization. *Energy & Environmental Science*, **4**(9), 3154-3166.

Quintanar-Guerrero, D., Allémann, E., Doelker, E., Fessi, H. 1998. Preparation and characterization of nanocapsules from preformed polymers by a new process based on emulsification-diffusion technique. *Pharmaceutical Research*, **15**(7), 1056-1062.

Ragauskas, A.J., Beckham, G.T., Biddy, M.J., Chandra, R., Chen, F., Davis, M.F., Davison, B.H., Dixon, R.A., Gilna, P., Keller, M. 2014. Lignin valorization: improving lignin processing in the biorefinery. *Science*, **344**(6185), 1246843.

Ragauskas, A.J., Nagy, M., Kim, D.H., Eckert, C.A., Hallett, J.P., Liotta, C.L. 2006. From wood to fuels: integrating biofuels and pulp production. *Industrial Biotechnology*, **2**(1), 55-65.

Rashid, M.u., Coombs, K.M. 2019. Serum-reduced media impacts on cell viability and protein expression in human lung epithelial cells. *Journal of Cellular Physiology*, **234**(6), 7718-7724.

Rawal, T., Parmar, R., Tyagi, R.K., Butani, S. 2017. Rifampicin loaded chitosan

nanoparticle dry powder presents an improved therapeutic approach for alveolar tuberculosis. *Colloids & Surfaces B: Biointerfaces*, **154**, 321-330.

Rinaldi, R., Jastrzebski, R., Clough, M.T., Ralph, J., Kennema, M., Bruijnincx, P.C., Weckhuysen, B.M. 2016. Paving the Way for Lignin Valorisation: Recent Advances in Bioengineering, Biorefining and Catalysis. *Angewandte Chemie International Edition in English*, **55**(29), 8164-215.

Saito, T., Perkins, J.H., Jackson, D.C., Trammel, N.E., Hunt, M.A., Naskar, A.K. 2013. Development of lignin-based polyurethane thermoplastics. *RSC Advances*, **3**(44), 21832-21840.

Saito, T., Perkins, J.H., Vautard, F., Meyer, H.M., Messman, J.M., Tolnai, B., Naskar, A.K. 2014. Methanol fractionation of softwood kraft lignin: Impact on the lignin properties. *ChemSusChem*, **7**(1), 221-228.

Salentinig, S., Schubert, M. 2017. Softwood lignin self-assembly for nanomaterial design. *Biomacromolecules*, **18**(8), 2649-2653.

Sannigrahi, P., Pu, Y., Ragauskas, A. 2010. Cellulosic biorefineries—unleashing lignin opportunities. *Current Opinion in Environmental Sustainability*, **2**(5-6), 383-393.

Sapsford, K.E., Tyner, K.M., Dair, B.J., Deschamps, J.R., Medintz, I.L. 2011. Analyzing nanomaterial bioconjugates: a review of current and emerging purification and characterization techniques. *Analytical Chemistry*, **83**(12), 4453-4488.

Sarkar, S., Adhikari, B. 2000. Lignin-modified phenolic resin: synthesis optimization, adhesive strength, and thermal stability. *Journal of Adhesion Science and Technology*, **14**(9), 1179-1193.

Sawamura, K., Tobimatsu, Y., Kamitakahara, H., Takano, T. 2017. Lignin Functionalization through Chemical Demethylation: Preparation and Tannin-Like Properties of Demethylated Guaiacyl-Type Synthetic Lignins. *ACS Sustainable Chemistry & Engineering*, **5**(6), 5424-5431.

Scarica, C., Suriano, R., Levi, M., Turri, S., Griffini, G. 2018. Lignin

functionalized with succinic anhydride as building block for biobased thermosetting polyester coatings. *ACS Sustainable Chemistry & Engineering*, **6**(3), 3392-3401.

Schubert, S., Delaney Jr, J.T., Schubert, U.S. 2011. Nanoprecipitation and nanoformulation of polymers: from history to powerful possibilities beyond poly (lactic acid). *Soft Matter*, **7**(5), 1581-1588.

Schultz, T.P., Templeton, M.C. 1986. Proposed mechanism for the nitrobenzene oxidation of lignin. *Holzforschung*, **40**(2), 93-97.

Sette, M., Lange, H., Crestini, C. 2013. Quantitative HSQC analyses of lignin: a practical comparison. *Computational and Structural Biotechnology Journal*, **6**(7), e201303016.

Sevastyanova, O., Helander, M., Chowdhury, S., Lange, H., Wedin, H., Zhang, L., Ek, M., Kadla, J.F., Crestini, C., Lindström, M.E. 2014. Tailoring the molecular and thermo–mechanical properties of kraft lignin by ultrafiltration. *Journal of Applied Polymer Science*, **131**(18).

Shao, Y., Xia, Q., Dong, L., Liu, X., Han, X., Parker, S.F., Cheng, Y., Daemen, L.L., Ramirez-Cuesta, A.J., Yang, S. 2017. Selective production of arenes via direct lignin upgrading over a niobium-based catalyst. *Nature Communications*, **8**(1), 1-9.

Siepmann, J., Siegel, R.A., Rathbone, M.J. 2012. *Fundamentals and applications of controlled release drug delivery*. Springer.

Singh, A., Amiji, M.M. 2018. *Stimuli-responsive Drug Delivery Systems*. Royal Society of Chemistry.

Slowing, I., Trewyn, B.G., Lin, V.S.-Y. 2006. Effect of surface functionalization of MCM-41-type mesoporous silica nanoparticles on the endocytosis by human cancer cells. *Journal of the American Chemical Society*, **128**(46), 14792-14793.

Sluiter, A., Hames, B., Ruiz, R., Scarlata, C., Sluiter, J., Templeton, D. 2005a. Determination of ash in biomass. *Laboratory Analytical Procedure (LAP)*

Technical Report, **1617**.

Sluiter, A., Hames, B., Ruiz, R., Scarlata, C., Sluiter, J., Templeton, D., Crocker, D. 2008. Determination of structural carbohydrates and lignin in biomass. *Laboratory Analytical Procedure (LAP) Technical Report*, **1617**.

Sluiter, A., Ruiz, R., Scarlata, C., Sluiter, J., Templeton, D. 2005b. Determination of extractives in biomass. *Laboratory Analytical Procedure (LAP) Technical Report*, **1617**.

Tagami, A., Gioia, C., Lauberts, M., Budnyak, T., Moriana, R., Lindström, M.E., Sevastyanova, O. 2019. Solvent fractionation of softwood and hardwood kraft lignins for more efficient uses: Compositional, structural, thermal, antioxidant and adsorption properties. *Industrial Crops & Products*, **129**, 123-134.

Teixeira, M., Cerqueira, F., Barbosa, C.M., Nascimento, M.S., Pinto, M. 2005. Improvement of the inhibitory effect of xanthones on NO production by encapsulation in PLGA nanocapsules. *Journal of Drug Targeting*, **13**(2), 129-35.

Thorn, C.F., Oshiro, C., Marsh, S., Hernandez-Boussard, T., McLeod, H., Klein, T.E., Altman, R.B. 2011. Doxorubicin pathways: pharmacodynamics and adverse effects. *Pharmacogenetics and Genomics*, **21**(7), 440.

Tiwari, G., Tiwari, R., Sriwastawa, B., Bhati, L., Pandey, S., Pandey, P., Bannerjee, S.K. 2012. Drug delivery systems: An updated review. *International Journal of Pharmaceutical Investigation*, **2**(1), 2-11.

Toledano, A., García, A., Mondragon, I., Labidi, J. 2010. Lignin separation and fractionation by ultrafiltration. *Separation & Purification Technology*, **71**(1), 38-43.

Ugartondo, V., Mitjans, M., Vinardell, M.P. 2009. Applicability of lignins from different sources as antioxidants based on the protective effects on lipid peroxidation induced by oxygen radicals. *Industrial Crops & Products*, **30**(2), 184-187.

Wang, G., Chen, H. 2014. Carbohydrate elimination of alkaline-extracted lignin liquor by steam explosion and its methylolation for substitution of phenolic adhesive. *Industrial Crops and Products*, **53**, 93-101.

Wang, J., Tian, L., Luo, B., Ramakrishna, S., Kai, D., Loh, X.J., Yang, I.H., Deen, G.R., Mo, X. 2018. Engineering PCL/lignin nanofibers as an antioxidant scaffold for the growth of neuron and Schwann cell. *Colloids & Surfaces B: Biointerfaces*, **169**, 356-365.

Wang, Y., Li, P., Kong, L. 2013. Chitosan-modified PLGA nanoparticles with versatile surface for improved drug delivery. *Aaps Pharmscitech*, **14**(2), 585-592.

Wen, J.-L., Sun, S.-L., Xue, B.-L., Sun, R.-C. 2013. Recent advances in characterization of lignin polymer by solution-state nuclear magnetic resonance (NMR) methodology. *Materials*, **6**(1), 359-391.

Wen, J.-L., Xue, B.-L., Xu, F., Sun, R.-C. 2012. Unveiling the structural heterogeneity of bamboo lignin by in situ HSQC NMR technique. *BioEnergy Research*, **5**(4), 886-903.

Wertz, J.-L., Bédué, O. 2013. *Lignocellulosic biorefineries*. CRC press.

Wurm, F.R., Weiss, C.K. 2014. Nanoparticles from renewable polymers. *Frontiers in Chemistry*, **2**, 49.

Xiong, F., Han, Y., Wang, S., Li, G., Qin, T., Chen, Y., Chu, F. 2017. Preparation and formation mechanism of size-controlled lignin nanospheres by self-assembly. *Industrial Crops & Products*, **100**, 146-152.

Yang, Q., Wang, S., Fan, P., Wang, L., Di, Y., Lin, K., Xiao, F.-S. 2005. pH-responsive carrier system based on carboxylic acid modified mesoporous silica and polyelectrolyte for drug delivery. *Chemistry of Materials*, **17**(24), 5999-6003.

Yang, S., Zhang, Y., Yuan, T.Q., Sun, R.C. 2015. Lignin–phenol–formaldehyde resin adhesives prepared with biorefinery technical lignins. *Journal of Applied Polymer Science*, **132**(36).

Ye, S., Wang, C., Liu, X., Tong, Z. 2005. Multilayer nanocapsules of polysaccharide chitosan and alginate through layer-by-layer assembly directly on PS nanoparticles for release. *Journal of Biomaterials Science, Polymer Edition*, **16**(7), 909-923.

Yoshioka, R., Nakashima, Y., Fujiwara, Y., Komohara, Y., Takeya, M., Nakanishi, Y. 2016. The biological response of macrophages to PMMA particles with different morphology and size. *Biosurface and Biotribology*, **2**(3), 114-120.

Yu, Z., Ma, L., Ye, S., Li, G., Zhang, M. 2020. Construction of an environmentally friendly octenylsuccinic anhydride modified pH-sensitive chitosan nanoparticle drug delivery system to alleviate inflammation and oxidative stress. *Carbohydrate Polymers*, **236**, 115972.

Yurgel, V.C., Oliveira, C.P., Begnini, K.R., Schultze, E., Thurow, H.S., Leon, P.M., Dellagostin, O.A., Campos, V.F., Beck, R.C., Guterres, S.S., Collares, T., Pohlmann, A.R., Seixas, F.K. 2014. Methotrexate diethyl ester-loaded lipid-core nanocapsules in aqueous solution increased antineoplastic effects in resistant breast cancer cell line. *International Journal of Nanomedicine*, **9**, 1583-91.

Zakzeski, J., Jongerius, A.L., Bruijnincx, P.C., Weckhuysen, B.M. 2012. Catalytic lignin valorization process for the production of aromatic chemicals and hydrogen. *ChemSusChem*, **5**(8), 1602-1609.

Zhang, M., Ogale, A.A. 2014. Carbon fibers from dry-spinning of acetylated softwood kraft lignin. *Carbon*, **69**, 626-629.

Zhang, X.-y., Zhang, P.-y. 2017. Polymersomes in nanomedicine-A review. *Current Nanoscience*, **13**(2), 124-129.

Zhang, X., Jeremic, D., Kim, Y., Street, J., Shmulsky, R. 2018. Effects of surface functionalization of lignin on synthesis and properties of rigid bio-based polyurethanes foams. *Polymers*, **10**(7), 706.

Zhao, C., Huang, J., Yang, L., Yue, F., Lu, F. 2019. Revealing Structural Differences between Alkaline and Kraft Lignins by HSQC NMR.

Industrial & Engineering Chemistry Research, **58**(14), 5707-5714.

Zhou, Y., Han, Y., Li, G., Yang, S., Xiong, F., Chu, F. 2019. Preparation of Targeted Lignin–Based Hollow Nanoparticles for the Delivery of Doxorubicin. *Nanomaterials*, **9**(2), 188.

Zhu, S., Wu, Y., Chen, Q., Yu, Z., Wang, C., Jin, S., Ding, Y., Wu, G. 2006. Dissolution of cellulose with ionic liquids and its application: a mini-review. *Green Chemistry*, **8**(4), 325-327.

Zylberberg, C., Matosevic, S. 2016. Pharmaceutical liposomal drug delivery: a review of new delivery systems and a look at the regulatory landscape. *Drug Delivery*, **23**(9), 3319-3329.

초 록

산업공정 리그닌을 이용한 약물 방출 조절형 나노입자 합성

서울대학교 대학원
산림과학부
환경재료과학전공
이재훈

최근 리그닌을 약물 전달 시스템의 재료로 이용하는 연구가 주목받고 있다. 특히 리그닌으로 나노입자를 제조하는 연구는 약물 수송 및 방출 조절에 관한 장점을 부여할 수 있어 선호되는 추세이다. 하지만 그중 리그닌의 구조적 특성이 나노입자의 형성 과정이나 물성(크기, 콜로이드 안정성, 생체안전성)에 미치는 영향에 주목한 연구는 거의 없는 실정이다. 본 연구에서는 산업공정 부산물로 발생하는 리그닌 부산물의 구조적 특성이 리그닌 나노입자의 물성에 미치는 영향을 이해하고자 하였다. 해당 결과를 바탕으로 약물 저장 리그닌 나노입자를 합성하여 약물 방출 특성과 기대 효과를 생체외 및 생체내 조건에서의 생체안전성 실험을 통하여 구명하였다.

우선 산업공정 부산물인 kraft 리그닌을 순차적 용매 분획화하여 분자량, 수산기 함량, 분자간 주요 결합 함량이 각기 다른 5개 분획으로 분리하였다. 각 리그닌 분획으로부터 THF-리그닌 용액과 증류수의 치환에 의한 나노침전법을 통하여 나노입자를 획득하였으며 입자 크기는 최소 193 nm에서 최대 1,039 nm로 다양하게 나타났다. 리그

닌 분자량이 작을수록, 페놀성 수산기 함량이 높을수록 크면서 균질한 분포를 보이는 입자가 형성되었으며 kraft 리그닌의 구조적 특성과 형성된 나노입자의 입자 크기와 분포는 리그닌 분자량과 수산기 함량, 특히 페놀성 수산기 함량에 영향을 받는 것으로 판단되었다. 나노입자는 대체로 깔끔한 구형으로 형성되었으며 증류수에 안정적인 콜로이드 상태로 분포하였다(−44.5 ~ −29.1 mV). 세포 생존율 및 혈구독성 평가 결과 리그닌 나노입자는 높은 농도 조건에서도 최소 3일간 높은 수준의 지속적인 세포안전성을 보이는 것을 확인하였다.

위 결과를 바탕으로 선택한 특정 리그닌 조건으로부터 약물 저장 나노입자를 합성하였으며 약물 방출 조절 효과를 입증하기 위한 실험을 수행하였다. 약물 저장 리그닌 나노입자는 coumarin 6에 대하여 최대 59%, 독소루비신에 대하여 최대 73%의 약물 저장 효율을 나타내었다. 약물 저장 리그닌 나노입자의 크기(176 ~ 469 nm)는 대조군과 비교하였을 때 약물 첨가에 큰 영향을 받지 않는 것으로 나타났다. 또한, 약물 저장 여부는 나노입자의 콜로이드 안정성에도 영향을 미치지 않았다. 약물 저장 리그닌 나노입자는 대체로 0 ~ 4시간 사이에 빠른 약물 방출 경향을 보였고 혈액과 동일한 pH 조건보다는 산성 조건에서의 약물 방출이 더 빠른 것으로 나타났다. 리그닌 나노입자는 생체외 혈구독성 실험과 생체내 알레르기 반응 실험에서 우수한 생체안전성을 나타냈으며, 생체외 세포독성 실험과 생체내 항암효과 검증 실험에서 약물 방출 조절 및 부작용 경감에 의한 사망률 감소 효과를 나타냈다.

Alkaline/soda 리그닌의 경우 순차적 용매 분획화와 별도로 페놀성 수산기의 메틸화 반응을 수행하여 분자량의 변화가 상대적으로 적으면서 페놀성 수산기의 함량이 각기 다른 4개 그룹을 추가로 획득하였다. 구조적 변형을 거친 해당 리그닌 그룹으로부터 나노입자를 획득

하여 그 물성을 분석한 결과, 분획화 리그닌 유래 나노입자는 kraft 리그닌에서와 유사한 크기 분포 경향을 보였다. 반면, 메틸화 리그닌 유래 나노입자는 페놀성 수산기가 감소함에 따라 크기가 감소하는(721 ~ 516 nm) 뚜렷한 경향을 보였다. 모든 조건에서 나노입자의 콜로이드 안정성은 높게 유지되었으며 생체안전성 역시 대부분 농도 및 시간 조건에서 안전성을 나타냈다.

본 연구에서는 펄프 및 바이오에탄올 생산공정에서 부산물로 발생하는 리그닌의 고부가가치 활용방안으로 약물 방출 조절 나노입자 합성을 제시하였다. 리그닌의 구조적 특성과 나노입자 물성의 상관성을 구명하여 본 연구에서 다루지 않은 다른 리그닌을 이용한 나노입자 제조 및 물성 제어에 있어서도 단초를 제공하였으며, 생체외 및 동물 실험을 통한 리그닌 나노입자의 약물 방출 조절 및 부작용 경감 효과를 검증하여 약물 전달체 원료로써 실제 적용 가능성을 제시하였다.

키워드 : 산업공정 리그닌, 약물 저장 나노입자, 나노침전법, 리그닌
　　　　　기능화, 약물 전달 시스템, 생체안전성

학　번 : 2016-30382